

Leipzig University
Faculty of Physics and Earth System Sciences
Semiconductor Physics Group

Structural and Electrical Properties of Heteroepitaxial grown Cr₂O₃



UNIVERSITÄT
LEIPZIG

Master's Thesis

Submitted by

Jakob Seifert

Leipzig, November 2024

Revision: Prof. Dr. Marius Grundmann
Dr. habil. Holger von Wenckstern

Supervision: Dr. habil. Holger von Wenckstern
Dr. Sofie Vogt
Dr. Clemens Petersen

Contents

1	Introduction	5
2	Theory	7
2.1	Sesquioxides	7
2.1.1	Chromium Oxide	8
2.1.2	Gallium Oxide	11
2.2	X-ray Diffraction Principles	12
2.2.1	Scattering at Lattices	12
2.2.2	X-rays	14
2.3	Heteroepitaxy	15
2.3.1	Pseudomorphic Growth	15
2.3.2	Relaxed Growth	17
3	Experimental Methods	21
3.1	Pulsed Laser Deposition	21
3.1.1	Setup	21
3.1.2	Plasma Dynamics	22
3.1.3	Segmented Target Approach	23
3.2	X-Ray Diffraction Measurement	24
3.2.1	2θ - ω -scans	25
3.2.2	ω -scans	26
3.2.3	ϕ -scans	26
3.2.4	Reciprocal Space Maps	26
3.2.5	Technical Details	29
3.3	Thermal Evaporation	30
3.4	Resistivity Measurement	30
3.5	Thickness Determination	32
3.6	Spectral Transmission	33
3.7	Further Measurement Methods	34
4	Experiment, Results and Discussion	35
4.1	Growth Window for Cr_2O_3 Deposition on Sapphire	35
4.1.1	Experiment	35

4.1.2	Oxygen Partial Pressure Variation on <i>m</i> -plane Sapphire	36
4.1.3	Growth Temperature Variation on <i>m</i> -plane Sapphire	39
4.1.4	Influence of Growth Rate on Crystal Structure	39
4.1.5	Deposition on <i>c</i> -, <i>r</i> -, <i>m</i> - and <i>a</i> -plane Sapphire	42
4.1.6	Conclusion	44
4.2	Discrete Combinatorial Synthesis for Tailored Doping	46
4.2.1	Experiment	46
4.2.2	DCS with Different Targets	47
4.2.3	Conclusion	53
4.3	Strain Analysis	56
4.3.1	Experiment	57
4.3.2	Growth Rates	61
4.3.3	Strain and Tilt for Different Orientations	63
4.3.4	Conclusion	77
4.4	Cr ₂ O ₃ Buffer Layers for α -Ga ₂ O ₃	80
4.4.1	Experiment	80
4.4.2	Comparison of <i>in situ</i> and <i>ex situ</i> grown Ga ₂ O ₃ on Cr ₂ O ₃ . . .	81
4.4.3	Conclusion	86
Appendices		91
A Calculations		93
A.1	<i>m</i> -plane lattice constants	93
A.2	<i>a</i> -plane lattice constants	94
B Figures		95
Bibliography		101

Chapter 1

Introduction

Semiconductor technology today is based on the versatility of silicon: its band gap of 1.1 eV is large enough to allow tailoring its conductivity from semi-insulating to conductive – on the other hand, it is small enough to be doped both *p*-type or *n*-type. Even though being present in a vast range of applications, today's technological requirements push silicon to its limits: power switching applications and high-frequency electronics are strongly dependent on the electrical field at which breakdown occurs [1]. This critical field strength however is correlated to the band gap of the underlying material [2], which is why Ultrawide-bandgap (UWBG) materials have gained much attention: Those semiconductors can provide the necessary properties which are needed, for example, in the optimization of charging and motor drive efficiency in electric vehicles [3] – which itself is an important step towards lowering emissions.

One interesting UWBG semiconductor is Ga_2O_3 , which turned out to be a viable material for solar-blind UV detectors [4], power rectifiers [5], power MOSFETs [6] and gas sensors [7]. Its thermodynamically most stable β -phase ($E_g = 4.6 - 5.0 \text{ eV}$) has been extensively studied, but the α -phase has an even higher band gap of up to 5.3 eV [8]. This metastable Ga_2O_3 phase crystallizes in the corundum structure, making it isostructural to cost-efficient and readily available sapphire (Al_2O_3) substrates. However, there is still a lattice mismatch of 4.6 % between $\alpha\text{-}\text{Ga}_2\text{O}_3$ and Al_2O_3 , regarding the *a*-constant. This introduces a large amount of threading dislocations [9], which strongly reduces the mobility in $\alpha\text{-}\text{Ga}_2\text{O}_3$ thin films [10]. Additionally, due to similar growth conditions of the α -phase, phase pure deposition of $\alpha\text{-}\text{Ga}_2\text{O}_3$ is a challenge for different growth techniques [11]. Several attempts have been undertaken to overcome these technical aspects of deposition, namely epitaxial lateral overgrowth [12] and growth on patterned substrates [13] or buffer layers [14, 15].

A promising buffer layer material for $\alpha\text{-}\text{Ga}_2\text{O}_3$ is chromium oxide (Cr_2O_3), which is isomorphic to $\alpha\text{-}\text{Ga}_2\text{O}_3$ with a very low lattice mismatch of only 0.4 % regarding the *a*-constant – one order of magnitude lower compared to Al_2O_3 . The feasibility of this approach has been demonstrated with Halide Vapor Phase Epitaxy (HVPE) [16–19], a Chemical Vapor Deposition (CVD) method also widely applied for successfully

depositing phase pure α -Ga₂O₃ thin films on several sapphire orientations [20]. Cr₂O₃ is also interesting due to its defect-induced *p*-type nature, which can be enhanced by doping with lower valent cations [21–24]. Because it is virtually impossible to achieve *p*-type Ga₂O₃ [25], Cr₂O₃ is a candidate for both *p*-type alloys with α -Ga₂O₃, similar to (Ir, Ga)₂O₃ [26], and *p-n* heterostructures with very low lattice mismatch at the interface [18].

Because Pulsed Laser Deposition (PLD) is a promising Physical Vapor Deposition (PVD) method for fabricating α -Ga₂O₃ thin films and devices [27–29], the aim of this work is to show the feasibility of preparing Cr₂O₃ thin films via PLD. Therefore, the growth window of thin film growth depending on oxygen partial pressure, growth temperature and substrate orientation is investigated (chapter 4.1). Detailed structural analysis via Reciprocal Space Maps (RSMs) is done for thin films fabricated with various laser energy densities during deposition (chapter 4.3). Furthermore, a segmented target approach is utilized to aim for tailored conductivities of Zn- and Cu-doped Cr₂O₃ thin films (chapter 4.2). Finally, it is shown that α -Ga₂O₃ can be deposited phase pure on Cr₂O₃ buffer layers in *c*-, *r*-, *m*- and *a*-orientation (chapter 4.4). Before analyzing the results of those experiments, a short overview will be given on the here investigated sesquioxides, as well as the basics of X-ray diffraction (XRD) and heteroepitaxy of rhombohedral materials.

Chapter 2

Theory

2.1 Sesquioxides

Transparent Conductive Oxides (TCOs) are materials that combine the properties of having low absorption coefficient in the visible spectrum and being conductive at the same time [30]. The interest in these materials is motivated by possible applications in portable and flexible electronics [31], displays [32], solar cells [33] and more [30]. Not only the focus on a small number of materials in the past (SnO_2 , In_2O_3 , ZnO) [30], but also the scarcity and concerns about availability⁽¹⁾ of fundamental compounds [34] increases the demand for new materials. This includes fabrication of *p*-type TCOs as well as compounds with even larger band gaps than 3 eV, called Ultrawide-bandgap (UWBG) materials. Because the critical electrical field – at which breakdown occurs – is depending on the band gap [2], UWBG materials can serve for high-power electronic devices as well as for deep ultra-violet (UV) optoelectronics [35]. Candidates for this material class are group-III sesquioxides⁽²⁾, of which Ga_2O_3 with its several polymorphs [8] recently gained interest in the scientific community – in particular the metastable corundum structured $\alpha\text{-}\text{Ga}_2\text{O}_3$.

The sesquioxide Cr_2O_3 , being a possible *p*-type TCO, is isomorphic to group-III sesquioxide $\alpha\text{-}\text{Ga}_2\text{O}_3$ with quite similar lattice parameters (cf. Tab. 2.1). This enables the use of Cr_2O_3 as a buffer layer between $\alpha\text{-}\text{Ga}_2\text{O}_3$ and isomorphic $\alpha\text{-}\text{Al}_2\text{O}_3$ (sapphire) substrates to improve the crystal quality [16]. The lower band gap also makes band gap engineering with isostructural sesquioxides interesting [36] and finally, Cr_2O_3 exhibits increased conductivity upon doping [37] and could thus serve as *p*-type component in a *p-n*-heterojunction with $\alpha\text{-}\text{Ga}_2\text{O}_3$. In the following, an overview of the two mentioned sesquioxides will be presented with focus on the physical properties being relevant to this work.

⁽¹⁾ China controls 75 % of the world's indium reserves, and limited the export of this material already in the past [34].

⁽²⁾ A sesquioxide is an oxide with formula unit Me_2O_3 , where Me is a metal with oxidation state +3. Transition metal sesquioxides are, e.g., Y_2O_3 , Rh_2O_3 or In_2O_3 .

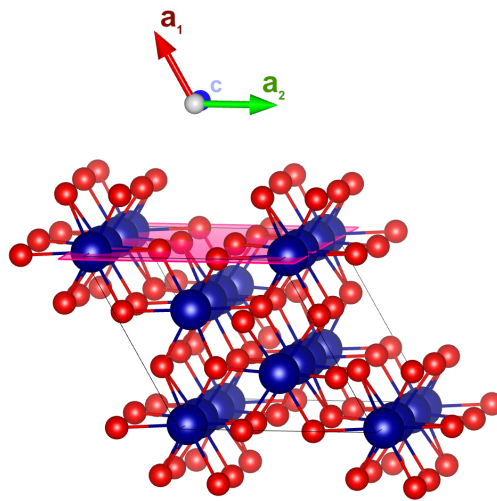


Figure 2.1: Image of the rhombohedral Cr_2O_3 crystal structure. Blue and red spheres correspond to Cr and O atoms, respectively. The magenta plane is the (10.0) m -plane. The image was made using VESTA Ver. 3 [47].

2.1.1 Chromium Oxide

Chromia or *Eskolaite* is a sesquioxide composed of the transition metal chromium and oxygen with formula unit Cr_2O_3 . Other chromium oxides do exist (e.g. metallic CrO_2 , toxic CrO_3), but Cr_2O_3 is the thermodynamically most stable oxidation state [38–40], making it the abundant chromium oxide on earth [41].

Chromium oxide is used for a wide range of applications, in particular it can be utilized as a coating material due to its high hardness [42], sufficient transparency for low thicknesses [43] as well as its resistance against corrosion and oxidation [44]. This also explains its use-case as component of stainless steel to form passive films [40]. Cr_2O_3 thin films absorb electromagnetic waves with wavelengths smaller than 400 nm, making it opaque in the UV-spectrum [45, 46]. It is transparent in the visible spectrum with, e.g., a reported transmittance of 40 % at 700 nm for 0.5 μm thick films by Cheng *et al.* [45].

Cr_2O_3 crystallizes in the corundum structure, which has trigonal symmetry (space group $R\bar{3}c$) and belongs to the hexagonal crystal family. One unit cell contains six formula units, i.e. 12 chromium cations and 18 oxygen anions [40]. The oxygen atoms arrange in a hexagonal close-packed manner, where two thirds of the formed octahedrons are filled with Cr atoms [48]. The unit cell is spanned by a principal axis, called c -axis⁽³⁾, with lattice constant c , and a hexagonal basal plane with lattice constant a . The numerical values for those lattice parameters differ depending on the publication [16, 22, 41, 49, 50], and henceforth the values in Tab. 2.1 will be used [41, 51, 52]. Only one study is known to the author that states another cubic spinel γ -phase with

⁽³⁾ The spins of the Cr atoms along this direction are alternating $3 \uparrow$ and $3 \downarrow$ [49], making the crystal antiferromagnetic [40, 48].

Table 2.1: Lattice constants of selected corundum structured sesquioxides.

	<i>a</i>	<i>c</i>	Ref.
$\alpha\text{-Al}_2\text{O}_3$	4.76 Å	13.00 Å	Pishchik <i>et al.</i> [51]
$\alpha\text{-Cr}_2\text{O}_3$	4.96 Å	13.59 Å	Mi <i>et al.</i> [41]
$\alpha\text{-Ga}_2\text{O}_3$	4.98 Å	13.43 Å	Marezio and Remeika [52]

Table 2.2: Several deposition techniques that have been applied on Cr_2O_3 .

Deposition technique	Substrate	Reference
Chemical Vapor Deposition (CVD)	Si(111)	[54, 55]
	glass	[45]
Molecular Beam Epitaxy (MBE)	<i>c</i> -sapphire	[24, 49]
Thermal evaporation	Pt(111)	[38]
Electron-beam Physical Vapor Deposition (PVD)	glass	[39]
Spray pyrolysis	glass	[21]
radio-frequency (RF) sputtering	<i>c</i> -sapphire	[16, 18]
	<i>r</i> -sapphire	[17]
Reactive direct current (DC) sputtering	glass	[46]
Reactive Pulsed Laser Deposition (PLD)	Si(100)	[56]
	<i>r</i> -sapphire	[57]
Non-reactive PLD	<i>c</i> -sapphire	[23, 49, 58]

random missing Cr point defects [38]. This information is based on Wyckoff [53], but the source is not available, so no further information can be given about the stability or other properties of this potential phase. Henceforth, Cr_2O_3 will refer to the α -phase.

Several techniques combined with various substrates were applied for depositing chromia thin films, which are listed in Tab. 2.2. The first deposition via PLD was done by Tabbal *et al.* [59].

Electronic Structure Experimental and theoretical studies reveal that chromia exhibits a band gap of 3.2 to 3.4 eV [22, 38, 40, 41] making it a wide band gap material. Discussion on the *p*-type or insulating behavior of Cr_2O_3 can be found in literature: With only a few defects, high quality epitaxial films of Cr_2O_3 grown by MBE [24] or PLD [49] are not *p*-type. This insulating behavior is classified as both Mott-Hubbard type and charge-transfer type, which are models to describe the electronic behavior of compounds containing transition metals with partly filled $3d^n$ orbitals, with $n = 5$ for Cr [40, 41, 48]. Density Functional Theory (DFT) calculations show that the Cr-3*d* states are almost solely responsible for electronic states in the conduction band and that they are also present in the valence band [40, 41]. Thus, $3d \rightarrow 3d$ band transitions are possible, indicating that the Mott-Hubbard model might fit best for this compound [40]. However, the O-2*p* states are mainly present in the valence band at similar energies as the Cr-3*d* states, which leads to hybridization and thus indicating the charge-transfer model [40].

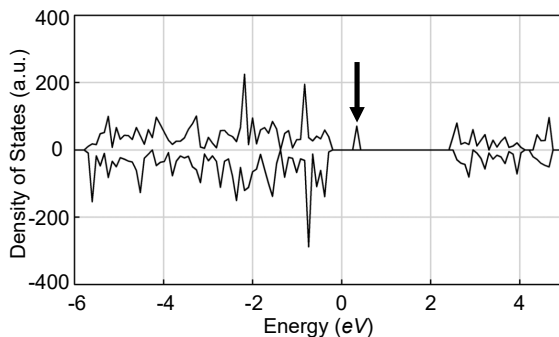


Figure 2.2: Calculated density of states (DOS) of chromia, taking a V_{Cr} into account. The arrow marks the new acceptor level. Reprinted with permission from Lebreau *et al.* [40]. Copyright © 2014 American Chemical Society.

However, several studies agree on Cr_2O_3 being a semiconductor with *p*-type conductivity at room temperature and atmospheric conditions [18, 40, 41, 45, 56, 58, 60]. Calculations were performed to investigate the effect of point defects on the band structure and conductivity. When considering a missing chromium atom (*vacancy* V_{Cr}), the band structure changes in two ways: The band gap itself is reduced [41], but not sufficiently to make excitations of valence electrons into the conduction band more probable than for defectless chromia. Additionally, there is a new defect band introduced slightly above the Fermi level (cf. Fig. 2.2), which acts as an unoccupied acceptor level [41]. This defect state is mainly composed of O-2p orbitals of the oxygen anions surrounding the vacancy [40]. Effectively, a missing neutral chromium atom removes the Cr^{3+} cation as well as three electrons bound to the adjacent O^{2-} anions, thus creating three holes [40] explaining the *p*-type conductivity.

Note that there are also other possible defects with different effects: a chromium FRENKEL point defect describes a Cr atom leaving its position and occupying a formerly unoccupied cavity in one of the oxygen-octahedrons. This FRENKEL defect creates a new band below the Fermi level, acting as an occupied donor level [40]. A similar defect state is introduced by oxygen vacancies [41]. Note that the Fermi level is located only slightly above the Valence Band Maximum (VBM) and thus the new occupied donor level is not significantly closer to the Conduction Band Minimum (CBM), which means that electrons still have to overcome the band gap energy to get into conducting states. This favors the formation of holes via Cr vacancies (O-2p acceptor states) rather than electrons via Cr Frenkel defects and O vacancies (Cr-3d donor states).

Doping Several attempts have been made to alter the conductivity of chromia thin films deliberately, including incorporation of magnesium [21, 24, 37], nickel [23], or lithium [61, 62] to achieve better *p*-type conductivity. On the other hand, incorporation of titanium yields electrons as majority carriers [63] due to the higher valent state of Ti when substituting Cr sites (Ti_{Cr}) [60].

Especially the effect of Mg doping of Cr_2O_3 thin films has been reported in liter-

ature. [21–24, 37, 49, 63]. Substituting Cr atoms with less valent hole providers – compared to structural defects of pure Cr_2O_3 – does not only allow for a more controlled defect incorporation, but is also energetically more favorable due to a lower formation energy of Mg_{Cr} compared to V_{Cr} [49]. Uekawa and Kaneko [37] report an increase in conductivity of five orders of magnitude for $\text{Cr}_2\text{O}_3:\text{Mg}$ thin films prepared by the polymer precursor method. This result can be further improved by postannealing [24] and deposition at higher oxygen partial pressures [24, 63]. These effects are attributed to homogenization of magnesium inside the thin films and increased MgO incorporation during deposition, respectively. An observed side-effect of Mg-doping is a color change to a brownish tint [22, 37]. Uekawa and Kaneko [37] discuss that this may be the result of a mixed valence state of chromium (Cr^{4+} or Cr^{6+}), formed upon doping, as observed by X-ray Photoelectron Spectroscopy (XPS). This may establish an unoccupied state, favoring charge-transfer transitions from $\text{O}-2p$ orbitals to this low-energetic state, resulting in a different optical appearance of the thin films. However, it has been shown that the overall transparency can be increased by codoping of Mg with nitrogen which also reduces the decolorization substantially [21, 22].

2.1.2 Gallium Oxide

Ga_2O_3 is a group-III sesquioxide with four⁽⁴⁾ different polymorphs, of which β - Ga_2O_3 is the thermodynamically most stable one at ambient conditions [8, 27, 64]. The corundum-structured α - Ga_2O_3 phase, which is of most relevance for this work, is isomorphic to Cr_2O_3 , with lattice parameters as listed in Tab. 2.1. Note that Cr_2O_3 has a larger c lattice constant, but a smaller a lattice constant than α - Ga_2O_3 . However, both compounds have larger lattice constants than Al_2O_3 . α - Ga_2O_3 is thermodynamically metastable [65], i.e. the phase can exist under ambient conditions, even though β - Ga_2O_3 has a lower energy state up to 1800 °C [25]. The thermodynamic equilibrium – which determines the favored phase – can also be changed by strain due to lattice mismatch occurring during heteroepitaxy. [27]. This approach is of particular interest due to the possibility of deposition on cheap – compared to bulk β - Ga_2O_3 substrates [65, 66] – and readily available sapphire substrates which are isomorphic to α - Ga_2O_3 [17, 25, 65]. Note that deposition of β - Ga_2O_3 on sapphire is also possible, but only with restriction to formation of more than one crystal domain [66]. On the other hand, highly crystalline [25] α - Ga_2O_3 thin films can be grown without rotational domains [27, 66].

Deposition of α - Ga_2O_3 on sapphire has been done by several deposition techniques, including [66]: Halide Vapor Phase Epitaxy (HVPE), mist CVD [9], MBE [64], Atomic Layer Deposition and metalorganic CVD. Phase-pure deposition via PLD has also been achieved [27, 28, 64]. Despite being isomorphic to each other, α - Ga_2O_3 and sapphire still exhibit a lattice mismatch of around 4.8 % along the a -axis [65]. This induces

⁽⁴⁾ Five, if the δ -phase is not considered as a form of the α -phase [8].

semicoherent growth with a fairly high dislocation density, which has been reported to be around $7 \times 10^{10} \text{ cm}^{-2}$ [9]. In particular, this becomes a problem regarding carrier mobility which is tremendously hindered by dislocation scattering [65].

To overcome the problems of lattice mismatch between sapphire substrates and α - Ga_2O_3 thin films, quasi-continuous gradients from Al_2O_3 to α - Ga_2O_3 have been applied, utilizing the capability of alloying the respective compounds [14]. Furthermore, buffer layers of isomorphic Cr_2O_3 have been used to decrease the high dislocation density for deposition on *c*-oriented [16, 18] as well as *r*-oriented sapphire [17]. Deposition on other than *c*-oriented substrates also decreases parasitic phases because of the suppression of *c*-plane facets on *m*- and *a*-plane sapphire [67]. Deposition on prismatic *m*-plane sapphire also yields much higher carrier mobilities when compared to *c*-plane sapphire [68]. It has to be noted that despite the difficulties occurring upon lattice mismatch, pseudomorphic growth seems to be feasible without buffer layers for different deposition techniques, at least for some monolayers [64].

With 5.0 to 5.3 eV [66], α - Ga_2O_3 has the highest band gap of the four polymorphs [25]. Band gap engineering is possible by alloying with Al_2O_3 [67] or In_2O_3 [69]. The crystal structure also allows for alloying with other corundum structured compounds [66], in particular other transition metal oxides such as Cr_2O_3 [17, 18]. The conduction band is mainly composed of Ga-4s states with an effective electron mass of $0.3 m_e$. The valence band is very flat and mainly composed of O-2p orbitals, yielding a high effective electron mass and thus strong localization [25]. This hinders the realization of *p*-type α - Ga_2O_3 . Next to band gap engineering, *n*-type doping via Sn, Si and Ge [28], as well as Zr [29] incorporation has been accomplished.

2.2 X-ray Diffraction Principles

2.2.1 Scattering at Lattices

To elucidate the working principles behind X-ray diffraction (XRD) as a measurement method (cf. 3.2), a brief description of reciprocal space and constructive interference will be provided. Those derivations are based on Ashcroft and Mermin [70].

A periodic point-like structure with translational symmetry (“BRAVAIS lattice”) can be described by three vectors \mathbf{a}_i that span a so-called “unit cell”. Every lattice point \mathbf{R} is a linear combination of those unit cell vectors. For such a lattice, there exists a so-called “reciprocal lattice”, which consists of all vectors \mathbf{K} satisfying the condition⁽⁵⁾:

$$e^{i\langle \mathbf{K}, \mathbf{R} \rangle} = 1, \quad (2.1)$$

$$\Leftrightarrow \langle \mathbf{K}, \mathbf{R} \rangle = 2\pi m, \quad (2.2)$$

⁽⁵⁾ The definition of \mathbf{K} by (2.1) is a consequence of demanding that the plane wave described by $f_{\mathbf{K}}(\mathbf{r}) = \exp(i\langle \mathbf{K}, \mathbf{r} \rangle)$ has the same symmetry as the BRAVAIS lattice [70].

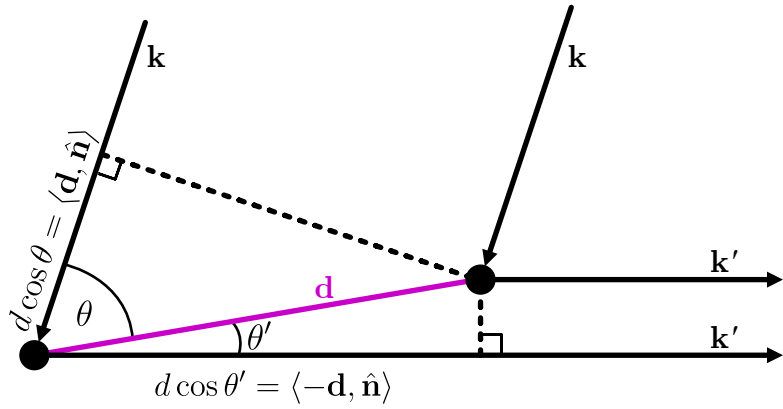


Figure 2.3: The geometry of two scattering centers displaced by \mathbf{d} , as well as incident and reflected X-rays \mathbf{k} and \mathbf{k}' , respectively.

with $m \in \mathbb{N}$. This is again a BRAVAIS lattice with unit cell vectors \mathbf{a}_j^* :

$$\mathbf{K}_{hkl} = h\mathbf{a}_1^* + k\mathbf{a}_2^* + l\mathbf{a}_3^*. \quad (2.3)$$

It follows that for any i, j :

$$\langle \mathbf{a}_i^*, \mathbf{a}_j \rangle = 2\pi\delta_{ij}, \quad (2.4)$$

with the KRONECKER delta δ_{ij} . A major application of reciprocal space vectors is their ability to describe lattice planes. Any lattice plane can be described by the shortest possible reciprocal space vector \mathbf{K}_{hkl} perpendicular to it. Consequently, the lattice plane is denoted by (hkl) . The distance between equivalent lattice planes can be calculated via

$$d_{hkl} = |\mathbf{K}_{hkl}|^{-1}. \quad (2.5)$$

Note that for non-cubic crystals, the lattice plane (hkl) is in general *not* perpendicular to the lattice direction $[hkl]$.

With those preliminaries, the conditions for constructive interference during diffraction of radiation at BRAVAIS lattices can be derived. Consider two scattering centers separated by \mathbf{d} (Fig. 2.3) and incident radiation with wave vector \mathbf{k} :

$$\mathbf{k} = \frac{2\pi}{\lambda}\hat{\mathbf{n}}, \quad (2.6)$$

with wavelength λ and direction $\hat{\mathbf{n}}$. For the case of elastic scattering, the outgoing wave vector \mathbf{k}' has the same wavelength λ but different direction $\hat{\mathbf{n}}'$. The phase difference of two photons scattered at the 1st and 2nd scattering center, respectively, can be calculated from their path difference, which reads

$$\langle \mathbf{d}, \hat{\mathbf{n}} \rangle + \langle -\mathbf{d}, \hat{\mathbf{n}}' \rangle. \quad (2.7)$$

Constructive interference occurs, if the phase difference is an integral multiple of the

wavelength, so it must follow that

$$\langle \mathbf{d}, (\hat{\mathbf{n}} - \hat{\mathbf{n}}') \rangle = m\lambda \quad (2.8)$$

$$\Leftrightarrow \langle \mathbf{d}, (\hat{\mathbf{k}} - \hat{\mathbf{k}}') \rangle = 2\pi m, \quad (2.9)$$

with $m \in \mathbb{N}$. Comparing with Equ. (2.2) reveals that $\hat{\mathbf{k}} - \hat{\mathbf{k}}'$ is a reciprocal space vector, because the separation \mathbf{d} of the two scattering centers is a lattice vector \mathbf{R} . So constructive interference (observing a reflection) occurs if and only if the scattering geometry (determined by angle of incidence and refraction, as well as wavelength) matches the lattice symmetry in the sense that there is a corresponding lattice translation vector \mathbf{d} fulfilling Equ. (2.9). Thus, from the position of reflections in reciprocal space, one can deduce the lattice symmetry.

Note that this description of X-ray scattering is equivalent to the BRAGG condition:

$$m\lambda = 2d_{hkl} \sin(\theta), \quad (2.10)$$

where the angle of incidence θ and λ are contained in $\hat{\mathbf{k}} - \hat{\mathbf{k}}'$. Furthermore, when a lattice point is not equivalent to a single atom, but represents several scattering centers, an additional geometrical structure factor has to be taken into account to determine whether a certain geometry allows reflexes. This is important, e.g., for structures with trigonal symmetry. They are described with a conventional hexagonal unit cell, although not every plane (hkl) exhibits constructive interference. The condition for allowed reflections is $-h + k + l = 3n$, with $n \in \mathbb{N}_0$ [71].

2.2.2 X-rays

Atomic distances in solids are of the order of several Å, so the radiation for probing those structures must have a similarly sized wavelength, which is fulfilled by X-rays [72]. The following description of X-rays is based on Spieß [73].

The basis of any X-ray tube are high-energy electrons which are produced by thermionic emission in a cathode, which is usually made out of tungsten⁽⁶⁾. An electric field of several KV accelerates the electrons to the anode, where they are stopped such that around 99 % of their kinetic energy dissipates. The momentum change of electrons, which are charged particles, leads to emission of bremsstrahlung. Furthermore, the electrons ionize atoms of the anode material which leads to unoccupied electron states. If those states are filled by electrons with higher quantum number n , the difference in energy of those levels is emitted as radiation with a discrete spectrum, called characteristic X-ray. Important for XRD measurements is a part of the characteristic spectrum, called K-radiation, which originates in occupation of empty 1s-orbitals.

⁽⁶⁾ Tungsten is the element with the second highest melting point of around 3400 °C. This ensures a low contamination of the anode with cathode material, reducing the intensity of observed peaks in XRD patterns that correspond to tungsten (cf. 3.2).

The occupying electron must come from an orbital with angular momentum quantum number $l = 1$, i.e. a p -orbital, because Δl cannot be zero for intraatomic electron transitions. The radiation is termed K α - or K β -radiation, depending on whether the previous orbital was $2p$ or $3p$, respectively. Furthermore, one distinguishes K α_1 - and K α_2 -radiation, depending on the magnetic quantum number of the previous orbital, which can be $\frac{3}{2}$ or $\frac{1}{2}$, respectively. K α -radiation is desired for probing crystal structures.

2.3 Heteroepitaxy

2.3.1 Pseudomorphic Growth

When a body is deformed (*strained*) from its original state of equilibrium (*bulk*), forces will arise that tend to return the body to this equilibrium. Molecular forces are the driving element behind these stresses [74]. In continuum mechanics, stress σ_{ij} and strain ϵ_{kl} are symmetric rank-2 tensors that are linearly connected by the elasticity tensor with components C_{ijkl} :

$$\sigma_{ij} = \sum_{k,l} C_{ijkl} \epsilon_{kl}. \quad (2.11)$$

Note that Equ. (2.11) represents a set of 9 linear equations.

If the in-plane (i.p.) lattice constants of two isomorphic compounds match at the interface of a heterostructure, one refers to “pseudomorphic” growth. This confines a part of the system of equations (2.11):

1. The thin film i.p. lattice constants a_{\parallel}^F have to match the substrate i.p. lattice constants a_{\parallel}^S . This defines the magnitude of i.p. strain of the thin film material.
2. On the other hand, due to vertical growth, the out-of-plane (o.o.p.) stress of the thin film is demanded to be zero: $\sigma_{zz} = 0$.

The resulting o.o.p. strain as well as non-diagonal strain components can be derived by solving the system of equations (2.11) with these two boundary conditions. In Grundmann [75], formulas are derived for the unknown strains in the special case of pseudomorphic heterostructures with threefold rhombohedral symmetry. For quantitative predictions of those strains, the elasticity tensor C_{ijkl} of the thin film compound has to be known. Depending on the symmetry of the crystal structure, its components collapse into a lower number of independent entries. Due to symmetry reasons [70], the nine indices ij of the strain tensor can be unambiguously expressed by one index with six possible values: $11 \rightarrow 1, 22 \rightarrow 2, 33 \rightarrow 3, 23 \rightarrow 4, 13 \rightarrow 5, 12 \rightarrow 6$ [75]. This allows for a 6×6 -matrix representation of the elasticity tensor $C_{ijkl} \rightarrow C_{\mu\nu}$. For rhombohedral crystals, six independent components are left [70]. The entries of the elasticity tensor of the two sesquioxides important for this work are given in Tab. 2.3.

Table 2.3: The six independent entries of the elasticity tensor for rhombohedral Cr₂O₃ [76] and α -Ga₂O₃ [75]. All values are in units of 100 GPa.

Material	C_{11}	C_{12}	C_{13}	C_{33}	C_{44}	C_{14}
α -Cr ₂ O ₃	3.74	1.48	1.75	3.62	1.59	-0.19
α -Ga ₂ O ₃	3.82	1.74	1.26	3.46	0.78	-0.17

Because of its direct influence on the o.o.p. lattice plane distance and thus on the XRD patterns of 2θ - ω -scans (cf. 3.2), the strain component perpendicular to the sample surface, ϵ_{zz} , is of particular interest. In the following, the formulas for the case of rhombohedral crystal structures are stated as derived in Grundmann [75]. They depend on the respective i.p. strains ϵ_{xx} and ϵ_{yy} caused by the lattice mismatch between film and substrate. Note that here, $\mathbf{r} = (x, y, z)$ describes coordinates in the laboratory system – in contrary to Ref. [75], where \mathbf{r} and \mathbf{r}' are used to describe cartesian coordinates in the crystal and laboratory system, respectively.

One derives for (11.0)-plane (a -orientation):

$$\epsilon_{zz,a} = -\frac{C_{13}\epsilon_{xx,a} + C_{12}\epsilon_{yy,a}}{C_{11}}, \quad (2.12)$$

for (10.0)-plane (m -orientation):

$$\epsilon_{zz,m} = -\frac{C_{13}C_{44}\epsilon_{xx,m} + (C_{12}C_{44} + C_{14}^2)\epsilon_{yy,m}}{C_{11}C_{44} - C_{14}^2}, \quad (2.13)$$

and for (00.1)-plane (c -orientation):

$$\epsilon_{zz,c} = -\frac{2C_{13}}{C_{33}}\epsilon_{yy,c}, \quad (2.14)$$

with $\epsilon_{xx,a} = c_S/c_F - 1$ and $\epsilon_{yy,a} = a_S/a_F - 1$, depending on the lattice parameters of substrate (a_S , c_S) and film (a_F , c_F). Note that

$$\begin{aligned} \epsilon_{xx,a} &= \epsilon_{xx,m}, \\ \epsilon_{yy,a} &= \epsilon_{yy,m}, \\ \epsilon_{yy,c} &= \epsilon_{yy,a}. \end{aligned}$$

For (01.2)-plane (r -orientation), more complex relations arise as it was demonstrated by Grundmann [77]. The distance of lattice planes d orthogonal to the sample surface are then strained, such that:

$$d_{\text{strained}} = d(1 + \epsilon_{zz}). \quad (2.15)$$

Assuming pseudomorphic growth of Cr₂O₃ on Al₂O₃, one can compare the strained lattice plane distances to the unstrained bulk values, by utilizing (2.15). The numer-

Table 2.4: (a) Comparison of d and d_{str} , which are the o.o.p. lattice plane distances for bulk Cr_2O_3 and pseudomorphic Cr_2O_3 on Al_2O_3 , respectively. The corresponding o.o.p.-strain ϵ_{zz} is also given, as well as the corresponding angles of typical reflections in diffraction patterns of 2θ - ω -scans. (b) The resulting tilt of the thin film depending on substrate orientation for relaxed growth. The results are obtained from considerations on the possible slip systems and BURGER's vectors.

Orientation (X-ray reflection)	(a) Pseudomorphic					(b) Relaxed	
	d (nm)	d_{str} (nm)	ϵ_{zz} (%)	2θ ($^{\circ}$)	$2\theta_{\text{str}}$ ($^{\circ}$)	$\theta_{T,x}$	$\theta_{T,y}$
c (00.6)	13.59	14.12	3.90	39.75	38.20	—	—
a (11.0)	2.48	2.57	3.63	36.18	34.87	no	no
m (30.0)	4.30	4.45	3.67	65.06	62.49	yes	no
r (02.4)	3.63	3.72	2.41	50.19	48.93	yes	no

ical values, calculated from the lattice constants (Tab. 2.1) and the elasticity tensor (Tab. 2.3), are listed in Tab. 2.4a.

2.3.2 Relaxed Growth

Dislocations

When the lattice mismatch is not resolved by adaption to the substrate (cf. 2.3.1), the strain is relieved by formation of *dislocations*, which facilitate a relaxed growth mode of the film [78]. The highest disturbance from equilibrium spacing occurs close to the *dislocation line* which extends through the material – far away from this line, the crystallinity is restored. In which fashion the distortion happens, can be characterized by the BURGER's vector **b**. The relation of the BURGER's vector to the dislocation line determines the type of the dislocation: if they are orthogonal, one refers to an *edge* dislocation; if they are parallel, one refers to a *screw* dislocation. For a “perfect” dislocation⁽⁷⁾, the BURGER's vector is a lattice translation vector. Note that in general, dislocations exhibit both edge- and screw-character [80].

Dislocations are not static, but can move (“glide”) inside the crystal. The movement happens typically inside a plane which has highest density of atoms (“glide plane”) and along the BURGER's vector which is responsible for the dislocation [80]. The arrangement of glide plane and direction of movement is called “slip system”, e.g. for hexagonal structures, one finds $\{00.1\}/\langle 11.0 \rangle$ to be one prevailing slip system [80].

For some slip systems occurring on heterostructures, the relaxation results in an additional tilt of the deposited film. This happens because a BURGER's vector **b** has more than one component: the edge component b_{\parallel} causes strain relaxation along b_{\parallel} ; but if **b** also exhibits a component b_{\perp} orthogonal to the sample surface and the dislocation

⁽⁷⁾ Also referred to as “full” dislocation [79].

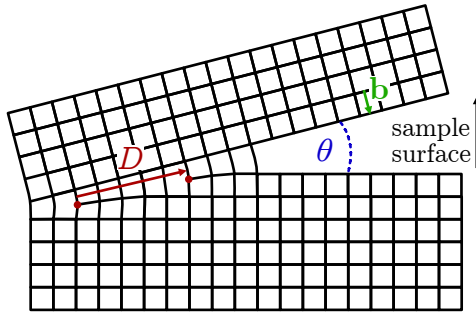


Figure 2.4: Edge dislocation with BURGER’s vector perpendicular to the sample surface. The edge dislocation lines are indicated by the red dots and are perpendicular to the image plane. Consequently, the direction of the edge BURGER’s vector is indicated by the red arrow, whose length D denotes the distance between dislocation lines. The green BURGER’s vector \mathbf{b} is the orthogonal component b_{\perp} mentioned in the text.

line, a tilt angle θ_T will result between substrate and relaxed film [78, 81]:

$$\theta_{T,i} = \epsilon_{ii} \frac{b_{i,\perp}}{b_{i,\parallel}}, \quad (2.16)$$

where i denotes the axis of strain relaxation. This is schematically depicted in Fig. 2.4. Note that Equ. (2.16) is formulated for partially relaxed systems in Kneiß *et al.* [78], but here the relaxation parameter ρ_i was omitted, therefore assuming fully relaxed thin films.

Slip Systems for Sesquioxide Heterostructures

For heteroepitaxial growth of $(\text{Al}_x\text{Ga}_{1-x})_2\text{O}_3$ with low Al content on Al_2O_3 , studies have been conducted on the prevailing relaxation mechanisms for *r*-oriented [81, 82], as well as *a*- and *m*-oriented [78] growth directions. In the following, those results will be summarized. Note that the *x*-axis points along the *c*-axis for *m*- and *a*-oriented heterostructures, and similarly along the projection of the *c*-axis on the sample surface for *r*-oriented heterostructures.

(01.2)-plane (*r*-orientation) The two relevant slip systems are $\{00.1\}/\frac{1}{3}\langle 11.0 \rangle$ and $\{11.0\}/\frac{1}{3}\langle 1\bar{1}.1 \rangle$, which contain the “basal” and “prismatic” glide plane, respectively [81]. The former allows relaxation along the direction containing the projection of the *c*-axis (*x*-axis), whereas the latter allows relaxation perpendicular to it (*y*-axis). For the basal system, one can determine two possible independent BURGER’s vectors \mathbf{b}_c with differing screw components but otherwise same tilt and edge components $b_{c,\perp}$ and $b_{c,\parallel}$, respectively. The tilt along *x*-direction can then be calculated via:

$$\theta_{T,x} = \epsilon_{xx} \frac{b_{c,\perp}}{b_{c,\parallel}} = \frac{1}{\sqrt{3}} \zeta_F \epsilon_{xx}, \quad (2.17)$$

with $\zeta_F = c_F/a_F$. For the prismatic slip system, the possible BURGER's vectors facilitate relaxation along the y -direction via $b_{a,\parallel}$. But in contrast to the basal system, the tilt components $b_{a,\perp}$ cancel out on average, thus resulting in no net tilt along the y -direction: $\theta_{T,y} = 0$.

(10.0)-plane (*m*-orientation) Neither basal (00.1) nor prismatic (11.0) and (10.0) slip systems can resolve strain along the x -axis: The (00.1)-plane is perpendicular to the surface and x -direction, thus the BURGER's vector can only have components in the y - z -plane. But for strain release along x , the BURGER's vector should have non-zero component in this direction, which cannot be the case. The prismatic planes, on the other hand, are perpendicular to the surface but parallel to the x -axis. This results in a dislocation line along the x -direction. To release strain, the BURGER's vector would have x -component, which does not apply for edge dislocations. So the prevailing slip system must have (01.2)-plane (*r*-orientation) or (11.2)-plane (*s*-orientation) character, which are called “pyramidal” slip systems. Three different *r*-planes contribute to strain release, because there is dislocation line component along the y -axis and BURGER's vector's components along the x -axis. With Equ. (2.16) and substituting the possible BURGER's vectors one finds:

$$\theta_{T,x} = \frac{2}{3} \frac{\sqrt{3}}{\frac{20\zeta}{24+6\zeta^2} + \zeta} \left(\frac{c_S}{c_F} - 1 \right) \quad (2.18)$$

(11.0)-plane (*a*-orientation) The same argument as for the *m*-oriented heterostructure holds, why only pyramidal slip systems are possible. But in this case, only two *r*-planes contribute to strain relaxation, because the third plane is perpendicular to the surface, thus can only exhibit BURGER's vectors without in-plane components which results in no possible edge dislocations. Furthermore, in this case, the BURGER's vectors of the two remaining *r*-planes have opposite tilt components, i.e. they point outwards and inwards of the surface, respectively. Regarding Equ. (2.16), this will result in no net tilt of the thin film.

Chapter 3

Experimental Methods

3.1 Pulsed Laser Deposition

PLD is a PVD technique, which utilizes absorption of laser energy by a target and subsequent condensation of evaporated target material on a substrate. Like MBE or CVD, it is used for deposition of thin film materials. Although not true in general [83], a stoichiometric transfer of target composition to the substrate is attributed to PLD. In the following, the PLD setup used for this work (Fig. 3.1a) is described. Furthermore, an overview of the basic physical processes interplaying during a PLD process is given, based on Lorenz [83].

3.1.1 Setup

The desired thin film material is provided by a ceramic pellet of the respective compound called *target*. It is fabricated by pressing powder with high pressure into cylindrical form, before it is sintered at high temperatures. The crystal growth takes place on a substrate, and in this work, the substrate is chosen to be sapphire (Al_2O_3) of different crystal orientation: *c*-, *r*-, *m*- and *a*-plane. Al_2O_3 is chosen because it matches the symmetry of the here investigated sesquioxides. They are $500\text{ }\mu\text{m}$ thick with an edge length of 5 mm. In this work, oxygen is chosen as background gas and to control the partial pressure, the process takes place in a vacuum chamber, called *PLD chamber*. Inside the chamber, a target holder is placed 90 cm opposite a sample holder, which both are capable of carrying up to four pellets and substrates, respectively. The latter is equipped with a resistive heater, allowing growth temperatures above $700\text{ }^\circ\text{C}$. To ensure homogenous ablation and deposition, both target and substrate can be rotated, whereby a frequency of 120 min^{-1} and 8 min^{-1} is chosen, respectively. Furthermore, an offset ε between the rotation centers of target and substrate is applied, i.e. the plasma plume does not hit the center of the substrate holder. To achieve homogeneous thickness distributions of the deposited material, $\varepsilon = 7.5\text{ mm}$ is chosen. Outside the PLD chamber, a KrF excimer laser produces pulsed radiation, which is redirected by

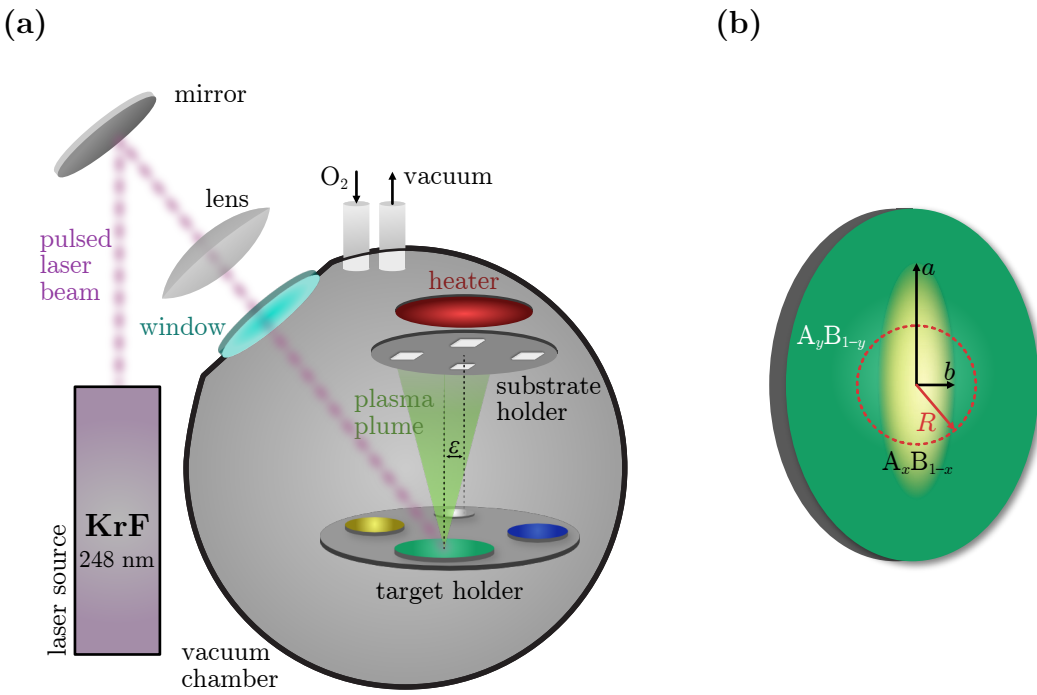


Figure 3.1: (a) Schematic of a PLD setup and (b) schematic of an elliptically segmented pellet used as target for DCS-PLD. *a* and *b* are semi-major and semi-minor axis of the ellipse, respectively. *R* denotes the radius of the circular laser spot path on the target surface. The composition of the inner and outer segment is A_xB_{1-x} and A_yB_{1-y}, respectively.

a mirror and enters the chamber through a fused silica window. With a wavelength of 248 nm, a UV lens is needed to project the beam on the target surface, where the laser energy is absorbed. By repositioning the lens, the laser spot size can be controlled. The energy per pulse can be adjusted and is several hundred mJ with a duration of about 20 ns, resulting in thousands of kW cm⁻² on the target surface [83].

The laser energy density, called fluence *F*, can be calculated by taking the energy per pulse *E* and the lens position *L* into account. For an applied *E* = 650 mJ, 75 % of the energy are absorbed by a mask, mirror, lens and entrance window⁽¹⁾. This transmittance is assumed to be independent of *E*. The resulting fluence dependence $F(E, L) = \frac{0.25E}{A(L)}$ is visualized in Fig. 4.20, whereby the laser spot size *A* was measured for some *L* and fitted by assuming parabolic behavior (Fig. 4.19).

3.1.2 Plasma Dynamics

The PLD procedure can be broken down into three physical processes: (i) energy absorption on the target surface, (ii) formation of a plasma and (iii) condensation on the substrate:

- (i) After being projected on the surface of the pellet, the radiation penetrates the material only by a fraction of a μm. Electrons are excited and oscillate in the

⁽¹⁾ This was estimated using an energy monitor device and conducted by M. Sc. J. Bredow.

electromagnetic field of the laser pulse. Those electrons collide with bulk atoms of the surface region, which are subsequently heated up and vaporize. This process is supported by breaking of chemical bonds due to laser radiation.

- (ii) A material cloud expands perpendicular to the target surface due to Coulomb repulsion and recoil. Absorption of remaining laser radiation results in a plasma plume which is strongly forward directed for low background pressures below 10^{-4} mbar. The target is rotating and laterally moving during this process to minimize the deflection of the plasma due to target degradation. The kinetic energy of the material in the plasma plume is crucial for the deposition process and can be controlled by background partial pressure and laser energy density on the target.
- (iii) The plasma plume hits the substrate which can result in resputtering of already deposited material, which condenses together with the plasma, resulting in thermal equilibrium and thus thin film nucleation. A large number of adatoms results in many nucleation centers which are responsible for smooth films.

Therefore, PLD is a non-equilibrium process, making empirical optimization of growth parameters an essential part of thin film manufacturing [83].

3.1.3 Segmented Target Approach

To provide a discrete material library – a set of different samples with homogeneous composition each –, a segmented target approach as described in Wenckstern *et al.* [84] is applied. Specifically, the Discrete Combinatorial Synthesis (DCS) method utilizes a radially segmented target, i.e. a target with distinct regions of different material composition. By varying the laser spot position on the target, different plasma compositions can be achieved. Because the target is rotating during PLD, the material distribution must be in such a way that when the radial position R of the laser on the target changes, the average ablated composition $\chi(R)$ changes. This can be realized with an elliptical segmentation, i.e. a target pellet with overall composition A_yB_{1-y} , but containing an inner ellipse with composition A_xB_{1-x} (Fig. 3.1b). By this means, any homogeneous composition $A_\chi B_{1-\chi}$ with χ between x and y can be realized with only one target. χ is related to the path lengths of the moving laser spot on the inner and outer segment, respectively. The composition in the plasma can be calculated via [84]:

$$\chi(R) = y - (y - x) \frac{2}{\pi} \arccos \left[\frac{1}{\delta} \sqrt{1 - \left(\frac{b}{R} \right)^2} \right] \quad (3.1)$$

where δ and b are eccentricity and semi-minor axis of the ellipse, respectively⁽²⁾. Small and large R will result in a composition equal to the composition of the inner and

⁽²⁾ The eccentricity is defined as $\delta = \sqrt{1 - b^2/a^2}$, where a is the length of the semi-major axis.

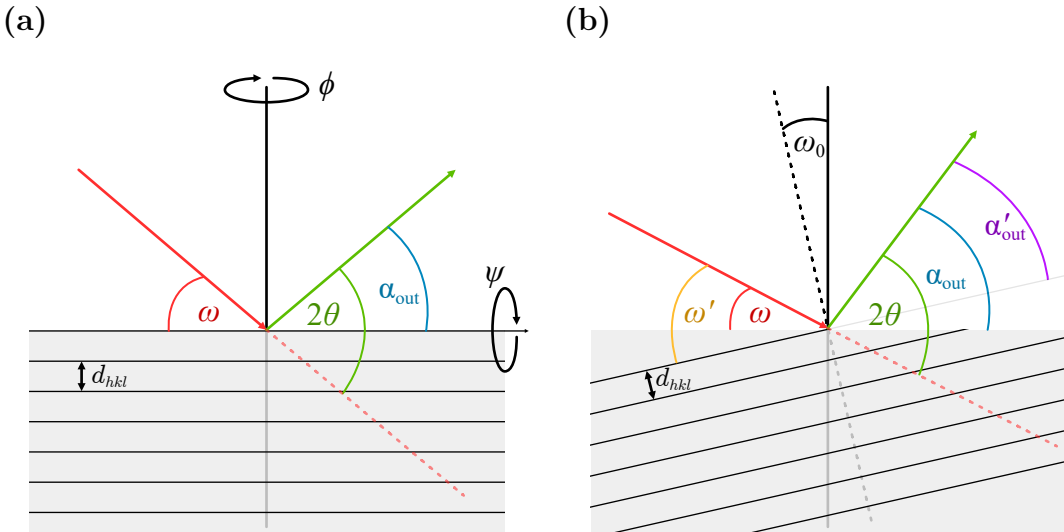


Figure 3.2: (a) Geometry for a 2θ - ω -scan without offset. (b) Scattering geometry containing an offset ω_0 . Angle of incidence and angle of diffraction decrease and increase, respectively. Note that 2θ is not affected by this offset.

outer segment, respectively. To model the process more accurately one has to take into account that the laser illuminates a finite area rather than a point-like spot. This is done in 4.2, in particular refer to Fig. 4.11.

3.2 X-Ray Diffraction Measurement

As described in 2.2.2, constructive interference of incoming and scattered X-rays may give insight into the symmetry of exposed crystal structures. This can be utilized for thin film investigation and is called XRD. The XRD device used for this work, namely an *X’Pert Pro* (Malvern Panalytical Ltd.), as well as the applied scanning techniques will be presented in the following.

The sample of interest is glued to a metallic holder which itself is placed into the shielded XRD device and exposed with X-rays at an angle ω between sample surface and incident radiation. The surface normal of the sample holder is parallel to the z -axis of the laboratory system. The diffracted radiation is measured at an angle α_{out} between sample surface and detector. 2θ is used to describe the angle between outgoing beam and the extension of the incoming beam, which both span the scattering plane. It follows that $2\theta = \omega + \alpha_{out}$. Note that θ in the BRAGG Equation (2.10) is the same angle as half of 2θ . The scattering plane is depicted in Fig. 3.2a. The sample can be rotated by ϕ (*azimuth*) and ψ around an axis parallel to the surface normal and parallel to the intersection of sample surface and scattering plane, respectively.

3.2.1 2θ-ω-scans

When probing for lattice plane distances using the BRAGG condition in its simplest form, it is assumed that the scattering planes are parallel to the sample surface (cf. Fig. 3.2a). It is necessary that $\omega = \alpha_{\text{out}}$ which implies $2\theta = 2\omega$. So the angle of incidence ω is coupled to 2θ , which represents the distance between lattice planes (cf. Equ. (2.10)). Measuring the diffracted X-ray intensity while varying 2θ and maintaining the condition $2\theta = 2\omega$, is called a *2θ-ω-scan*. This results in a *2θ-ω diffraction pattern*, where peaks correspond to constructive interference and thus to certain lattice plane distances.

When analyzing $2\theta\text{-}\omega$ diffraction patterns, one usually compares the observed reflections to predicted peak positions of the expected phase of the compound which is investigated. This reference diffraction pattern stems from powder samples of the respective compound, containing all crystal orientations during one $2\theta\text{-}\omega$ -scan. When a peak is identified, a possible peak shift is determined and the shape of the peak is investigated. Peak shifts may be due to residual stress, substrate induced strain or compositional gradients in the thin film [72]. A certain amount of peak broadening is always present due to convergence of the incident beam as well as convolution of $K\alpha_1$ - and $K\alpha_2$ -radiation (cf. 2.2.2), which is called instrumental broadening [72]. The Full Width at Half Maximum (FWHM) of the highly crystalline substrate peaks may give a reference for broadening of peaks in $2\theta\text{-}\omega$ diffraction data.

This method can be extended to measure lattice planes which are not parallel to the sample surface but tilted by ω_0 . This is done by rotating the reference frame of the sample in such a way that the BRAGG condition is fulfilled again. Note that 2θ does not change upon rotation, as can be seen in Fig. 3.2b. When probing for plane distances of the rotated lattice, one finds for the coupling between 2θ and ω :

$$\begin{aligned} \omega' &= \alpha'_{\text{out}} \\ \omega + \omega_0 &= \alpha_{\text{out}} - \omega_0 \\ \omega + \omega_0 &= (2\theta - \omega) - \omega_0 \\ \Rightarrow 2\theta &= 2(\omega + \omega_0) = 2\omega'. \end{aligned}$$

This coupling is equivalent to a $2\theta\text{-}\omega$ -scan but with an offset ω_0 applied to the angle of incidence. There are several use cases for applying an offset ω_0 :

- (i) It is assumed that ω denotes the angle between incident X-ray beam and the sample surface. But a perfect alignment between sample and sample holder is not always possible. So to correct this tilt between expected sample position and its real inclination, the offset ω_0 can be set to really probe for lattice planes parallel to the sample surface. This is done before measuring a $2\theta\text{-}\omega$ -scan to achieve more precise results.

- (ii) When probing for lattice planes which are not parallel to the sample surface, called *asymmetric reflections*, one can apply the expected inclination angle as an offset ω_0 . This is the case in Fig. 3.2b.
- (iii) When 2θ is fixed, but ω_0 is varied, an ω -*scan* is performed, which enables quantification of mosaicity (cf. 3.2.2).

3.2.2 ω -scans

Thin films may exhibit a distribution of lattice plane inclination, called mosaicity. This results in an observation of diffraction peaks for several offsets ω_0 . The mosaicity can thus be quantified by fixing 2θ , representing a certain lattice plane distance, and then vary ω_0 and measure the X-ray intensity. This is called an ω -*scan*, and the FWHM of the observed diffraction pattern (also called *Rocking curve*) is a measure for the mosaicity [72]. ω -scans are particularly useful when comparing a set of thin films of varying deposition parameters to optimise growth conditions. In particular, recording Rocking curves of symmetric and asymmetric lattice planes allows the calculation of dislocation densities in the thin film [85].

3.2.3 ϕ -scans

A 2θ - ω -*scan* is not capable of resolving in-plane rotations of crystal domains, because the distance of lattice planes parallel to the surface are not affected. Those rotational domains can be detected by probing for lattice planes which are inclined with respect to the surface, i.e. by fixing 2θ to the expected lattice plane distance and ω_0 to the inclination angle (cf. Fig. 3.2b). Depending on the symmetry of the inspected material, constructive interference should only appear for distinct values of ϕ . So by rotating the sample by 360° and simultaneously recording the X-ray intensity, a ϕ -*scan* (also called *Azimuth-scan*) can yield information about the existence of rotational domains. If the number of observed peaks in the ϕ -*scan* diffraction pattern exceeds the theoretically expected number for a single crystal, rotational domains are present [72]. Furthermore, comparing the ϕ -*scan* diffraction data of thin film and substrate reveals whether the film has grown with an in-plane rotation with respect to the substrate. Finally, if the thin film grows in a tilted manner on the substrate, a ϕ -*scan* prior to an ω -*scan* can ensure the correct positioning before alignment. Then, the BRAGG condition is fulfilled for performing a 2θ - ω -*scan*.

3.2.4 Reciprocal Space Maps

Because the BRAGG condition is equal to the description of diffraction with $\mathbf{k}' - \mathbf{k}$ and reciprocal space vectors \mathbf{K}_{hkl} (cf. 2.2.2), both can be used depending on context. Henceforth, $\mathbf{k}' - \mathbf{k}$ will be denoted by the *scattering vector* \mathbf{q} . Note that \mathbf{k} and \mathbf{k}' are

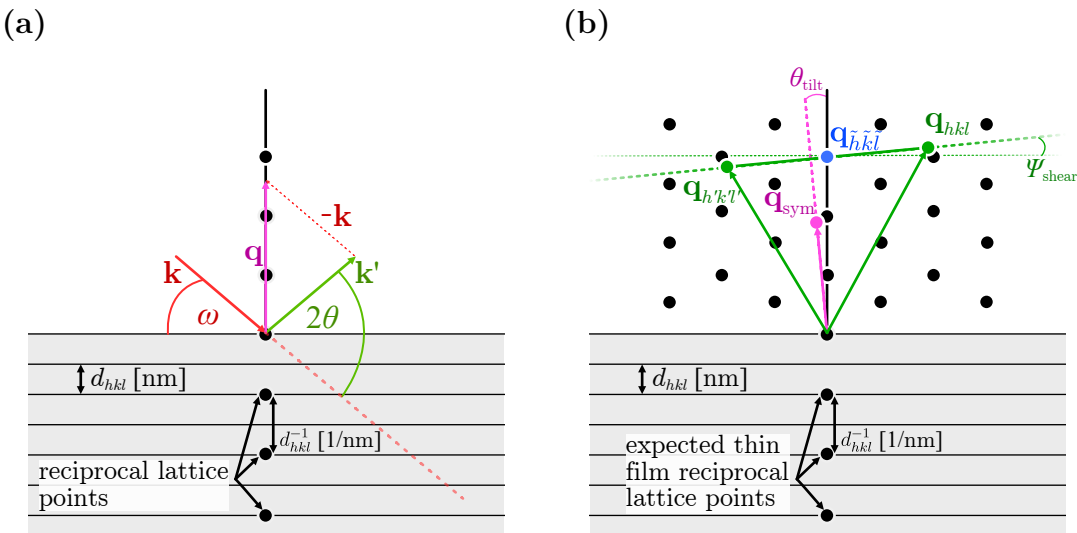


Figure 3.3: (a) Construction of the scattering vector (magenta) from incoming (red) and outgoing (green) beam, according to Equ. (3.4). The reciprocal lattice points are visualized together with the lattice planes. It has to be noted that the distances between lattice planes and between reciprocal lattice points have different dimensions. (b) Expected reciprocal lattice (black circles) and different deviations due to lattice distortions: Thin film tilt can be determined from symmetric reflections (magenta). However, shear angles do not manifest in symmetric reflections (blue), but in asymmetric reflections (green).

parallel to incoming and outgoing beam, respectively. From the definition of angles, it follows that

$$\mathbf{q} = \begin{pmatrix} q_{\parallel} \\ q_{\perp} \end{pmatrix} = \mathbf{k}' - \mathbf{k} \quad (3.2)$$

$$= \frac{1}{\lambda} \begin{pmatrix} \cos \alpha_{\text{out}} \\ \sin \alpha_{\text{out}} \end{pmatrix} - \frac{1}{\lambda} \begin{pmatrix} \cos \omega \\ -\sin \omega \end{pmatrix} \quad (3.3)$$

$$= \frac{1}{\lambda} \begin{pmatrix} \cos(2\theta - \omega) - \cos(\omega) \\ \sin(2\theta - \omega) + \sin(\omega) \end{pmatrix}. \quad (3.4)$$

From Equ. (3.4), two properties follow for the scattering vector:

$$-q_{\parallel}/q_{\perp} = -\tan \left(\omega - \frac{2\theta}{2} \right) = \tan \omega_0 , \quad (3.5)$$

$$|\mathbf{q}| = \sqrt{q_{\parallel}^2 + q_{\perp}^2} = \frac{1}{\lambda} 2 \sin \theta \stackrel{\text{Bragg}}{=} \frac{1}{d_{hkl}}, \quad (3.6)$$

where the last equality of Equ. (3.6) holds, if \mathbf{q} is a reciprocal lattice vector \mathbf{K}_{hkl} . The scattering vector, together with the corresponding XRD geometry is depicted in Fig. 3.3a. Because 2θ and ω can simultaneously be represented by \mathbf{q} , it is possible to measure intensities for several \mathbf{q} , such that a part of the reciprocal space $Q \ni \mathbf{q}$ is mapped. Consequently, this is called a RSM. According to Equ. (2.9), a peak in 2D

reciprocal space Q should be observed if \mathbf{q} is a reciprocal space vector. In this case, $\mathbf{q} = \mathbf{K}_{hkl}$ is called a *reflection*. With Equ. (3.5) one can determine ω_0 – the direction of the corresponding lattice planes – and with Equ. (3.6) the lattice plane distance d_{hkl} can be calculated. Note that for rhombohedral crystals, d_{hkl} can also be predicted from the lattice constants a and c with the following equation [75]:

$$d_{hkl} = \left(\frac{4}{3} \frac{h^2 + k^2 + hk}{a^2} + \frac{l^2}{c^2} \right)^{-1/2}. \quad (3.7)$$

The inclination with respect to the c -axis can be determined via [81]

$$\alpha_{hkl|c} = \arccos \left(\frac{l}{\sqrt{\frac{4c^2}{3} \frac{h^2+k^2+hk}{a^2} + l^2}} \right). \quad (3.8)$$

A 2θ - ω -scan corresponds to a set of \mathbf{q} with fixed direction in reciprocal space, but varying length. For scanning symmetric reflections, \mathbf{q} is parallel to the surface normal (as in Fig. 3.3a). On the other hand, an ω -scan corresponds to a set \mathbf{q} with fixed length but varying direction. Therefore, the mosaicity can be approximately quantified by the broadening of a reflection perpendicular to the direction of \mathbf{K}_{hkl} . Because anisotropic strain has an effect on direction and length of inclined lattice planes, asymmetric reflections, i.e. $\omega_0 \neq 0$, can be deconvoluted into an in-plane and out-of-plane component. By this means, RSMs enable the calculation of lattice constants. To precisely calculate the latter, several corrections are applied to the recorded RSMs, as proposed in Kneiß *et al.* [78]:

1. High-quality sapphire substrates are used for deposition of thin films. It can be assumed that they have the expected crystal structure of bulk α -Al₂O₃ (cf. Tab. 2.1). So any deviation of the observed reflection $\mathbf{q}_{hkl}^{\text{Al}_2\text{O}_3,\text{obs}}$ from the expected peak position $\mathbf{q}_{hkl}^{\text{Al}_2\text{O}_3,\text{lit}}$ is corrected by a rotation \mathbf{R} and scaling ρ of reciprocal space Q :

$$\mathbf{q}^{\text{cor}} = \rho \mathbf{R} \cdot \mathbf{q}^{\text{obs}} \quad , \quad \mathbf{q}^{\text{obs}} \in Q, \quad (3.9)$$

with

$$\mathbf{R} = \begin{pmatrix} \cos \gamma & -\sin \gamma \\ \sin \gamma & \cos \gamma \end{pmatrix} \quad , \quad \gamma = \arccos \left(\frac{\mathbf{q}_{hkl}^{\text{Al}_2\text{O}_3,\text{lit}} \cdot \mathbf{q}_{hkl}^{\text{Al}_2\text{O}_3,\text{obs}}}{|\mathbf{q}_{hkl}^{\text{Al}_2\text{O}_3,\text{lit}}| \cdot |\mathbf{q}_{hkl}^{\text{Al}_2\text{O}_3,\text{obs}}|} \right) \quad (3.10)$$

$$\rho = \frac{|\mathbf{q}_{hkl}^{\text{Al}_2\text{O}_3,\text{lit}}|}{|\mathbf{q}_{hkl}^{\text{Al}_2\text{O}_3,\text{obs}}|}. \quad (3.11)$$

2. If the thin film grows tilted (e.g. due to slip systems, cf. 2.3.2), a symmetric reflection – having scattering vector parallel to the surface normal in theory – will exhibit an in-plane component $q_{\parallel,hkl}^{\text{film}} \neq 0$. The tilt angle can be calculated

by Equ. (3.5):

$$\theta_{\text{tilt}} = \arctan \left(-\frac{q_{\parallel,hkl}^{\text{film}}}{q_{\perp,hkl}^{\text{film}}} \right). \quad (3.12)$$

To determine the lattice constants from asymmetric peaks, the reciprocal space is again rotated as in Equ. (3.10) but with rotation angle $-\theta_{\text{tilt}}$. This scenario is depicted in Fig. 3.3b, where the magenta colored reflection deviates from the expected symmetric position.

3. If the thin film is sheared, a symmetric reflection $\mathbf{q}_{\tilde{h}\tilde{k}\tilde{l}}^{\text{film}}$ will be unaffected. On the contrary, an asymmetric reflection with both in- and out-of-plane component is affected. To get reliable results for the lattice constants, this shear angle Ψ_{shear} has also to be corrected, and can be calculated from two inclined lattice planes (hkl) and $(h'k'l')$, i.e. scattering vectors with non-zero in-plane component. Those vectors must have symmetry of a mirror plane perpendicular to the scattering plane⁽³⁾. The geometry is depicted in Fig. 3.3b, with the blue and green reflections representing the symmetric and asymmetric reflections, respectively. The shear angle can be calculated with

$$\Psi_{\text{shear}} = \arctan \left(\frac{q_{\perp,hkl}^{\text{film}} - q_{\perp,h'k'l'}^{\text{film}}}{q_{\parallel,hkl}^{\text{film}} - q_{\parallel,h'k'l'}^{\text{film}}} \right). \quad (3.13)$$

To correct the shear, a rotation around the corresponding symmetric reciprocal lattice point $\mathbf{q}_{\tilde{h}\tilde{k}\tilde{l}}^{\text{film}}$ with the same expected out-of-plane component must be applied.

3.2.5 Technical Details

For the results presented in this work, the radiation was produced by an copper anode, resulting in a wavelength of $\lambda = 1.5406 \text{ \AA}$ for Cu-K α_1 radiation. Note that Cu-K α_2 and Cu-K β radiation is not filtered out, resulting in additional low-intensity peaks in the diffractograms. Furthermore, contamination of the anode with tungsten results in an observable W-L α_1 contribution with energy between Cu-K α - and Cu-K β -radiation. During the course of the conducted experiments, the contaminated anode has been replaced, so the peaks corresponding to W-L α_1 -radiation are not present in every diffractogram.

The diffracted radiation is detected with a *PIXcel^{3D}* (*Malvern Panalytical Ltd.*) detector. For 2θ - ω -scans (cf. 3.2.1), the detector is operating in **Scanning Line** mode. For scans fixing the 2θ position, i.e. ω - (cf. 3.2.2) and ϕ -scans (cf. 3.2.3), the detector is operated in **Receiving Slit** mode. RSMs are recorded with the **Frame Based** mode. The settings for the various scans are listed in Tab. 3.1. Note that it is distinguished between scans and optimizations. The latter were applied for aligning the sample

⁽³⁾ This can be achieved by probing for a plane (hkl) and then rotate the sample around ϕ by 180° .

Table 3.1: Configurations for the applied XRD scans.

scan type	detector mode	step size ($^{\circ}$)	active channels	effective width
2 θ - ω -scan	1D Scanning Line	0.005	255	2.51 $^{\circ}$
ω -scan	0D Receiving Slit	0.005	55	3.025 mm
ω -optimization	0D Receiving Slit	0.02	37	2.035 mm
ϕ -scan	0D Receiving Slit	0.05	55	3.025 mm
ϕ -optimization	0D Receiving Slit	0.5	55	3.025 mm
RSMs	1D Frame Based	0.005	255	2.51 $^{\circ}$

correctly, depending on the measurement. For example, before a 2 θ - ω -scan of m -plane oriented rhombohedral samples, a ϕ -scan has been applied for the inclined (30.6) reflection to find the correct azimuth of the c -axis, which is called ϕ -optimization. Afterwards, a Rocking curve has been recorded and ω set to the maximum of the peak to compensate for the expected lattice tilt (cf. 2.3.2), called an ω -optimization.

3.3 Thermal Evaporation

The ohmic contacts for electrical characterization of Cr₂O₃ thin films were deposited by means of thermal evaporation, which is a PVD method. This method is well established for contacting α -Ga₂O₃ thin films [28]. Experiments on the ohmic behavior of evaporated contacts on Cr₂O₃ were conducted and linear U vs. I curves were obtained for conducting samples (not shown). The thermal evaporation method utilizes a *boat* made of a material with high melting temperature (tungsten or molybdenum) that is loaded with the target material in form of powder or filament. A vacuum chamber is used to achieve pressures of around 5×10^{-5} mbar. A high current is driven through the contacted boat, such that resistive heating ensures melting of the target material and subsequent evaporation. The evaporated material spreads out due to the pressure gradient and condensates on the sample which is mounted to a rotating holder. A metal mask ensures that only the corners of the sample are contacted.

The contacts are either a stacking of titanium, aluminum, and gold (henceforth referred to as *Ti-Al-Au*) or only titanium and gold (*Ti-Au*). The thickness of each material layer is around 30 nm, measured with a crystal oscillator during the process. The currents used for evaporating Ti, Al and Au are 60 A, 50 A and 45 A, respectively.

3.4 Resistivity Measurement

As shown by van der Pauw [86], it is possible to determine the specific resistivity of a flat sample by only making four small contacts at arbitrary points at its edge and

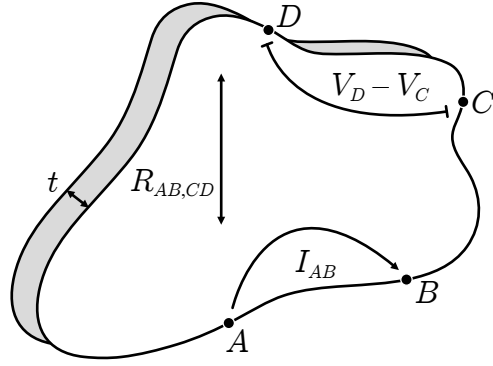


Figure 3.4: The geometry for measuring the specific resistance of a thin film as proposed by van der Pauw [86].

measure the thickness t as well as the following resistances⁽⁴⁾:

$$R_{AB,CD} = \frac{V_D - V_C}{I_{AB}} \quad , \quad R_{BC,DA} = \frac{V_A - V_D}{I_{BC}} , \quad (3.14)$$

where $V_D - V_C$ is the potential difference between points C and D , measured while applying I_{AB} , the current entering the sample at point A and leaving it at point B . The geometry is depicted in Fig. 3.4a. Note that Equ. (3.15) is restricted to these conditions: “(a) The contacts are at the circumference of the sample. (b) The contacts are sufficiently small. (c) The sample is homogeneous in thickness. (d) The surface of the sample is singly connected, i.e., the sample does not have isolated holes.” (van der Pauw [86]) The specific resistivity ρ can then be calculated via

$$\rho = \frac{\pi t}{\ln 2} \frac{R_{AB,CD} + R_{BC,DA}}{2} \cdot f \left(\frac{R_{AB,CD}}{R_{BC,DA}} \right) , \quad (3.15)$$

where f is a function equal to 1, if the two measured resistances are equal; f decreases for higher ratios of the two measured resistances [86]. The geometry can further be used to determine the Hall mobility μ_H and carrier concentration n , but due to low conductivities of the here investigated Cr_2O_3 thin films, this method yields no reliable information about μ_H and n .

Temperature-dependent resistivity measurements were conducted with a Hall probe station *CRX-VF* controlled by the measurement setup *HM-8425* (Lake Shore Cryotronics, Inc.), cooled via a *Model 336 cryogenic temperature controller* (Lake Shore). The samples were measured in a vacuum and the temperature could be controlled between 10 K and 390 K.

⁽⁴⁾ The unit of those quantities is Ω , thus the name.

3.5 Thickness Determination

spectroscopic ellipsometry is a method to measure the optical constants and thickness t of a thin film by the change of polarization state upon light reflection. If the probing light covers several wavelengths at once, one refers to spectroscopic ellipsometry, which will be presented in the following, based on Fujiwara [87]. The incoming light can be represented by an electromagnetic wave, decomposed into two components being parallel (p) and perpendicular (s) to the scattering plane:

$$\mathcal{E} = \mathcal{E}_{\text{ip}} + \mathcal{E}_{\text{is}}. \quad (3.16)$$

In general, the amplitudes of p- and s-polarized light change in a different manner after reflection, so the overall polarization of the reflected light is changed. This change is described by the fraction

$$\rho = \frac{r_p}{r_s} := \tan \Psi \cdot \exp(i\Delta), \quad (3.17)$$

where r_p and r_s are the amplitude reflection coefficients⁽⁵⁾ for the p- and s-polarized component, respectively. For simple structures, Ψ is essentially the refractive index n , and Δ represents the extinction coefficient k . In general, they can be calculated from the JONES-matrix – representing the reflection – and depend on the angle of incidence as well as the photon energy.

To determine the sample thickness, the spectra of Ψ and Δ can be generated using a model for the sample structure, which is then fitted to the experimental data. In this work, this model consists of an Al_2O_3 substrate without backscattering from the backside (infinite thickness); a Cr_2O_3 thin film of thickness t ; and a mixed layer of air and Cr_2O_3 , approximating the roughness of the sample. Because the measured spectra were confined to the visible regime of the thin film (approx. < 2.8 eV), one can apply the CAUCHY model [87], approximating the refractive index by

$$n(\lambda) = A + \frac{B}{\lambda^2} + \frac{C}{\lambda^4} + \mathcal{O}(\lambda^{-6}) \quad , \quad k = 0. \quad (3.18)$$

The spectroscopic ellipsometry measurements were performed with an *M-2000VI* (J.A. Woolam Co., Inc.) and the data was analyzed using the software *WVASE* (J.A. Woolam). The angles of incidence were chosen to be 50°, 60° and 70°, and the modelled spectral range is 0.75 to 2.8 eV. If samples of different orientation were fabricated in the same process, one can assume similar thicknesses, and a measurement with three angles was conducted only for one sample of the batch. The other samples were measured with only one angle, if the determined thickness did not differ significantly from the more accurately measured one.

Note that the investigated thin films are not isotropic in general, which is why the validity of the determined thickness is checked by profilometer measurements with a

⁽⁵⁾ They are defined by the amplitude of incoming (i) and reflected (r) radiation: $r = |\mathcal{E}_r|/|\mathcal{E}_i|$.

Dektak XT Stylus Profiler (Bruker Corporation). The edges of the quadratic substrates are masked by the sample holder during deposition, which is why they are not deposited with the target material. Consequently, measuring the height profile ranging from an edge to coated regions of the sample yields an approximation for t by the height of the observed step edge.

3.6 Spectral Transmission

For optical characterization, spectral transmission measurements were conducted: Monochromatic light is used to compare a reference beam with the intensity of radiation transmitting a sample of thickness t . The fraction of both is defined as the transmittance $T(E)$, which depends on the photon energy $E = \hbar\omega$. In a simple model, neglecting reflection on the sample surface as well as thin film interference [88], the absorption coefficient α can be defined via the LAMBERT-BEER-law:

$$T \propto e^{-\alpha t}, \quad (3.19)$$

which states an exponential decay of intensity with increasing thickness t . The absorption coefficient is based on the transition rate between valence band and conduction band at photon energy E . This rate depends on the energy-dependent coupling matrix element for this transition, as well as the joint electron and hole density of states (DOS) [89]. If matrix element and DOS are assumed to be constant and parabolic, respectively [90], then $\alpha = 0$ for energies below the band gap, and for direct transitions it follows [89]:

$$\alpha \propto (E - E_g)^{1/2}. \quad (3.20)$$

For indirect transitions, phonons with energy $\hbar\Omega$ must be considered which leads to

$$\alpha \propto (E + \hbar\Omega - E_g)^2. \quad (3.21)$$

In general, it has to be noted that those equations are affected by several approximations: no COULOMB interaction between holes and electrons is considered; defect states that could enable absorption below E_g are neglected; the parabolic nature of the DOS is only true for $k \approx 0$ and not for large energies $\hbar\omega \gg E_g$ [89]. Due to those considerations, the “band gap” constant occurring in Equ. (3.20) and Equ. (3.21) will be referred to as *optical gap* E_{opt} , or *optical absorption edge*. Both equations allow extrapolating an $\alpha^{1/\eta}$ vs. E plot to the abscissa to determine the optical gap, with $\eta = \frac{1}{2}$ and $\eta = 2$ for direct and indirect transitions, respectively [89]. According to Zanatta [89], these two methods are often mislabeled as TAUC plots $\alpha^{1/\eta}$ vs. E and were applied to determine the band gap of crystalline solids [24, 39, 45, 58]. But actually, those methods are based on the description of *crystalline* solids, whereas the original “TAUC plot” was an empirical description of *amorphous* germanium, leading to an $(\alpha E)^{1/2}$ vs. E plot [90].

Therefore, applying the TAUC method to crystals is inappropriate – it can be only used if localized energy states are present, as in amorphous solids or nanoparticles [91]. In this work, a direct band gap of Cr₂O₃ is assumed and therefore the α^2 vs. E plot is utilized. This is described in more detail in 4.1.

Due to the fact that the intersection of

$$\alpha = \text{const.} \cdot (E - E_{\text{opt}})^{1/2}$$

with the abscissa does not depend on the value of const., the α^2 vs. E plots are visualized with arbitrary units on the ordinate.

The measurements were conducted in a spectral range of 200 to 2800 nm, realized by two light sources with a *Lambda 40* (Perkin-Elmer). The spectra are corrected with a corresponding reference substrate. The measurements were done by M. Hahn.

3.7 Further Measurement Methods

Reflection High-Energy Electron Diffraction (RHEED) is a method to probe the crystal structure of only a few monolayers below the surface of a thin film. High-energy electrons are pointed in grazing incidence geometry on the sample surface and the diffracted electrons are detected with a fluorescent screen. The image of the screen is called the RHEED pattern and it can yield information about the symmetry and crystallinity of the sample surface [92].

Transmission Electron Microscopy (TEM) is a method for providing highly magnified images of solid state samples. The method utilizes a beam of high energy electrons that is passing through an sufficiently thin sample. Resolutions of 0.08 nm can be achieved due to the shorter wavelength of electrons compared to visible light [93]. A scanning TEM method is High-Angle Annular Dark-Field Imaging (HAADF), where scattered electrons are detected with an annular dark field detector. The HAADF images in this work were kindly performed by Dr. J. G. Fernandez.

Chapter 4

Experiment, Results and Discussion

4.1 Growth Window for Cr₂O₃ Deposition on Saphire

In the first part of this work, the feasibility of depositing Cr₂O₃ thin films via PLD as well as their resulting physical properties are investigated. Because Cr₂O₃ is the most stable chromium oxide, its formation is expected, but other oxidation states cannot be excluded. E.g., in Fig. 4.13, a silver colored target coating can be observed, presumably corresponding to metallic CrO₂. If Cr₂O₃ is the only oxidation state, then amorphous or rhombohedral films are expected, because no other polymorph of Cr₂O₃ exists. Furthermore, it is investigated whether Al₂O₃ and Cr₂O₃ exhibit the same crystal orientation. Finally, deposition parameters should be optimized to obtain the best crystal quality.

4.1.1 Experiment

Due to the similar crystal structure of Cr₂O₃ and α -Ga₂O₃, the deposition parameters of the latter were chosen as a starting point to deposit chromia thin films on $10 \times 10 \text{ mm}^2$ sapphire substrates with *m*-plane orientation [27]. Namely, a pulse energy of 650 mJ and a pulse frequency of 20 Hz were applied for a total of 30 000 pulses. To investigate the influence of deposition parameters, three batches were produced:

1. variation of oxygen partial pressure $p(\text{O}_2)$ from 8×10^{-5} to 1×10^{-2} mbar with a fixed heater temperature of 745 °C,
2. variation of heater temperature from 725 to 765 °C with a fixed oxygen partial pressure of 1×10^{-3} mbar, and
3. variation of substrate orientation between *c*- (00.1), *r*- (01.2) *m*- (10.0) and *a*-plane (11.0) $5 \times 5 \text{ mm}^2$ sapphire substrates⁽¹⁾ with a fixed oxygen partial pressure of 1×10^{-3} mbar and a growth temperature of 715 °C.

⁽¹⁾ In the following, the BRAVAIS-MILLER-indices will be omitted.



Figure 4.1: Image of the samples produced at different oxygen partial pressures ($T = 740^\circ\text{C}$) and different heater temperatures ($p(\text{O}_2) = 1 \times 10^{-3} \text{ mbar}$), as denoted in the image.

Photographs of the first two batches are depicted in Fig. 4.1. Structural properties of those thin films were determined by 2θ - ω -scans, ω -scans and ϕ -scans. The thickness was determined via spectroscopic ellipsometry, and transmission spectra were recorded for two samples of the 1st batch to determine the optical band gap. By dividing the thickness by the number of applied pulses, the growth rate g can be calculated as is provided in units of pm pulse⁻¹. Temperature dependent resistivity measurements were performed only for the samples of the 3rd batch, because all *m*-plane oriented samples showed no conductivity at room temperature.

4.1.2 Oxygen Partial Pressure Variation on *m*-plane Sapphire

In the following, the results for the samples produced at four different oxygen partial pressures are analyzed. In Fig. 4.2, the 2θ - ω -patterns are depicted. For each pattern, the two peaks (solid line) at around 68° correspond to the (30.0) reflection of the *m*-plane oriented sapphire substrate. The splitting occurs due to the similar wavelength of Cu-K α_1 and Cu-K α_2 radiation. The additional peaks also stem mainly from the (30.0) reflection of Al₂O₃ and are caused by W-L β_2 -, W-L β_1 -, Cu-K β -, W-L α_1 - and W-L α_2 -radiation (increasing angles). In the vicinity of the calculated peak position for the (30.0) reflection of Cr₂O₃ (cf. 2.4), there is a peak observed for each sample, indicating that the α -phase of Cr₂O₃ is present. Note that the peak position is varying depending on the chosen oxygen partial pressure. The difference to the expected peak position $2\theta_0$ is expressed as o.o.p. strain ϵ_{zz} using the Bragg equation Equ. (2.10) and then

$$\epsilon_{zz} = \frac{d - d_0}{d_0} = \left(\frac{1}{\sin(2\theta/2)} - \frac{1}{\sin(2\theta_0/2)} \right) \cdot \sin(2\theta_0/2). \quad (4.1)$$

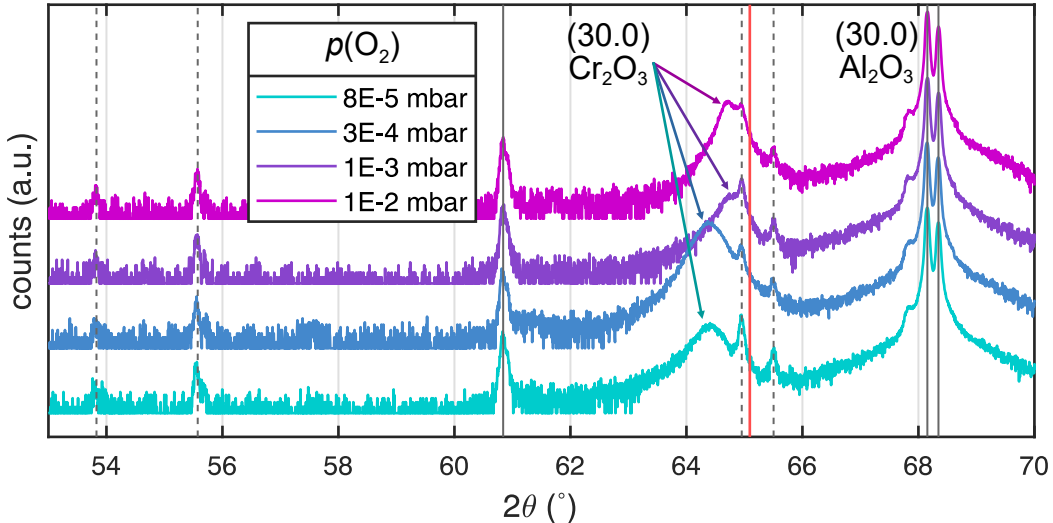


Figure 4.2: $2\theta-\omega$ -patterns of Cr_2O_3 thin films deposited on *m*-plane sapphire for various oxygen partial pressures. The gray solid lines indicate (30.0) substrate reflections corresponding to copper radiation, whereas the gray dashed lines indicate (30.0) substrate reflections corresponding to tungsten radiation. The red line corresponds to the predicted (30.0) reflection of Cr_2O_3 .

In Fig. 4.3a, the calculated strain is shown in dependence of the corresponding oxygen partial pressure (black circles). The strain decreases from approx. 0.95 % to 0.45 % with increasing pressure. This strain reduction may therefore be the result of increased background gas scattering which results in less kinetic energy of the specimen reaching the heated substrate (cf. 3.1.1).

For each sample, the 2θ angle was fixed to the observed (30.0) reflection of Cr_2O_3 and an ω -scan was performed. The FWHM of the ω -patterns (henceforth ω -FWHM) are depicted in Fig. 4.3a (orange triangles). The values vary between approx. 30' and 50' and show a dependence on oxygen partial pressure, which is less pronounced compared with o.o.p. strain. Still, since ω -FWHM is connected to the mosaicity of the thin film, higher oxygen partial pressures yield slightly better crystal qualities. Note that due to the fact that an oxygen partial pressure of 1×10^{-3} mbar yielded the best crystal quality, this value is used for future deposition processes.

To probe for rotational domains of the thin films, ϕ -scans were performed by fixing 2θ , ω and χ to the corresponding angles of the (10.2) reflection of Cr_2O_3 . The diffraction patterns are depicted in Fig. 4.4. The observed peaks of the thin film align with the peaks of the single crystal substrate, indicating that the film has no in-plane rotation with respect to the substrate. Furthermore, the absence of additional peaks indicates that there exists only a single domain of the thin film.

The growth rate g varies between 3 pm pulse^{-1} and 7 pm pulse^{-1} and no systematic dependence on the oxygen partial pressure can be observed. This is not expected, because the background pressure is related to scattering of the plasma species, which should alter the kinetic energy and therefore the growth dynamics. This behavior is attributed to reduced laser fluence on the target due to window coating, as it will be

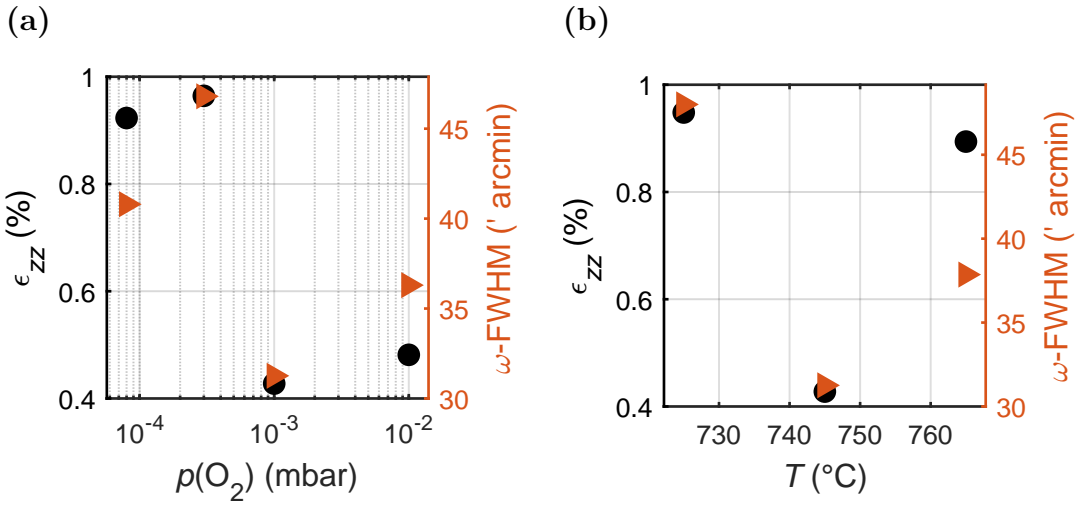


Figure 4.3: (a) Out-of-plane strain and ω -FWHM for the samples fabricated at different oxygen pressures. (b) Out-of-plane strain and ω -FWHM for the samples fabricated at different growth temperatures.

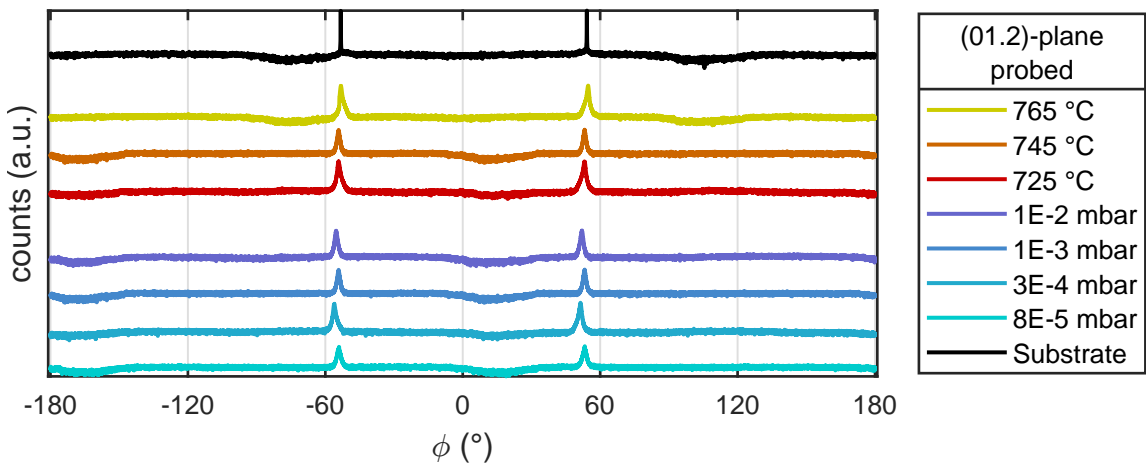


Figure 4.4: Diffraction patterns of ϕ -scans performed on the inclined (01.2) reflection for m -plane oriented Cr_2O_3 samples (color). The corresponding pattern of the Al_2O_3 substrate is also depicted (black). The diffraction patterns cover the samples from variation of oxygen partial pressure (teal to blue colored) and variation of growth temperature (red to yellow colored).

explained below.

The transmission spectra of two selected Cr_2O_3 thin films are shown in Fig. 4.5a. The samples are not fully transparent in the visible spectrum (80 % transmission at 400 nm) and they exhibit a green tint, as can also be seen in Fig. 4.1. To determine the onset of absorption E_{opt} , an α^2 vs. E plot (Fig. 4.5b) is utilized (cf. 3.6). Although the publications used for reference in this work support the direct transition nature of Cr_2O_3 [24, 41], it has to be noted that there exist studies determining the optical band gap of Cr_2O_3 by assuming an indirect transition nature [39, 45]. However, all of them utilize a TAUC plot ($\alpha E)^{\eta}$ vs. E , which is an unappropriate method for crystalline solids as discussed in 3.6. Therefore, the method based on the assumption of parabolic shape of bands as well as direct transitions (cf. 3.6) is used. Fitting the linear regime between 3.75 eV and 4.3 eV results in $E_{\text{opt}} \approx 3.6$ eV for both samples, which differ in strain and ω -FWHM by a factor of approx. 2 and 0.3, respectively. A second absorption edge can be identified between 5.3 eV and 5.5 eV and yields an optical gap of $E_{\text{opt}} \approx 5.1$ eV for both samples.

4.1.3 Growth Temperature Variation on *m*-plane Sapphire

In the following, the results for the three samples produced at different growth temperatures are presented. In addition to the oxygen partial pressure, the influence of growth temperature is investigated. Similar to the previous results, the (30.0) reflection of the α -phase of Cr_2O_3 can be observed (Fig. 4.6). The calculated o.o.p. strain is shown in Fig. 4.3b and a large spread of strain can be observed, varying between 0.4 % and 1 %. Note that there is no systematic dependence on growth temperature. The ω -FWHMs of the Cr_2O_3 (30.0) reflection are shown in Fig. 4.3b and exhibit a similar spread as the samples with varying oxygen partial pressure, but similar to the o.o.p. strain, no dependence on growth temperature is observed. The ϕ -scans (Fig. 4.4) show that the thin films are in-plane aligned with the respective substrate and that no rotational domains are present. Finally, the growth rate varies between 3.5 pm pulse⁻¹ and 10 pm pulse⁻¹ with no observable dependence on growth temperature.

4.1.4 Influence of Growth Rate on Crystal Structure

It has to be noted that there is a large spread in strain, ω -FWHM and growth rate for the samples that were deposited at different growth temperatures. The range of temperature variation was only 40 °C and has no significant influence on the distribution of strain and ω -FWHM (Fig. 4.3b). Note that for the last two samples produced with heater temperatures of $T = 725$ °C and $T = 765$ °C, respectively, the pulse number was increased to 40 000 pulses, leading to thicker samples. But the crystal structure does not depend on thickness either (not shown). Because all the other process parameters were kept the same, this indicates that another parameter influences the crystal quality.

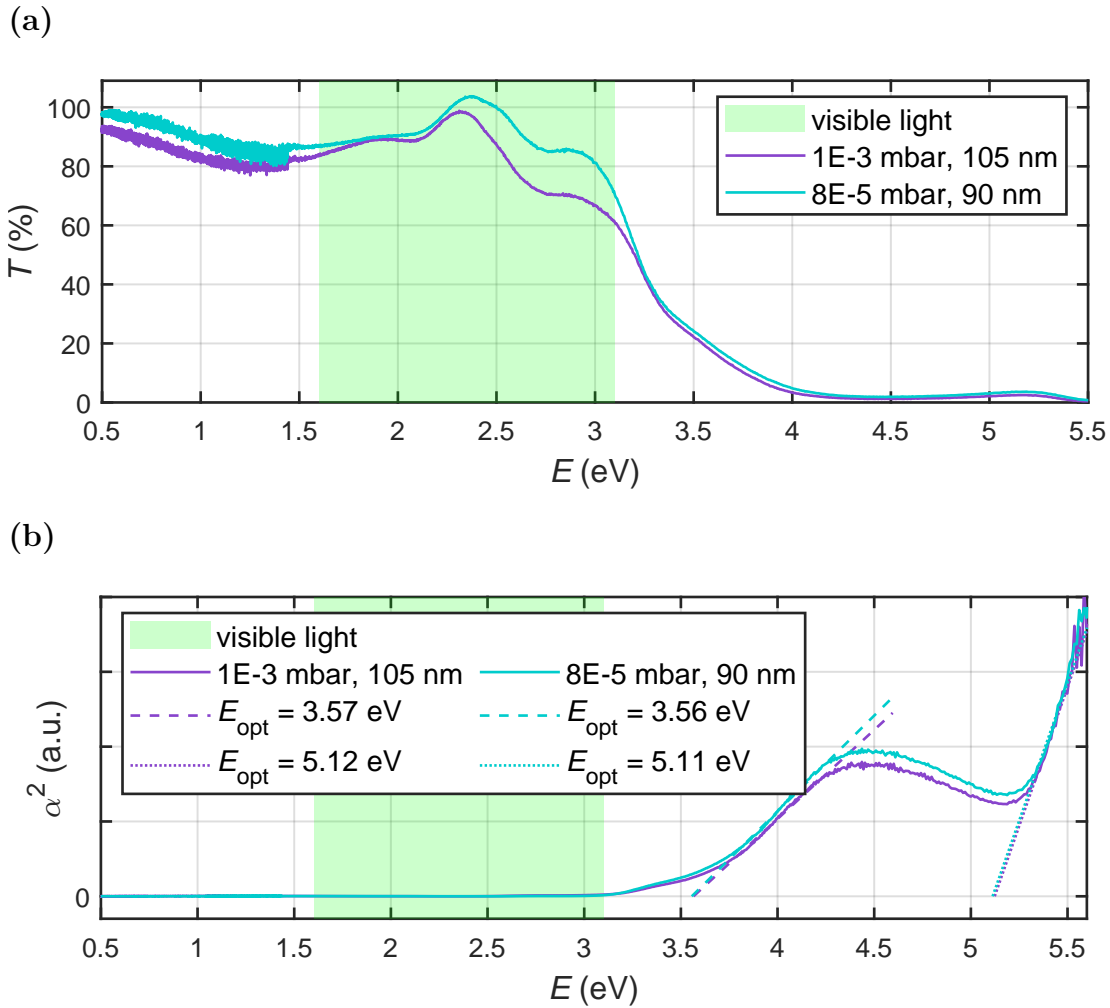


Figure 4.5: (a) Transmission spectra of two selected Cr₂O₃ thin films, deposited with different oxygen partial pressures of 1×10^{-3} mbar and 8×10^{-5} mbar. The spectra are normalized to a corresponding uncoated *m*-plane sapphire substrate. No correction to film thickness was done, which results in a lower transmittance of the thicker sample (purple). (b) α^2 vs. E plot of the above-mentioned samples. It is assumed that Cr₂O₃ has a direct bandgap [24, 41]. The fitting regime for determining the optical gap is chosen to be between 3.75 eV and 4.3 eV, as well as between 5.3 eV and 5.5 eV.

This is supported by the fact that the growth rate correlates with the magnitude of strain and ω -FWHM, as can be seen in Fig. 4.7a (the outlier with low growth rate but high strain will be explained below). Note that at this point, the growth rate cannot be deconvoluted from the thin film thickness. Therefore, it is not clear whether the thickness or the reduced growth rate influences the crystal quality.

The origin of the varying growth rate – and therefore varying crystal quality – can be found when taking the number of processes into account that were performed before a specific process. In Fig. 4.7b, the growth rate is visualized depending on the order of sample fabrication. It is also indicated when, the laser entrance window has been cleaned. It is common practice to clean the latter every couple of processes due to coating with target material which absorbs laser energy. E.g., in the case of ZnO, even after 100 000 pulses, no significant influence can be observed on the transmission of

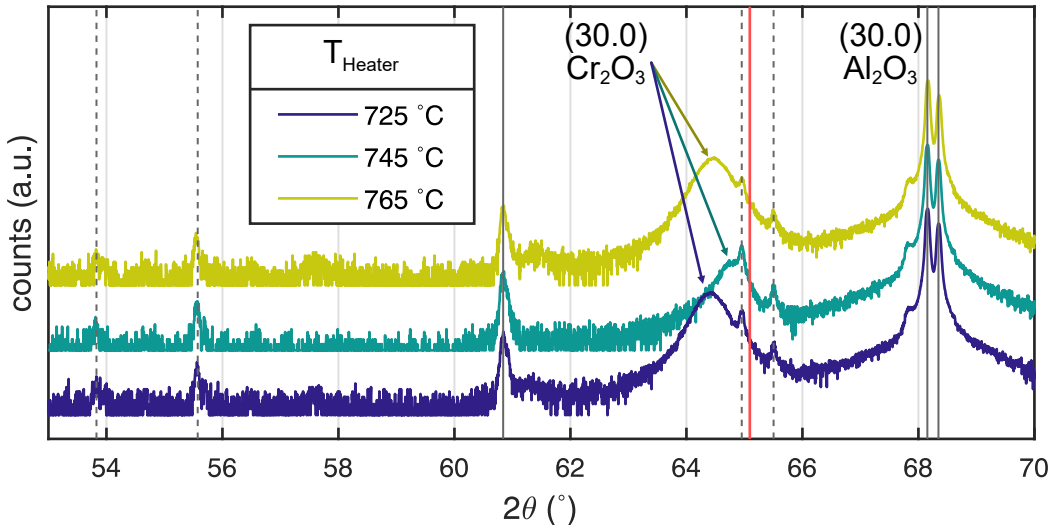


Figure 4.6: $2\theta-\omega$ -pattern of Cr_2O_3 thin films deposited on *m*-plane sapphire for three different growth temperatures. The gray solid lines indicate (30.0) substrate reflections corresponding to copper radiation, whereas the gray dashed lines indicate (30.0) substrate reflections corresponding to tungsten radiation. The red line corresponds to the predicted (30.0) reflection of Cr_2O_3 .

laser energy. But from Fig. 4.7b it becomes clear that this should be done much more frequently when working with Cr_2O_3 . Note that the laser has a wavelength of 248 nm, corresponding to 5.0 eV, which is not transmitted by Cr_2O_3 thin films⁽²⁾, as can be seen in Fig. 4.5a. Therefore, the increasing coating of the laser entrance window with each new process absorbs a large amount of laser pulse energy, resulting in less fluence on the PLD target. This results in less ablated target material and less kinetic energy of the ablated species, which leads to a reduced growth rate and different crystal growth conditions that have less strain and ω -FWHM as a result.

This explanation is supported by the dependence of crystal quality on oxygen partial pressure (cf. Fig. 4.3a). There, the increasing crystal quality with higher oxygen pressures is attributed to the increased background gas scattering resulting in less kinetic energy of the plasma material. This also explains the outlier in Fig. 4.7a, where one sample corresponds to a higher strain and ω -FWHM of approx. 0.9 % and 41', respectively (black square). This is not expected when considering the rather small growth rate of 3 pm pulse^{-1} (W6724 in Fig. 4.7b). But when taking into account that this sample is fabricated at a very low oxygen partial pressure of 8×10^{-5} mbar, it becomes clear that although the reduced fluence on the target would generally lower the kinetic energy of the plasma material, the limited scattering with the background gas counteracts this effect, resulting in the observed crystal quality.

It is noteworthy that the observed strain (cf. Fig. 4.3a,b) is distributed around two distinct values of approx. 0.4 % and 0.9 %. A prior reported thin film tilt for *m*-plane oriented rhombohedral heterostructures [78] may be the reason for this observation:

⁽²⁾ To be precise, the transmission spectrum in Fig. 4.5a is recorded for *m*-plane oriented *crystalline* Cr_2O_3 thin films. This may not be the present phase when Cr_2O_3 deposits on the (colder) window made out of glass, where it may form an amorphous phase.

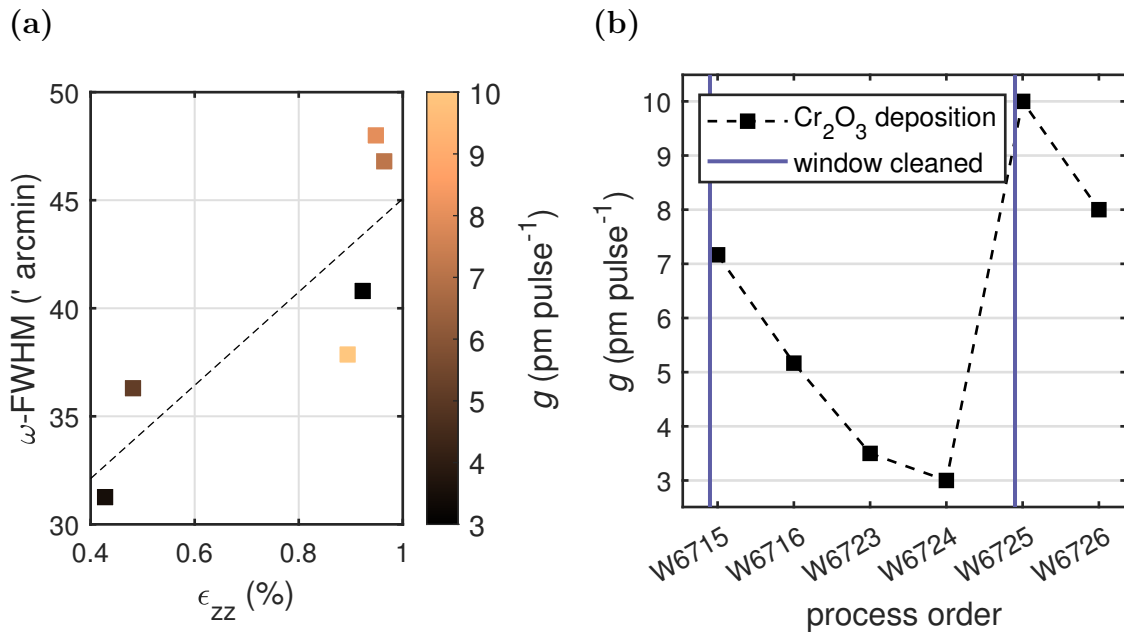


Figure 4.7: (a) Correlation of ω -FWHM with o.o.p. strain, as well as correlation of both with growth rate g (false color). The dashed line is a linear fit serving as guide to the eye. The outlier with low growth rate but large strain can be explained by accounting for the low oxygen partial pressure of 8×10^{-5} mbar for this sample. This results in larger kinetic energy of the plasma species. (b) Growth rate depending on order of sample fabrication.

the samples are installed in the XRD device in such a way that the c -axis is either parallel or orthogonal to the scattering plane. This orientation is arbitrary, and thus the (expected) thin film tilt is either along the X-ray beam or perpendicular to it, which could result in unexpected results when calculating the o.o.p. lattice plane distance from the observed peak position. To check if this is the origin of the observed strain, for two samples of different strain according to Fig. 4.3, four 2θ - ω -scans were performed with incrementing the azimuth by 90° after each measurement. The resulting diffraction patterns are depicted in Fig. 4.8. The strain is independent of azimuth, only the peak intensity is altered by the in-plane rotation of the sample as expected. For both samples, an azimuth of 0° and 180° results in a lower intensity, supporting the hypothesis that the (expected) thin film tilt is perpendicular to scattering plane which results in a deviation from the BRAGG condition. Therefore, the distribution of observed strain is not a measurement artifact.

4.1.5 Deposition on c -, r -, m - and a -plane Sapphire

For the samples deposited on substrates with different orientation, 2θ - ω -patterns were recorded (Fig. 4.9). For each sample, the expected Al₂O₃ peaks are observed: (00.6) and (00.12) for c -plane; (01.2), (02.4), (03.6) and (04.8) for r -plane; (30.0) for m -plane; (11.0) and (22.0) for a -plane. Several smaller peaks also correspond to those reflections but stem from other X-rays than Cu-K α . The mentioned reflections are also observed for the Cr₂O₃ thin film, but with a shift in 2θ position similar to the previously inves-

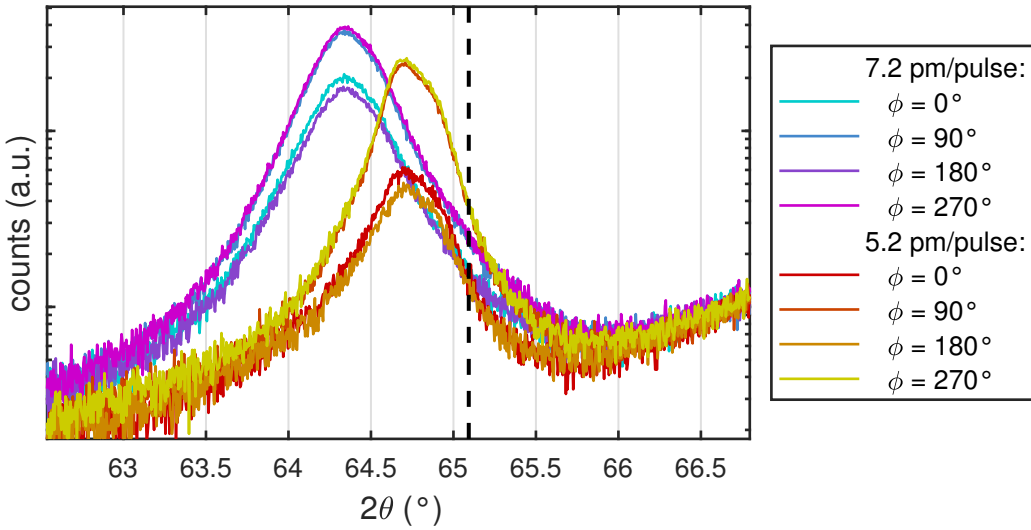


Figure 4.8: 2θ - ω -patterns for two samples in four different azimuths each. The black dashed line indicates the expected (30.0) reflection of Cr_2O_3 .

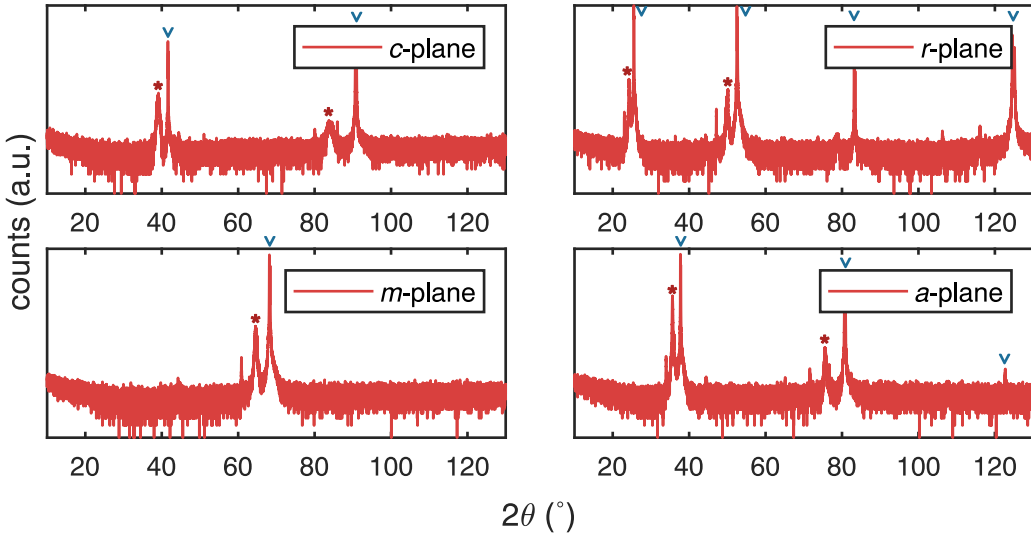


Figure 4.9: 2θ - ω -patterns of Cr_2O_3 thin films deposited on *c*-, *r*-, *m*- and *a*-plane sapphire. The red star (*) and blue wedge (V) mark reflections of Cr_2O_3 and Al_2O_3 , respectively.

tigated *m*-plane samples (Tab. 4.1). Note that for *r*-plane, the higher order reflections of Cr_2O_3 cannot be observed. It can be concluded that Cr_2O_3 grows in the α -phase on sapphire substrates of different orientation, where the thin film orientation matches the corresponding substrate. Henceforth, “*c*-plane Cr_2O_3 ” will refer to a Cr_2O_3 thin film deposited on *c*-plane oriented $5 \times 5 \text{ mm}^2$ sapphire substrates, and so on. For each sample, ω -scans were performed on the (00.6), (02.4), (30.0) and (11.0) reflections for *c*-, *r*-, *m*- and *a*-plane, respectively. The resulting ω -FWHMs are in the range of approx. 30' to 40' (Tab. 4.1). Note furthermore that for every plane, an out-of-plane tensile strain can be observed, as already seen for *m*-plane thin films. This strain reaches rather large values of 1.71% for *c*-plane Cr_2O_3 .

Because the resistivity of all samples was too high to measure Hall effect, only resistivity measurements (cf. 3.4) were performed for several temperatures (Fig. 4.10).

Table 4.1: Structural parameters, approximate resistivity at room temperature and activation energy for Cr₂O₃ thin films of different orientation.

Plane	ϵ_{zz} (%)	ω -FWHM (')	ρ ($\Omega \text{ cm}$)	E_A (meV)
<i>c</i>	1.71	42.6	3	57, 34
<i>r</i>	0.72	38.4	120	117
<i>m</i>	0.55	42.6	3600	240
<i>a</i>	1.41	32.4	4900	259

The samples were contacted on four corners with Ti-Al-Au via thermal evaporation. The resistivity depends strongly on the orientation of the thin film. The resistivities at room temperature are listed in Tab. 4.1. A difference of more than three orders of magnitude of the resistivity between *c*-plane and *a*-plane samples is observed. The linear behavior of the ARRHENIUS-plot, $\log \rho$ vs. T^{-1} , indicates a thermally activated mechanism for conductivity, and thus semiconductive behavior. Note that no further conclusions can be drawn on the conduction mechanisms due to the missing carrier concentration and mobility data. By assuming a behavior of the form

$$\rho \propto \exp\left(\frac{E_A}{k_B T}\right), \quad (4.2)$$

with BOLTZMANN constant k_B , an activation energy E_A can be estimated. Those energies are also listed in Tab. 4.1. For *c*-plane Cr₂O₃, two linear regimes can be distinguished, favoring a dependence of the form

$$\rho \propto a \exp\left(\frac{E_{A,1}}{k_B T}\right) + b \exp\left(\frac{E_{A,2}}{k_B T}\right), \quad (4.3)$$

thus two activation energies are determined. In previous studies, activation energies of 400 to 500 meV for polycrystalline Cr₂O₃ thin films prepared by CVD [45] and 200 meV for Mg-doped *c*-plane thin films prepared by electron beam PVD evaporation [24] were reported. The values were also determined by simply fitting the linear regime in an ARRHENIUS plot of the conductivity and are in accordance to the here reported values.

4.1.6 Conclusion

m-plane Cr₂O₃ thin films can be deposited over a wide range of oxygen partial pressure of more than two orders of magnitude. It turned out that the crystal quality correlates mainly with the growth rate, which is presumably caused by a variation of the laser pulse fluence on the target. Therefore, lower kinetic energy of the plasma species is probably the reason for improved crystallinity and less strain. Even though the influence of those parameters was less dominant, an oxygen partial pressure of 1×10^{-3} mbar and a growth temperature of 750 °C are identified as best growth conditions.

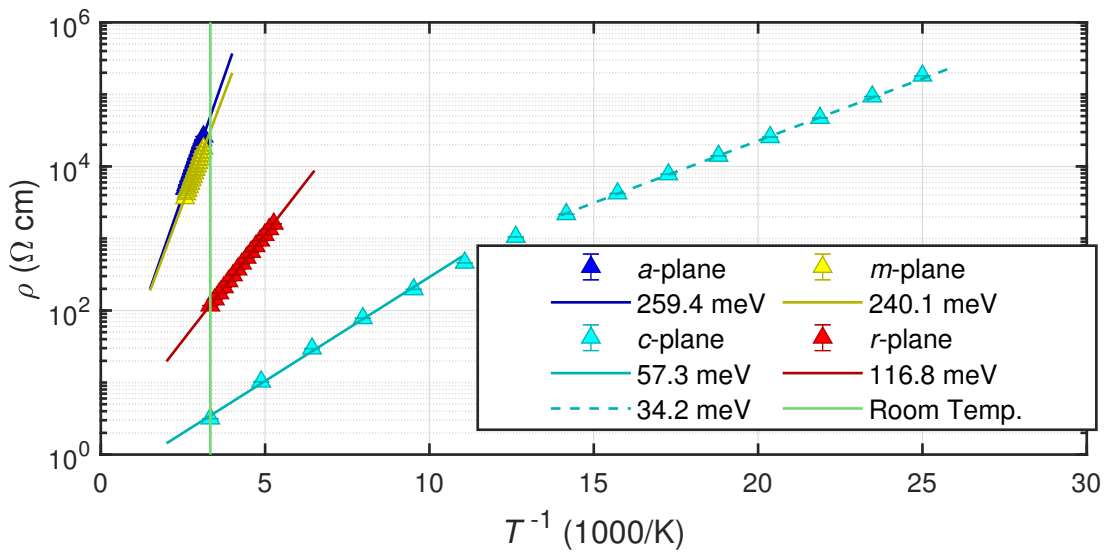


Figure 4.10: Temperature dependent resistivity measurements for samples with different orientations.

Note that those values overlap with the conditions for deposition $\alpha\text{-Ga}_2\text{O}_3$, which makes ternary solid solutions of chromia with rhombohedral Ga_2O_3 feasible.

$\alpha\text{-Cr}_2\text{O}_3$ was also deposited on *c*-, *r*- and *a*-plane sapphire, with the thin films crystallizing in the respective orientation. This is important for heterostructures with $\alpha\text{-Ga}_2\text{O}_3$ and could enable growth of rhombohedral Ga_2O_3 on all common sapphire cuts via Cr_2O_3 buffer layers. Note that all deposited thin films showed a discrepancy between observed o.o.p. lattice constants and bulk Cr_2O_3 literature values (Tab. 2.1). The conductivity is strongly dependent on the crystal orientation and was very low for the prismatic orientations, but with 0.3 S cm^{-1} three orders of magnitude higher for the basal orientation.

4.2 Discrete Combinatorial Synthesis for Tailored Doping

As described in the previous chapter, the resistivity of the Cr₂O₃ thin films shows strong dependence on thin film orientation. To improve and taylor the conductivity, it is tried to incorporate acceptors into the *p*-type material. The elements chosen for this are lower valent Cu²⁺ via CuO and Zn²⁺ via ZnO, because doping has already been reported in literature on *c*-plane sapphire with magnesium via MgO [24].

4.2.1 Experiment

As described in Section 3.1.1, Equ. (3.1) can be applied to calculate the material composition χ of the plasma plume when utilizing a DCS target. But as mentioned before, this does not account for the finite area illuminated by the laser pulse. A simple model for including this effect can be achieved by assuming a target that has an outer composition of pure Cr₂O₃ and an inner composition of Cr₂O₃ with dopant concentration $x_{D,0}$. Simulating N randomly distributed points r_i in the range Δr around a radial laser position r_{PLD} allows the calculation of doping concentration in the plasma x_D as the mean of the N calculated compositions for each r_i . The resulting dependence of x_D on r_{PLD} is visualized in Fig. 4.11a, where a higher value of Δr results in more smeared out graphs. Those *Monto Carlo* simulations can further be approximated by a linear fit, which was done for $\Delta r = 2$ mm (blue dotted line in Fig. 4.11a). Henceforth, the different samples fabricated with different radial laser spot positions r_{PLD} are parameterized by the expected composition x_D calculated from this linear fit. Note that due to the small concentration of dopant, it was not possible to resolve those fractions via element sensitive measurements: Dr. Daniel Splith kindly performed Energy-dispersive X-Ray Spectroscopy (EDX) measurements that resulted in no signal for either Cu or Zn.

To fabricate doped thin films, three different PLD targets were utilized. Each target was elliptically segmented, with the outer region consisting of pure Cr₂O₃ and the inner region consisting of Cr₂O₃ with dopant concentration $c_{D,0}$:

1. $c_{D,0} = 0.01$ wt.% CuO, called *CuO-doped*,
2. $c_{D,0} = 0.01$ wt.% ZnO, called *ZnO-doped (low)* and
3. $c_{D,0} = 1$ wt.% ZnO, called *ZnO-doped (high)*.

For each target the DCS approach was utilized, i.e. several processes were done with fixed laser spot position during deposition, but varying laser spot position *between* processes. For each process, deposition was done on all of the 4 aforementioned substrate orientations, even though *m*- and *a*-plane samples did not exhibit any substantial

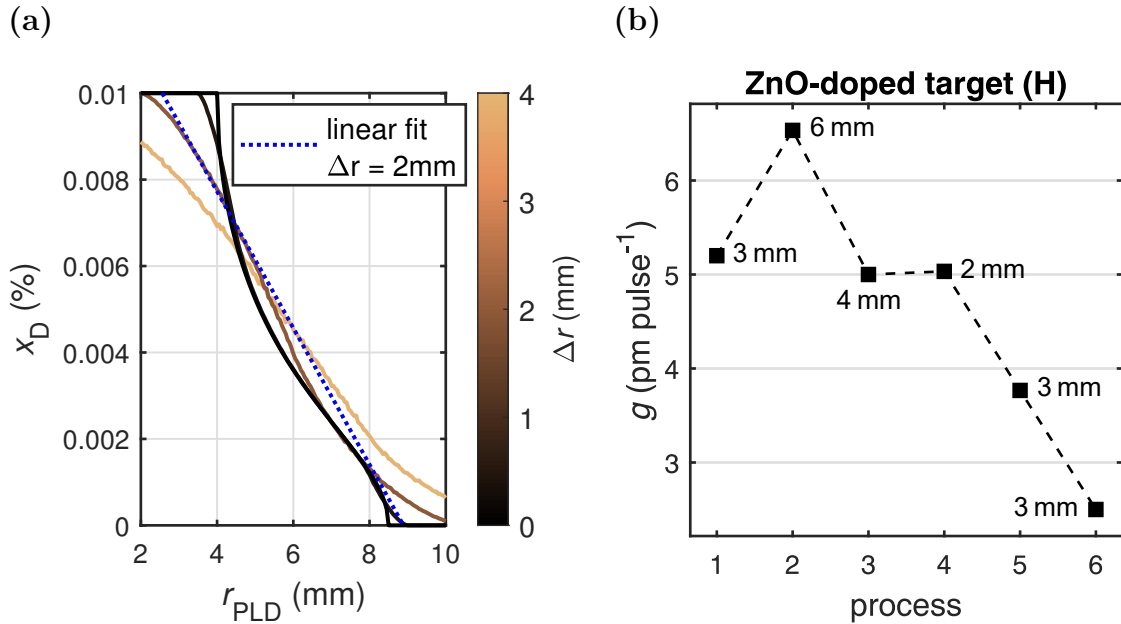


Figure 4.11: (a) Predictions for the plasma plume composition x_D using Monte Carlo simulations with $N = 10\,000$ and different values for Δr . The blue dotted line is a fit for the graph calculated with $r = 2$ mm. (b) Growth rate depending on the process order for the samples fabricated from the ZnO-doped (high) target. The laser entrance window was cleaned after each process. The applied r_{PLD} is indicated next to the marker symbols.

conductivity. This was done to check whether the conductivity of the prismatic orientations could be improved via doping. The pulse number was 40 000 for the 0.01 wt.% targets and 30 000 for the ZnO-doped (high) target.

4.2.2 DCS with Different Targets

To investigate the growth rate, spectroscopic ellipsometry measurements were performed to determine the thickness. The according growth rates of the samples produced from the CuO-doped and ZnO-doped (low) target are depicted in Fig. 4.12. The growth rates vary between 3 and 6 pm pulse $^{-1}$ and depend strongly on the number of deposition processes that were conducted before. By cleaning the laser entrance window after three processes, and thus reducing laser energy absorption, the growth rate is doubled, which is non-negligible. This is similar to the results obtained in chapter 4.1.

To circumvent the effect of the window blinding with each process, the window was cleaned after each process for the samples produced from the ZnO-doped (high) target. The growth rates depending on the fabrication order for those samples are depicted in Fig. 4.11b. However, note that the growth rate still varies from approx. 2.5 to 6.5 pm pulse $^{-1}$, even though the laser entrance window was cleaned after each process. So this variation in growth rate must be traced back to another effect. Only the first sample was fabricated with 40 000 pulses, which explains the increment of growth rate between the first and second process: The condensation of material on the laser

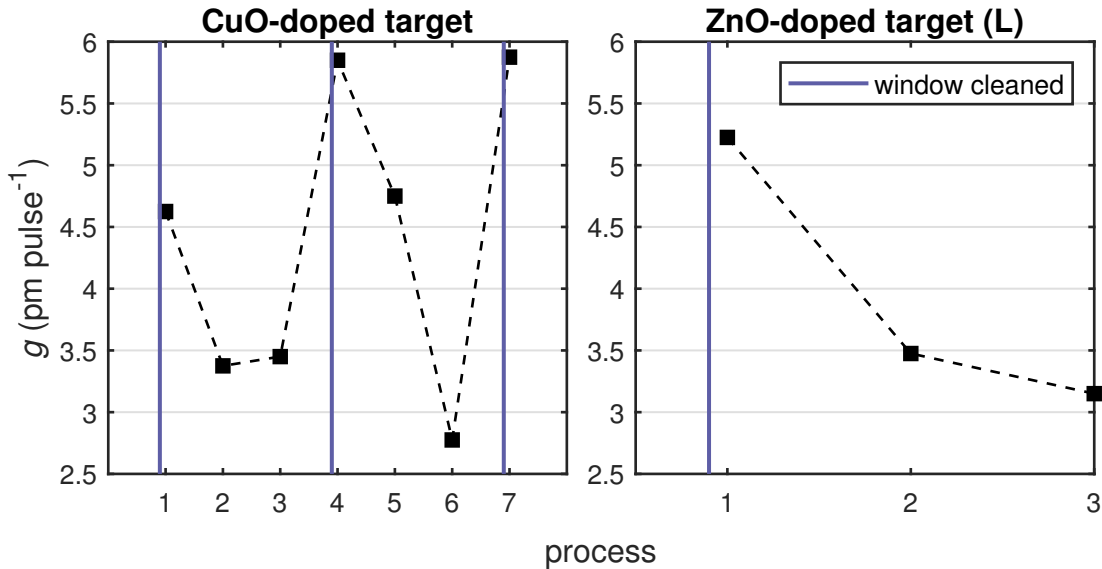


Figure 4.12: Growth rate depending on the process order for the samples fabricated from the CuO-doped and ZnO-doped (low) target. It is indicated when the laser entrance window was cleaned.

entrance window yields a decreasing growth rate over time. This has a strong effect on the overall growth rate calculated for the complete process. Furthermore, the second process was done with $r_{PLD} = 6$ mm, which is rather outside compared to the 1st, 3rd and 4th process with 3 mm, 4 mm and 2 mm, respectively. This results in a larger total ablated area and in less target degradation. Therefore, the hypothesis is that target degradation during deposition has an influence on the growth rate. To systematically investigate this, three processes were conducted at the same radius, namely process 1, 5 and 6. Note that all these samples were fabricated with $r_{PLD} = 3$ mm and otherwise the same deposition parameters. The only variation is that tracks are carved into the target by the laser (Fig. 4.13c). This is probably the reason for a crucial change in plasma dynamics and therefore a reduction of the growth rate from approx. 5 to 2.5 pm pulse $^{-1}$.

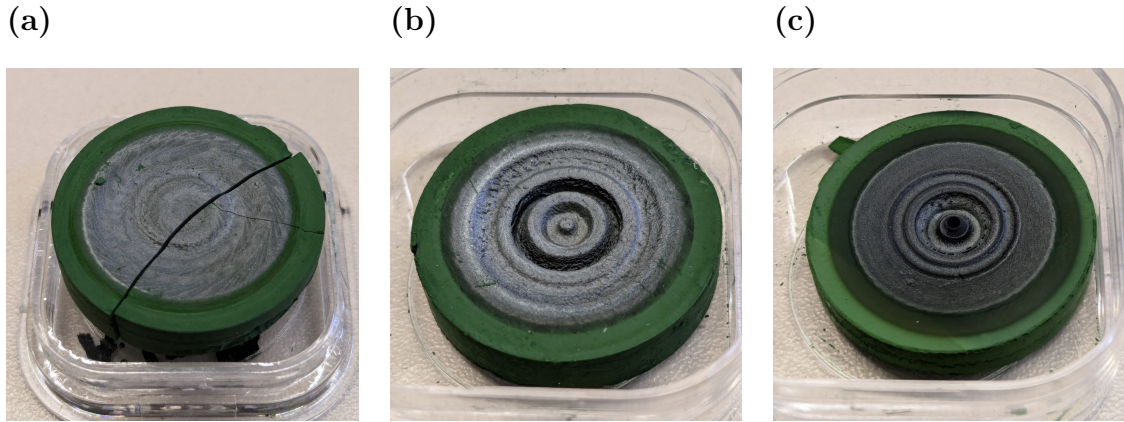


Figure 4.13: Photograph of the (a) CuO-doped, (b) ZnO-doped (low) and (c) ZnO-doped (high) target. The CuO-doped target broke during the last process it was used in. The silverish tint is presumably due to the formation of metallic chromium oxide CrO_2 on the target surface.

To probe the conductivity of the fabricated samples, resistivity measurements were performed using the PAUW methods. Only r - and c -plane samples were investigated, because the prismatic planes exhibited resistances of several $\text{G}\Omega$ or higher, when measured with a multimeter, as the HALL-effect measurement setup at the semiconductors group is not designed to measure such high resistivities. In Fig. 4.14a, the measured resistivity ρ at room temperature depending on the predicted dopant concentration x_D is depicted. From the unsystematic variation in resistivity (2 to $500 \Omega \text{ cm}$), it can be concluded that the attempt of doping the Cr_2O_3 thin films resulted in no improvement of conductivity. Using the two targets with different concentration of ZnO in the inner ellipse, no change was observed when adjusting x_D between 0.001 % and 1 %. In particular, note the aforementioned samples (1, 5 and 6 in Fig. 4.11b) that were fabricated with the same growth condition $r_{\text{PLD}} = 3 \text{ mm}$, corresponding to the triangles in Fig. 4.14a at approx. $x_D = 1 \%$: here, the same process parameters yield samples differing in resistivity by 2 orders of magnitude. Because those samples showed different growth rates due to target degradation, it is plausible that these altered growth dynamics also influence the conductivity.

Because in the previous chapter 4.1 it was shown that the growth rate is correlating to the ω -FWHM, Rocking scans were performed on the (00.6) and (02.4) reflection for c -plane and r -plane samples, respectively. The extracted ω -FWHMs are depicted in Fig. 4.15 depending on the growth rate for the respective process. A general trend is that the crystallinity increases for lower growth rates, namely for a growth rate of $3.4 \text{ pm pulse}^{-1}$, a ω -FWHM of 4' (240") can be achieved. It is irrelevant, whether this reduction in growth rate is due to lower fluence on the laser target due to infrequent window cleaning (CuO-doped and ZnO-doped (low) target) or due to target degradation (ZnO-doped (high) target). The better FWHM is achieved for c -plane samples. Note that for the deposition of Cr_2O_3 on r -plane sapphire from the ZnO-doped (high) target, no thin film peaks in 2θ - ω -scans were observed (Fig. B.1). Those X-ray-amorphous

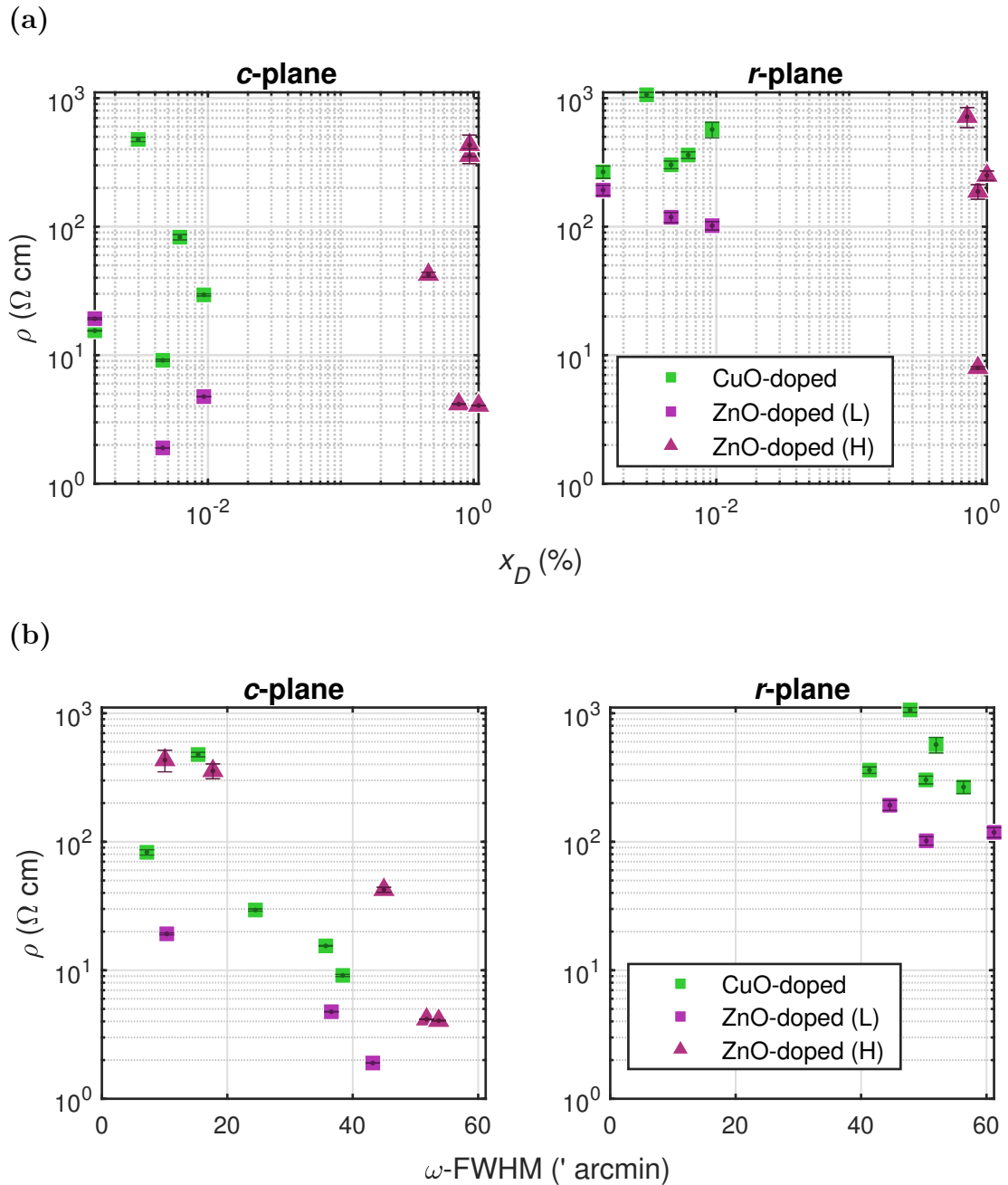


Figure 4.14: (a) Resistivity vs. predicted dopant concentration for *c*- and *r*-plane samples fabricated from all three radially segmented targets. (b) Resistivity vs. ω -FWHM of the aforementioned samples. Note that the *r*-plane samples fabricated from the ZnO-doped (high) target did not exhibit sufficient peak intensity to determine the ω -FWHM.

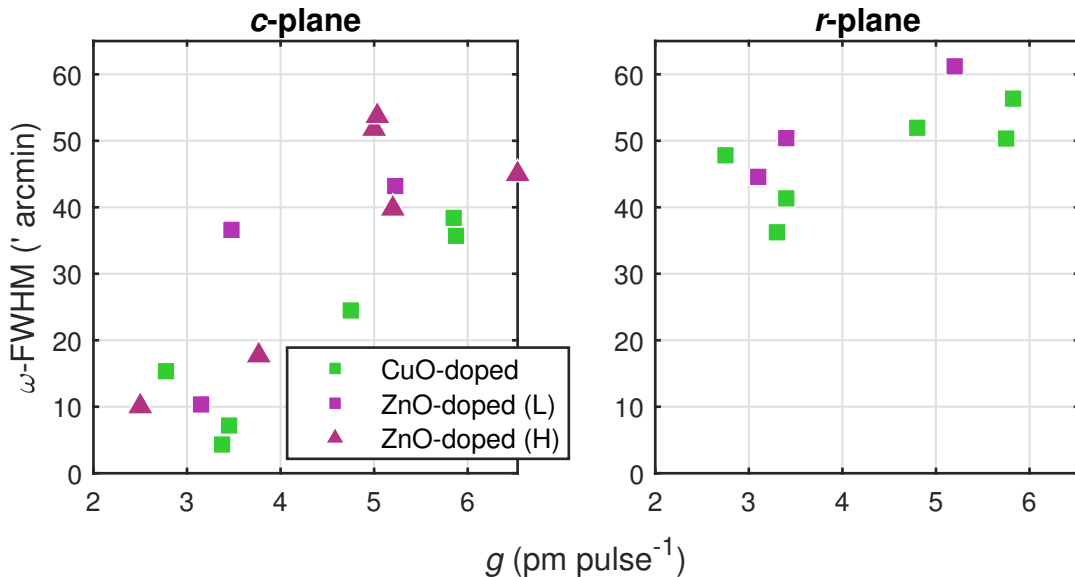


Figure 4.15: ω -FWHM for *c*- and *r*-plane samples that were fabricated from the three radially segmented targets.

films are presumably a result of the drastically altered plasma dynamics due to target degradation.

To investigate the influence of crystal quality on the electrical properties, in Fig. 4.14b, the resistivity depending on the ω -FWHM is depicted. It becomes clear that a higher mosaicity results in higher conductivity. Since more dislocations correspond to more crystal defects (cf. section 2.3.2), this result is in accordance to the predicted influence of crystal defects on the electrical properties of Cr_2O_3 thin films (cf. section 2.1.1). It has to be noted that this effect is less pronounced for *r*-plane samples compared to *c*-plane samples, where resistivities as low as $1.9 \Omega \text{ cm}$ can be achieved for an ω -FWHM of $40'$. Furthermore, this does not explain why *m*- and *a*-plane Cr_2O_3 exhibit such high resistivity, because their ω -FWHM is comparable to the basal and pyramidal orientations (cf. Tab. 4.1).

For each target, one *c*-plane sample with presumably highest doping concentration (smallest *r*_{PLD}) was chosen to perform temperature dependent resistivity measurements in the range of 40 to 390 K (Fig. 4.16). For all samples, an ARRHENIUS-like behavior is observed with two linear regimes above and below 100 K, respectively. By applying Equ. (4.3), two activation energies can be extracted that are listed in Tab. 4.2. Note that there is no significant difference between the undoped and doped samples. Furthermore, the samples with the smallest ablation radius for each target were chosen, and not the samples with the highest conductivity for each batch. Therefore, the data in Fig. 4.16 does not indicate that samples from the Cu-doped target have lower conductivity per se.

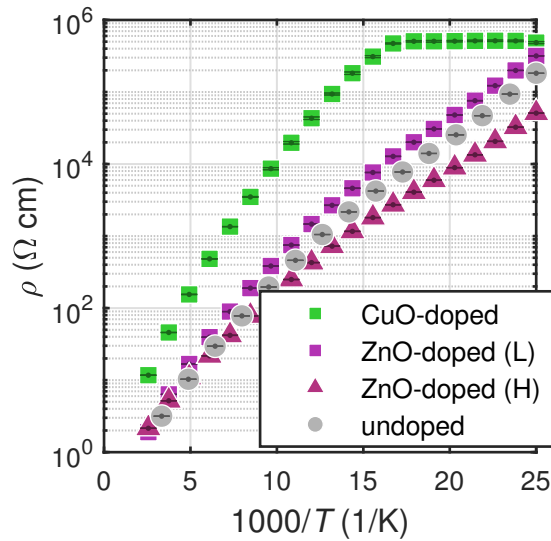


Figure 4.16: Temperature dependent resistivity measurements for c -plane samples fabricated from the different radially segmented targets, as well as a pure Cr_2O_3 target. The clipping of the sample from the CuO-doped target (green squares) is due to the limited resolution of the measurement device and the artifact nature of this saturation is confirmed by repeated measurements with different current applied during measurement (not shown).

Table 4.2: Activation energies E_A extracted from the linear regimes in the temperature dependent resistivity measurements (Fig. 4.16).

target	E_A (meV)	
	< 100 K	> 100 K
CuO-doped	53	83
ZnO-doped (low)	35	61
ZnO-doped (high)	31	50
pure Cr_2O_3	35	54

Even though the doping resulted in no improvement of the electrical properties of the thin films, the several samples fabricated at different growth conditions – due to infrequent laser window cleaning and target degradation – may serve as an insight into the o.o.p. strain that was already observed in chapter 4.1. The o.o.p. strain dependent on the growth rate is depicted in Fig. 4.17a and was determined from Cr_2O_3 peak positions in $2\theta\text{-}\omega$ patterns. For *m*- and *a*-plane, the hypothesis of increasing strain with increasing growth rate can be confirmed. However, the slope of this relation differs depending on the target: the samples fabricated from the CuO-doped target showed less strain depending on growth rate than the samples fabricated from the ZnO-doped (high) target. This may be explained by the fact that the target degradation for the former (cf. Fig. 4.13a) was not so pronounced when compared to the latter (cf. Fig. 4.13c).

A reverse behavior is observed for *c*-plane samples: the strain is increasing with higher growth rates. But compared to *m*- and *a*-plane, there is no significant difference between the samples fabricated from different targets. This leads to the assumption that the plasma dynamics do not determine the o.o.p. strain for this orientation. It has to be noted that due to the constant pulse number, a change in growth rate corresponds to a change in thickness of the thin films. Therefore, it may be possible that the strain of the thin samples (low growth rate) is due to pseudomorphic growth on the corresponding Al_2O_3 substrate. Note that this leads not to the conclusion that the origin of the strain in *m*- and *a*-plane samples is also pseudomorphic growth: There, the thicker samples show more strain which is not expected because far away from the interface, dislocations should form to propagate relaxed growth. For *r*-plane samples, the overall strain is smaller and shows a less pronounced trend similar to *m*- and *a*-orientation. Because *r*-plane has both basal and prismatic character, both thickness and plasma dynamics effects may contribute to the observed strain.

The qualitative difference between *c*-plane and the other orientations can also be observed in Fig. 4.17b, where the ω -FWHM is shown depending on the o.o.p. strain. Compared to the previous results (cf. Fig. 4.7a), both factors characterizing crystal quality (strain and ω -FWHM) are not minimized simultaneously.

4.2.3 Conclusion

The incorporation of CuO or ZnO had no effect on the conductivity of *c*- and *r*-plane oriented Cr_2O_3 thin films. None of the *m*- or *a*-plane oriented films became conductive. However, the conductivity depends strongly on the crystallinity, which indicates intrinsic defects as the origin of charge carriers. The crystallinity is mainly influenced by target degradation due to repeated ablation with the same laser spot position on the target. This results in lower growth rates and presumably less kinetic energy of the plasma species which deposits on the substrate. Even though the doping attempt showed no effect, a discrete material library of Cr_2O_3 thin films with different

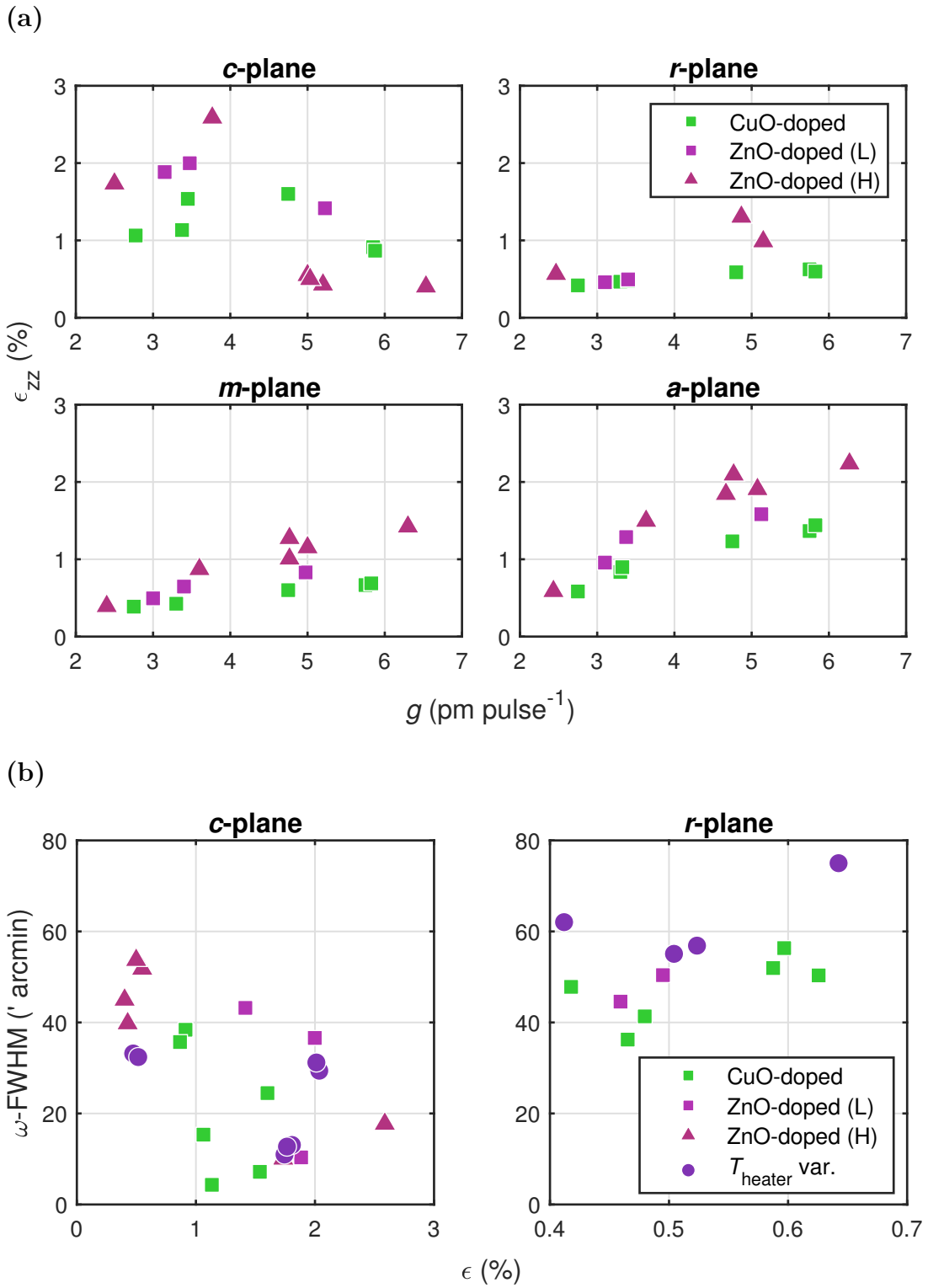


Figure 4.17: (a) Strain extracted from the peak positions in 2θ - ω -scans for samples fabricated from the three radially segmented targets. (b) Correlation between strain and ω -FWHM for *c*- and *r*-plane samples. The samples fabricated at different growth temperatures are also included.

strains was provided. A fundamental difference between *c*-plane and the other common orientations was observed, regarding the origin of the observed o.o.p. strain. Further measurements must be conducted to deconvolute the effects of (i) thickness, (ii) laser fluence on target and (iii) target degradation.

4.3 Strain Analysis

The structural properties of the thin film, namely its mosaicity and lattice distortion depend crucially on the growth process: It was observed that the absorption of energy at the laser entrance window alters the growth rate and the crystallinity much more dominantly than the growth temperature or the oxygen partial pressure (cf. chapter 4.1). A similar effect was observed when worn targets were used for fabrication: a non-planar surface caused by tracks that were carved by the laser during previous ablations alter both structural and electrical properties of the resulting thin films substantially (cf. chapter 4.2). Therefore, the following investigations focus on the origin of the observed variations in strain and ω -FWHM. This is further motivated by the observation that a deliberate and controlled variation of laser spot size on the target surface yields a large reduction of ω -FWHM as well as a reduced shift of the peak position in the 2θ - ω -pattern (Fig. 4.18). This was achieved by varying the lens position L such that the laser spot size increases, yielding smaller fluence F and larger ablation area A on the target surface. Namely, doubling the laser spot size from 8 to 16 mm² results in an improvement of crystallinity by a factor of over 5.

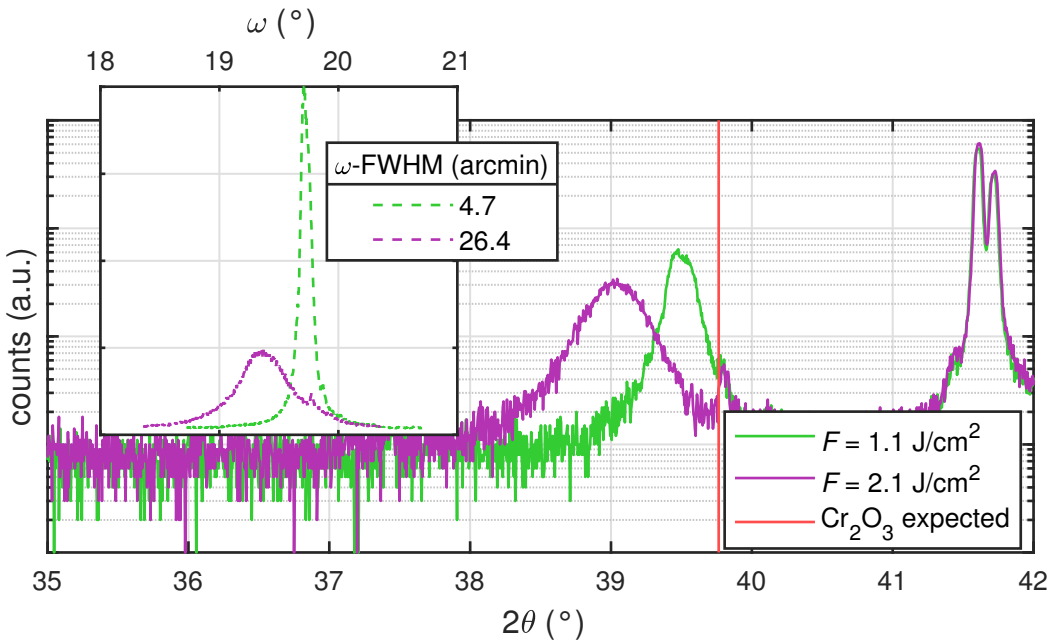


Figure 4.18: 2θ - ω -patterns for two c -plane samples fabricated with different laser spot size, therefore different laser fluence on the target. The thickness is 120 nm and 100 nm for the low fluence (green) and high fluence (purple) sample, respectively. The red line at 39.8° corresponds to the calculated peak position of the Cr_2O_3 (00.6) reflection. The low intensity peak at this angle is the Al_2O_3 (00.6) reflection caused by tungsten La_1 radiation. The peak at approx. 41.5° corresponds to the Al_2O_3 (00.6) reflection caused by copper K α radiation. The inset displays the diffractograms of the corresponding ω -scans performed on the Cr_2O_3 (00.6) reflection. The ZnO -doped (low) target (cf. chapter 4.2) was used for deposition without a fixed r_{PLD} but with uniform ablation on the whole target surface. The reason for the choice of target is that this experiment was conducted in the course of the studies of the previous chapter, where a DCS approach was applied for thin film doping. A pulse energy of 650 mJ was applied.

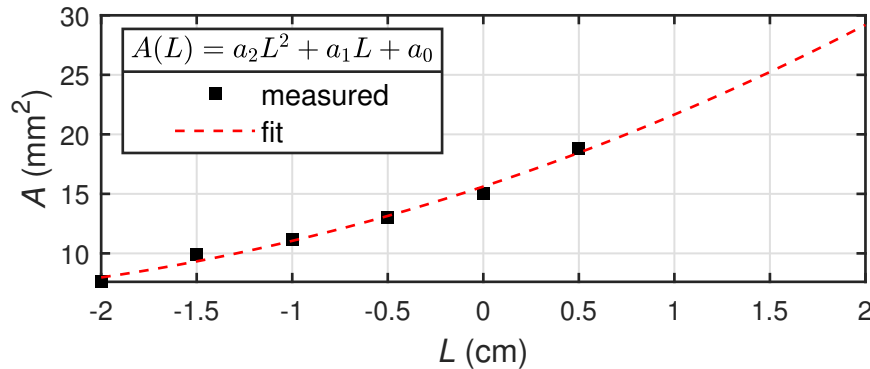


Figure 4.19: Laser spot size A depending on the lens position L : measured data (black) and fit according to $A(L) = a_2 L^2 + a_1 L + a_0$ (red dashed). The fit parameters a_2 , a_1 and a_0 are $0.74 \text{ mm}^2 \text{ cm}^{-2}$, $5.3 \text{ mm}^2 \text{ cm}^{-1}$ and 15.6 mm^2 , respectively.

4.3.1 Experiment

Sample Fabrication

For all following depositions, the laser entrance window was cleaned before each process. A pure Cr_2O_3 target was used for deposition of thin films on $5 \times 5 \text{ mm}^2$ sapphire substrates in the four aforementioned orientations. A first series of samples was produced by only varying the pulse number to achieve a series of thin films with varying thickness but constant laser fluence during deposition. Therefore, the influence of thickness and growth rate can be deconvoluted. The pulse energy was set to 650 mJ and the lens position to -2 cm , resulting in a laser spot size of 8 mm^2 . As described in section 3.1.1, the laser pulse energy inside the PLD chamber is significantly lower than 650 mJ , due to absorption at the mirror, UV lens and laser entrance window. By accounting for this attenuation, the resulting fluence on the PLD target is approx. 2 J cm^{-2} . This corresponds to the standard configuration during all previous processes (pink square in Fig. 4.20). This was repeated for three other lens positions, namely 0 cm , 1 cm and 2 cm , resulting in lower fluences of 1.1 J cm^{-2} , 0.8 J cm^{-2} and 0.6 J cm^{-2} , respectively. In Fig. 4.20, the yellow circles represent the probed laser fluences. This set of samples is referred to as the 1st batch and is listed in Tab. 4.3. The laser spot sizes for different lens positions are depicted in Fig. 4.19.

To investigate the influence of fluence independent of ablation area, a 2nd batch of samples was fabricated with a laser spot size of approx. 10 mm^2 ($L = -1 \text{ cm}$) but varying laser pulse energy: 300 mJ , 450 mJ , 650 mJ and 800 mJ . The achieved fluences are 0.7 J cm^{-2} , 1.0 J cm^{-2} , 1.5 J cm^{-2} and 1.8 J cm^{-2} (red triangles in Fig. 4.20). The pulse number was adjusted to achieve approximately the same thickness for all samples even though the growth rate vastly differs. But note that for the different samples, the thickness is distributed from 100 to 200 nm . Better results could be achieved in future experiments by first calibrating the growth rates for different fluences, and then adjusting the pulse numbers accordingly. The process parameters of those samples are listed in Tab. 4.3.

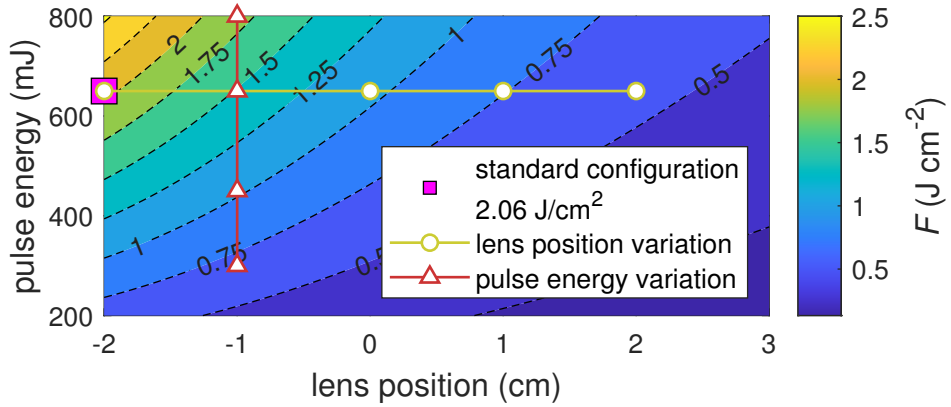


Figure 4.20: Laser energy density depending on the applied pulse energy and lens position. Smaller lens positions yield smaller spot sizes. A value of -2 cm corresponds to the lens being as close as possible to the laser entrance window in the setup used for this work. The default configuration of 650 mJ and -2 cm yields typical fluences of about 2 J cm^{-2} . The triangles and circles represent the variation of laser fluence in this work, achieved by varying the pulse energy and lens position, respectively.

Table 4.3: Processes of the first and second batch. For the first batch, a constant laser pulse energy of 650 mJ was applied. The second batch was obtained by fixing the laser spot size to 10 mm^2 . For every process, Cr_2O_3 was deposited on four sapphire substrates with different orientations of *c*-, *r*-, *m*- and *a*-plane.

	L (cm)	E_L (mJ)	A (mm^2)	F (J cm^{-2})	pulses (1k)	t (nm)
Batch 1	-2	650	8	2.1	5	25
					10	45
					20	80
					40	170
					70	210
	0		16	1.1	8	40
					20	90
					35	40
	1		22	0.8	20	50
					40	65
Batch 2	-1	300	10	0.7	40	90
					70	150
		450		1.0	40	150
		450		1.0	50	150
		650		1.5	40	200
	800			1.8	35	170

Measurements

For all samples, $2\theta\text{-}\omega$ -scans as well as ω -scans were performed. The symmetric reflections probed by the latter were (00.6), (02.4), (30.0) and (22.0) for c -, r -, m - and a -plane, respectively. For r - and a -plane samples, the higher order reflection was chosen because the distance between the Cr_2O_3 peak and the Al_2O_3 peak caused by W-L α_1 radiation increases with higher angles. Because both peaks are located at similar angles, this approach reduces the contribution of the substrate to the thin film Rocking curves. To obtain more information about the relation between in-plane and out-of-plane lattice constants, RSMs were performed on selected samples. For every orientation, lattice planes have been chosen that have both a rather small tilt and high intensity:

c -plane For c -plane samples, the thickness series grown at $L = -2\text{ cm}$ and therefore a laser spot size of 8 mm^2 ($F = 2.1\text{ J cm}^{-2}$) of the 1st batch was investigated. The asymmetric reflection that was used for probing the relaxation process is (02.10), which has an inclination angle of approx. 32° with respect to the sample surface.

r -plane All r -plane samples fabricated in the 2nd batch with different laser pulse energies were investigated with RSMs. For each sample, the x -axis of the sample – containing the projection of the c -axis – is found by performing a ϕ -scan on the (03.0) reflection: This set of lattice planes has an inclination with respect to the surface, so the position of the peak in the diffraction pattern of the ϕ -scan reveals the x -axis. In this azimuth, an RSM is recorded around the asymmetric (03.0) reflection and the symmetric (02.4) reflection. By rotating $\Delta\phi = 90^\circ$, the y -axis lays in the scattering plane and another RSM is performed around the symmetric (02.4) reflection. The twofold measurement of the symmetric reflection is necessary to calculate a possible lattice plane tilt for both x - and y -direction. After performing the various corrections described in 3.2.4, the tilt angles can be calculated for both azimuths by

$$\theta = \arccos \left(\frac{q_\perp}{|\mathbf{q}|} \right) \cdot \text{sgn}(q_\parallel), \quad (4.4)$$

with q_\perp and q_\parallel being the o.o.p. and i.p. components of the scattering vector \mathbf{q} , respectively. The i.p. and o.o.p. strains are determined by comparing the observed (03.0) scattering vector to the scattering vector calculated from Cr_2O_3 bulk lattice constants:

$$\mathbf{q}_{(03.0)} = |\mathbf{q}_{(03.0)}| \cdot \begin{pmatrix} \cos \alpha_{(03.0)|r} \\ \sin \alpha_{(03.0)|r} \end{pmatrix}, \quad (4.5)$$

with $|\mathbf{q}_{(03.0)}|$ calculated from Equ. (3.6) and Equ. (3.7). $\alpha_{(03.0)|r}$ denotes the angle between the (03.0) reflection and the normal of the r -planes; it can be calculated from

Equ. (3.8):

$$\alpha_{(03.0)|r} = 90^\circ - (\alpha_{(03.0)|c} - \alpha_{(01.2)|c}) = \alpha_{(01.2)|c} = 57.62^\circ. \quad (4.6)$$

***m*-plane** Similar to the *r*-plane samples, all *m*-plane samples from the 2nd batch were investigated. The samples were aligned to the *x*-axis by performing a ϕ -scan on the asymmetric (30.6) reflection, and an RSM was recorded afterwards. By rotating $\Delta\phi = 180^\circ$ while maintaining 2θ and ω , the scattering condition for (30. $\bar{6}$) is probed and an RSM was recorded. The symmetric reflection (30.0) was also measured in this azimuth. The tilt angle and shear angle can be calculated according to Equ. (4.4) and Equ. (3.13), respectively. As described in further detail in appendix A.1, the lattice constants can be calculated from the components of the scattering vectors:

$$a_\perp = \frac{\sqrt{12}}{q_\perp^{(30.\pm 6)}}, \quad (4.7)$$

$$a_\perp = \frac{\sqrt{12}}{q_\perp^{(03.0)}}, \quad (4.8)$$

$$c = \frac{6}{q_\parallel^{(30.\pm 6)}}. \quad (4.9)$$

a_\perp denotes the *a* lattice constant in direction of the normal to the sample surface. By rotating $\Delta\phi = 90^\circ$, the *y*-axis can be probed via asymmetric reflections ($\bar{4}2.0$) and (22.0), which differ in the azimuth by $\Delta\phi = 180^\circ$. A second symmetric reflection (30.0) is recorded in this azimuth. Similar to the *x*-axis, the tilt and shear angles, as well as the lattice constants can be calculated:

$$(4\bar{2}.0) : a_\perp = \frac{\sqrt{12}}{q_\perp^{(4\bar{2}.0)}} , \quad a_\parallel = \frac{2}{q_\parallel^{(4\bar{2}.0)}}, \quad (4.10)$$

$$(22.0) : a_\perp = \frac{\sqrt{12}}{q_\perp^{(22.0)}} , \quad a_\parallel = \frac{2}{q_\parallel^{(22.0)}}, \quad (4.11)$$

$$(30.0) : a_\perp = \frac{\sqrt{12}}{q_\perp^{(03.0)}}. \quad (4.12)$$

a_\parallel denotes the *a* lattice constant parallel to the *y*-axis. For detailed calculations of the former equations, see A.1. Note that all 6 measured reflections yield a value for a_\perp , and 2 measured reflections each yield 2 values for c and a_\parallel , respectively. Therefore, for each lattice constant, the mean value is evaluated and the error is estimated by the standard deviation (cf. Fig. 4.32a).

***a*-plane** All *a*-plane samples from the 2nd batch were investigated and the method is similar to the one applied to the *m*-plane samples. The azimuth of the *x*-axis is found by performing a ϕ -scan on the (22.6) reflection, which also served for an RSM. Rotating by $\Delta\phi = 180^\circ$ yields the (22. $\bar{6}$) reflection and (22.0) is also measured. Similar

to above, the sample is rotated by 90° to align to the y -axis and two more asymmetric reflections are recorded: (30.0) and (03.0). A second RSM of (22.0) is also performed. This yields the following lattice constants for the x -axis:

$$a_{\perp} = \frac{4}{q_{\perp}^{(22.\pm 6)}} , \quad (4.13)$$

$$a_{\perp} = \frac{4}{q_{\perp}^{(22.0)}} , \quad (4.14)$$

$$c = \frac{6}{q_{\parallel}^{(22.\pm 6)}} , \quad (4.15)$$

and for the y -axis:

$$(30.0) : \quad a_{\perp} = \frac{3}{q_{\perp}^{(30.0)}} , \quad a_{\parallel} = \frac{3}{\sqrt{3}q_{\parallel}^{(30.0)}} , \quad (4.16)$$

$$(03.0) : \quad a_{\perp} = \frac{3}{q_{\perp}^{(03.0)}} , \quad a_{\parallel} = \frac{3}{\sqrt{3}q_{\parallel}^{(03.0)}} , \quad (4.17)$$

$$(22.0) : \quad a_{\perp} = \frac{4}{q_{\perp}^{(22.0)}} . \quad (4.18)$$

For detailed calculations, see A.2. Again, for the lattice constants obtained from several reflections, the mean and standard deviation are calculated (cf. Fig. 4.32b).

4.3.2 Growth Rates

In Fig. 4.21, a detailed view into the growth rates of the samples of the 1st batch is given. First of all, for a fixed fluence (false color), increasing the pulse number decreases the growth rate. This is expected, because the coating of the laser entrance window increases during the process. By fixing a pulse number to 20 000 pulses, an increase in growth rate is observed for a regime of decreasing fluence from 2 to 1 J cm⁻² (Fig 4.21 bottom). This can be explained by the fact that the reduction of fluence is due to increasing laser spot size. When the fluence is still above the ablation threshold for the target material, an increasing ablation area results in an increasing growth rate. But at some point, the fluence is too low to ablate the material and then the growth rate decreases, even though the ablation area increases. This can be observed at around 1.2 J cm⁻² in Fig. 4.21, which is therefore an estimate for the ablation threshold. For the growth rates of the samples of the 2nd batch (Fig. 4.22), a similar conclusion can be drawn. Reducing the fluence via decreasing laser pulse energy below approx. 1.5 J cm⁻² results in a decrease of growthrate from 5 to 2 pm pulse⁻¹. The ablation threshold can be localized between 1 J cm⁻² and 1.5 J cm⁻², which is in accordance to the value obtained for the 1st batch.

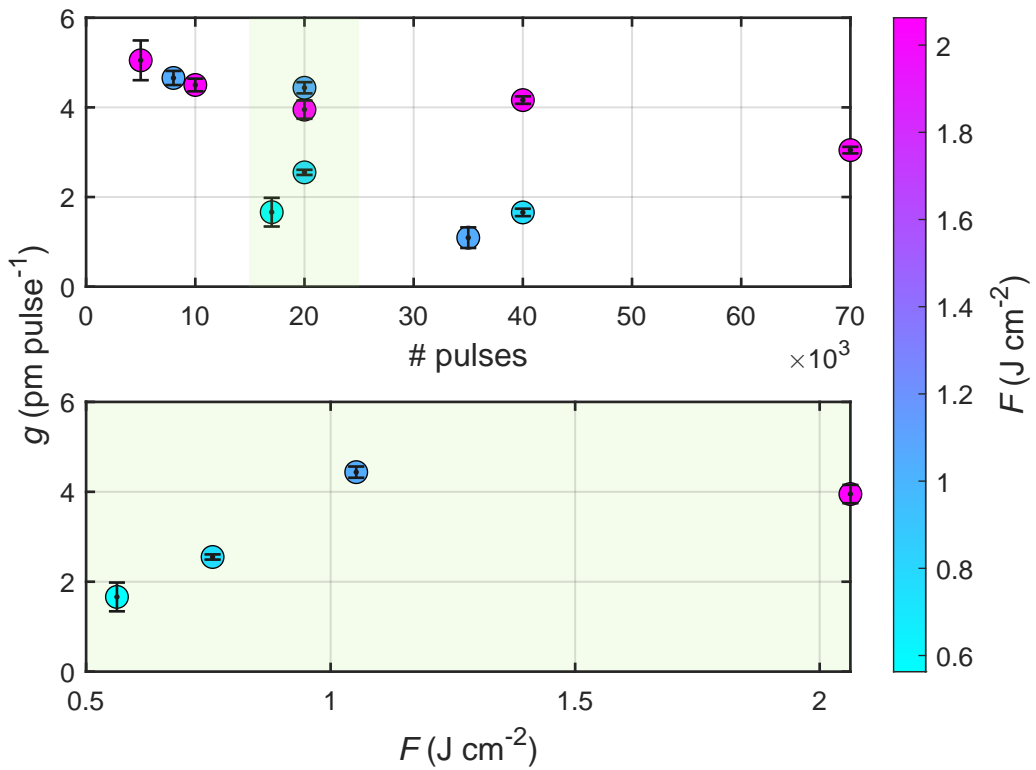


Figure 4.21: Growth rates of the samples from the 1st batch, i.e. samples with different laser spot size and therefore different laser fluence (false color), as well as different pulse number each (cf. Tab. 4.3). The growth rate is visualized as depending on the pulse number (top) and depending on the laser fluence on the target for a fixed pulse number of 20 000 (bottom). The data points are the mean of the four samples with c -, r -, m - and a -orientation, that were obtained from every process. The errorbar displays the standard deviation. s

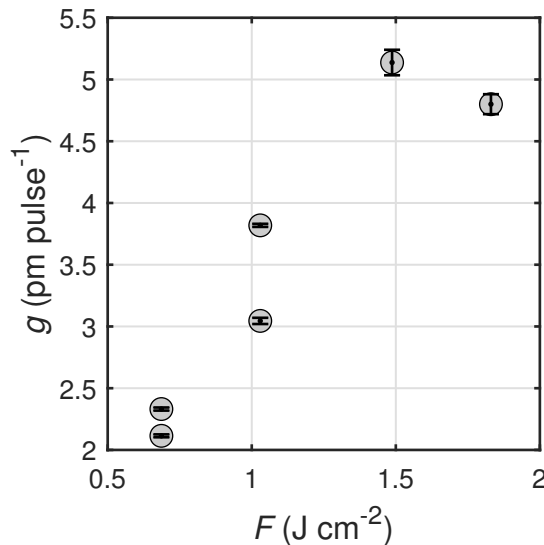


Figure 4.22: Growth rates of samples from the 2nd batch, i.e. samples with different laser pulse energy, but same laser spot size on the target, depending on laser fluence on the target surface. The data points are the mean of thicknesses of the four orientations, similar to Fig. 4.21.

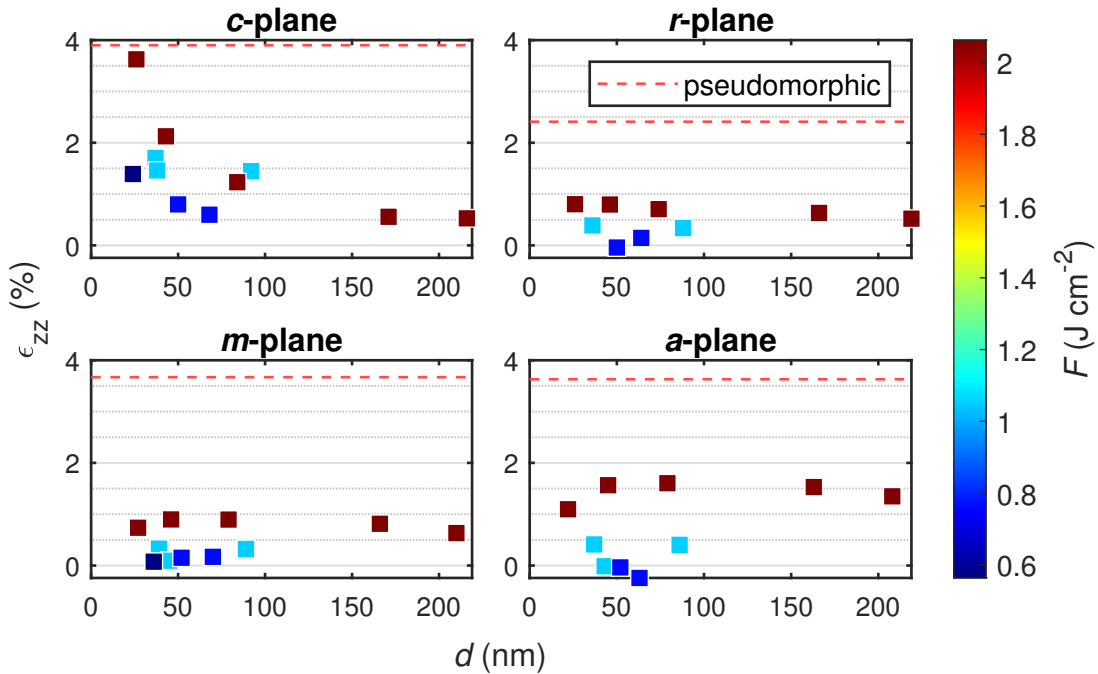


Figure 4.23: Out-of-plane strain calculated from 2θ - ω -patterns for all samples from the 1st batch, depending on thickness and laser fluence (false color).

4.3.3 Strain and Tilt for Different Orientations

c-plane: Laser Spot Size Variation

The o.o.p. strain calculated via Equ. (4.1) for all samples of the 1st batch is displayed in Fig. 4.23. Consider the *c*-plane oriented samples of the 1st batch that had a fixed lens position yielding a fluence of approx. 2 J cm^{-2} , but varying thickness (brown squares in Fig. 4.23). A clear dependence of the o.o.p. strain can be observed: thinner samples yield higher strain. The layers become relaxed for thicknesses above approx. 170 nm. For low thicknesses, the strain approaches the predicted value for pseudomorphic growth of Cr_2O_3 on Al_2O_3 , which is 3.90 % (cf. Tab. 2.4). The recorded RSMs of the $(02.\underline{1}0)$ reflection can confirm that this observation of o.o.p. strain is due to pseudomorphic growth. In Fig. 4.24, one can observe a shift of $q_{\parallel}^{(02.10)}$ to higher values for lower thicknesses. This corresponds to a decrease of the i.p. lattice constant, which is the expected behavior for pseudomorphic growth, because the i.p. *a* lattice constant of *c*-oriented Al_2O_3 is 0.2 Å smaller than for Cr_2O_3 (cf. Tab. 2.1). The tensile o.o.p. strain observed via 2θ - ω -scans can also be confirmed by the fact that the o.o.p. component $q_{\perp}^{(02.10)}$ is decreasing for thinner samples. The reduction of signal intensity is attributed to the thickness, but could also be a result of decreasing crystal quality (cf. Fig. 4.25). Makushko *et al.* [94] reported a similar behavior for *c*-plane Cr_2O_3 thin films deposited via magnetron sputtering. They varied the thin film thickness from 30 to 250 nm, which is comparable to this work. In TEM measurements, they could observe that dislocations started forming approx. 5 nm away from the Cr_2O_3 – Al_2O_3 interface, indicating a highly strained pseudomorphic layer. This could also be ob-

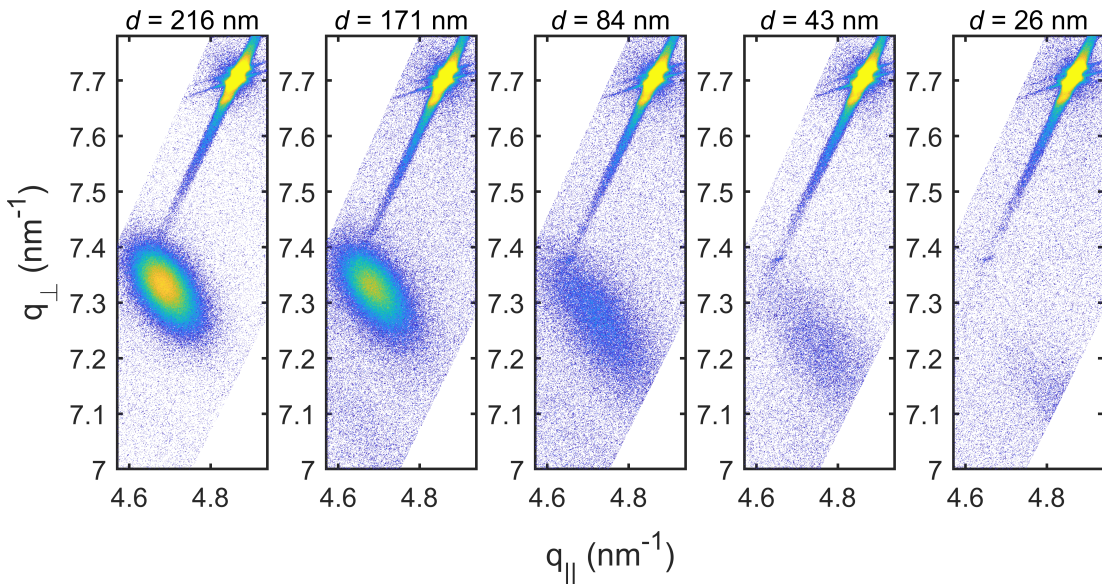


Figure 4.24: RSMs of the (02.10) reflection for *c*-plane oriented samples with varying thickness. The laser spot size was 8 mm^2 , resulting in a fluence of approx. 2 J cm^{-2} . The reflection in the upper right corner corresponds to the (02.10) reflection of the sapphire substrate.

served as a very sharp peak in reciprocal space, identified by an alignment of q_{\parallel} with the corresponding asymmetric reciprocal space vector of the substrate. Note that this peak cannot be observed for the here presented samples. A reason for this could be that Makushko *et al.* observed this for thin films with thickness of 30 nm only. Every film but the thinnest in Fig. 4.24 exceed this critical thickness. Another reason for the missing sharp peak could be that the herein probed (02.10) plane has only 50 % of the intensity of the (10.10) reflection [95, mp-19399].

When looking into the remaining samples that were fabricated with larger laser spot sizes but similar thickness of 50 nm (bluish squares in Fig. 4.23), it becomes clear that the o.o.p. strain is also slightly reduced for lower fluences. But note that this effect is less dominant when compared to the influence of thickness.

In Fig. 4.25, the ω -FWHM is depicted in dependence on the film thickness and laser fluence for the 1st batch. As before, consider the samples with smallest laser spot size (largest fluence) first: increasing the thickness is clearly correlated to a decreasing ω -FWHM. Therefore, thicker samples yield *both* less strained and more crystalline films. This is an unexpected result, because as shown in section 2.3.2, relaxation is mediated by dislocations which should worsen the crystal quality. Note that there is an outlier to this behavior for the sample with a thickness of approx. 30 nm. When considering the ω -pattern of this sample (Fig. B.2a), it becomes clear that the non-VOIGT shape makes the determination of FWHM difficult. Therefore, not too much attention should be paid to this data point. When considering the samples fabricated with lower fluences (bluish squares in Fig. 4.25), a much more dominant influence of laser spot size on the crystallinity can be observed. This can be summarized by stating that the thickness of the samples is the dominant influence on the o.o.p. strain, because the thickest

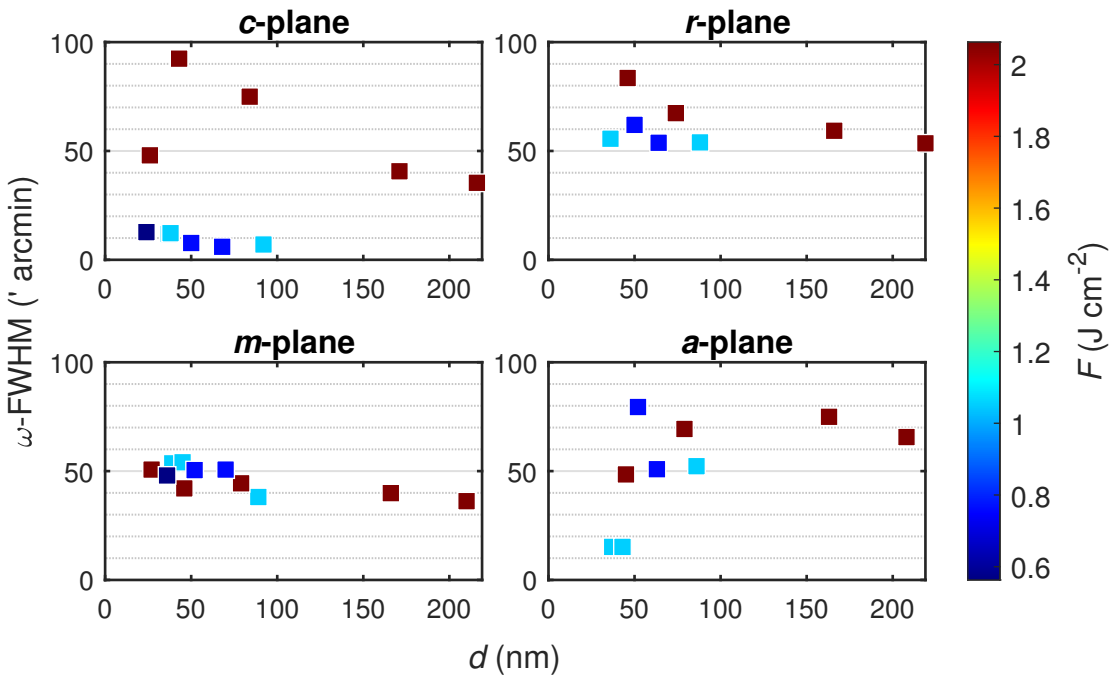


Figure 4.25: ω -FWHM for all samples from the 1st batch, depending on thickness and laser fluence (false color). The corresponding diffractograms are depicted in Fig. B.5.

samples yielded less strain than the thinner samples with lowest fluence (Fig. 4.23). However, for the ω -FWHM, the reverse is observed, namely that even the thickest samples (which exhibit better quality than thinner samples of the same lens position) have a much higher ω -FWHM when compared to thinner samples fabricated with less fluence. This can be seen in Fig. B.3, where the ω -FWHM is visualized depending on the o.o.p. strain of the corresponding sample: A linear behavior (correlation) is observed for each set fluence; but there are two different regimes in total, with the high-fluence regime generally showing higher ω -FWHM.

c-plane: Pulse Energy Variation

The o.o.p. strain for the *c*-plane oriented samples fabricated with various laser pulse energies, but constant laser spot size, are depicted in Fig. 4.26. Note that there is still a distribution of thickness from 100 to 200 nm, even though it was tried to counteract this by adjusting the pulse numbers. Therefore, the thickness is also displayed via false color to account for the convolution of thickness with laser fluence. The strain is overall smaller ($< 2\%$) than for the 1st batch, because the 2nd batch contained samples with thickness $t > 100$ nm which yields smaller strains as seen before. No systematic dependence on the laser fluence is observed, which may be explained by the still remaining thickness distribution which overlaps the fluence variation. This effect could be strong enough to overshadow the impact of laser pulse energy, as it was shown in the previous experiments that the thickness is the dominant factor for the o.o.p. strain. For example, note the sample fabricated with $F = 1.5 \text{ J cm}^{-2}$ (dark green square in Fig. 4.26), which exhibits the lowest strain, even though having higher fluence

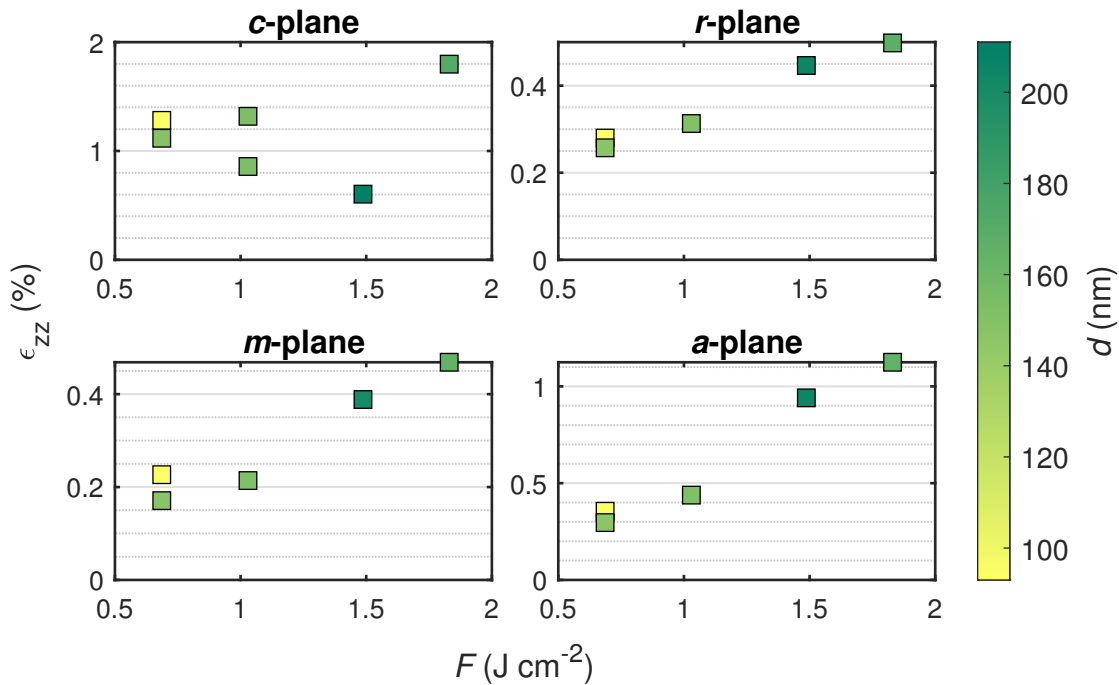


Figure 4.26: Out-of-plane strain calculated from 2θ - ω -patterns for all samples from the 2nd batch, depending on laser fluence and thickness (false color).

value than other samples. This can be explained by the fact that with $t = 200 \text{ nm}$, it is the thickest sample of the batch and therefore the lowest strain is expected (cf. Fig. 4.23).

In Fig. 4.27, the ω -FWHM is depicted depending on the laser fluence and film thickness for the 2nd batch. The previously observed relation is confirmed: increasing fluences result in higher ω -FWHMs. Namely, reducing the fluence by a factor of 2 results in a crystal quality improvement by one order of magnitude. Note that for a fluence of approx. 1 J cm^{-2} , two samples A and B with same thickness of 150 nm exhibit very different ω -FWHM of $\Delta\omega_A = 8'$ and $\Delta\omega_B = 49'$. The ω -patterns are depicted in Fig. B.2b. Note that both diffractograms have VOIGT shape, so the discrepancy may not be attributed to the determination of the FWHM. On the contrary, note that for the whole process B, which represents a set of samples with *c*-, *r*-, *m*- and *a*-orientation, a determination of FWHM was possible only for the *c*-plane samples⁽³⁾. In Fig. B.4, the ω -patterns of samples of all orientations from this process are depicted. The non-VOIGT shape for the orientations other than *c*-plane as well as the unexpectedly high ω -FWHM for *c*-plane sample indicate that the process yielded samples with poor crystal quality. The origin of this observation is not entirely clear, but since both A and B were conducted with the same process parameters with similar growthrate of $g_A = 3 \text{ pm pulse}^{-1}$ and $g_B = 3.75 \text{ pm pulse}^{-1}$, an effect must have influenced the thin film deposition substantially.

⁽³⁾ This is why in Fig. 4.27, only the upper left *c*-plane tile has two data points at $F \approx 1 \text{ J cm}^{-2}$.

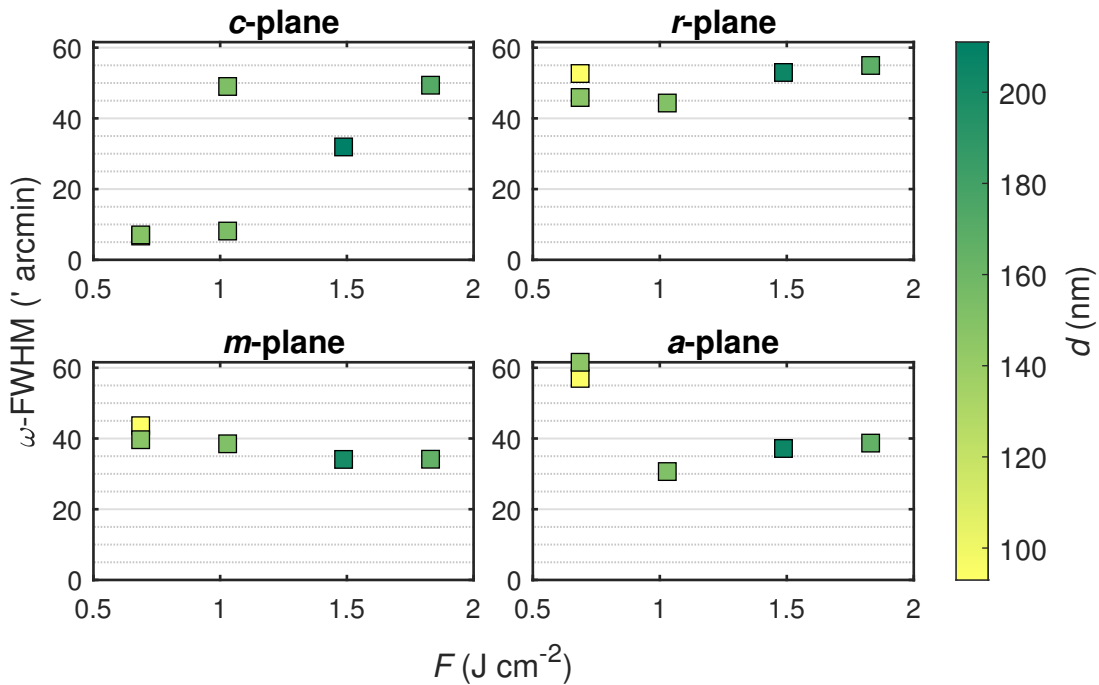


Figure 4.27: ω -FWHM for all samples from the 2nd batch, depending on laser fluence and thickness (false color). The corresponding diffractograms are depicted in Fig. B.6.

r-plane: Laser Spot Size Variation

In Fig. 4.23, the o.o.p. strain for the *r*-plane samples fabricated with varying laser spot size is shown. The overall strain is less than 1% and lower when compared to the *c*-plane samples, exhibiting values up to 4% for thin samples. In particular, the predicted value for o.o.p. strain during pseudomorphic growth of Cr_2O_3 on Al_2O_3 of 2.41% is not reached (cf. Tab. 2.4). As can be seen in a detailed view (Fig. B.7), the strain depends on the thickness: it decreases from 0.8% to 0.5% for an increment of thickness from 50 nm to 200 nm. This is in accordance to the behavior observed for the *c*-plane samples, albeit less pronounced. Furthermore, for a fixed thickness, decreasing the fluence also results in less strained thin films, which is similar to the behavior of the *c*-plane samples. The ω -FWHM obtained from the (02.4) reflection is depicted in Fig. 4.25. Similar to the *c*-plane samples – but less pronounced–, increasing the thickness results in less mosaicity, which is also achieved by reducing the fluence. Note that the overall ω -FWHM is between 50' and 90' which is significantly higher than for the *c*-plane samples, where a lower fluence yielded samples with $\Delta\omega < 10'$ (cf. Fig. 4.25). Therefore, increasing the thickness and reducing the fluence by varying laser spot position may increase the crystal quality, but not to an amount comparable to *c*-plane oriented thin films.

r-plane: Pulse Energy Variation

In Fig. 4.26, the o.o.p. strain is depicted for varying laser pulse energies (2nd batch). Independent of thickness, the fluence determines the strain of the thin films. The

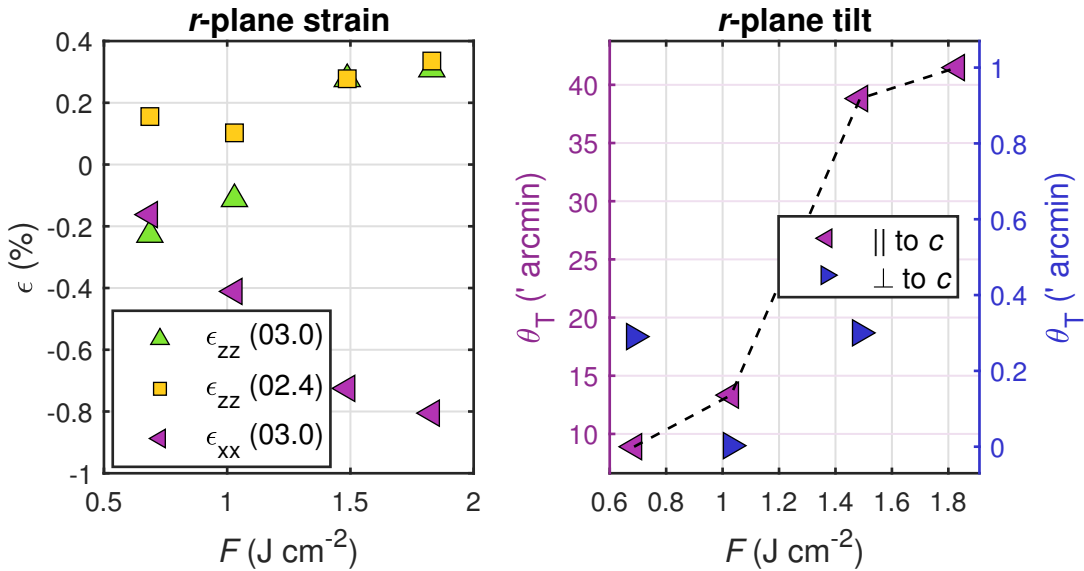


Figure 4.28: In-plane and out-of-plane strain for the *r*-plane samples from the 2nd batch, calculated from the peak positions of the RSMs described in 4.3.1 (left). Tilt along the *x*-axis (purple ordinate) and *y*-axis (blue ordinate), determined from symmetric reflections (right). Note the different scaling of the ordinates, indicating less tilt along the *y*-axis.

overall strain is below 0.4 %, and thereby comparable to the samples obtained from processes in the 1st batch with larger laser spot sizes. A detailed view on the strain for those samples is given in Fig. 4.28 which is based on the evaluation of RSMs that were performed as described in 4.3.1. The o.o.p. strain was calculated from both asymmetric (green triangle) and symmetric (yellow squares) reflections. The latter is equivalent to the calculation from the peak position in 2θ - ω diffraction patterns. It can be observed that the increasing tensile o.o.p. strain comes along with an increasing i.p. compressive strain, ranging from -0.2 % to -0.8 %. Therefore, the o.o.p. strain may be attributed to a partial pseudomorphic growth mode, because the Al_2O_3 lattice constants are smaller than the ones for Cr_2O_3 . The compressive strain is then due to an aligning of in-plane lattice constants.

Note that the values for o.o.p. strain obtained from 2θ - ω -scans (cf. Fig. 4.26) are only qualitatively confirmed: the strain measured from the symmetric RSM is approx. 0.2 percentage points below the value obtained from 2θ - ω -scans. A comparison of both methods is given in Fig. 4.29, where both a 2θ - ω pattern and a symmetric RSM of the are depicted for one sample ($F = 1.1 \text{ J cm}^{-2}$), as well as the calculated strain for all samples with different laser pulse energy. The origin of this discrepancy may lie in on of the corrections that was applied the RSMs, but not to the 2θ - ω patterns. However, the correction of the substrate peak position in 2D reciprocal space (rotation and stretching, cf. section 3.2.4) corresponds to a shift of the whole 1D 2θ - ω pattern to match the substrate peak. The latter was done for the evaluation of 2θ - ω -scans on which Fig. 4.26 is based. But the correction of thin film tilt which is done for RSMs was not done for the 2θ - ω -scans. This can be seen in Fig. 4.29, where the 2θ - ω pattern

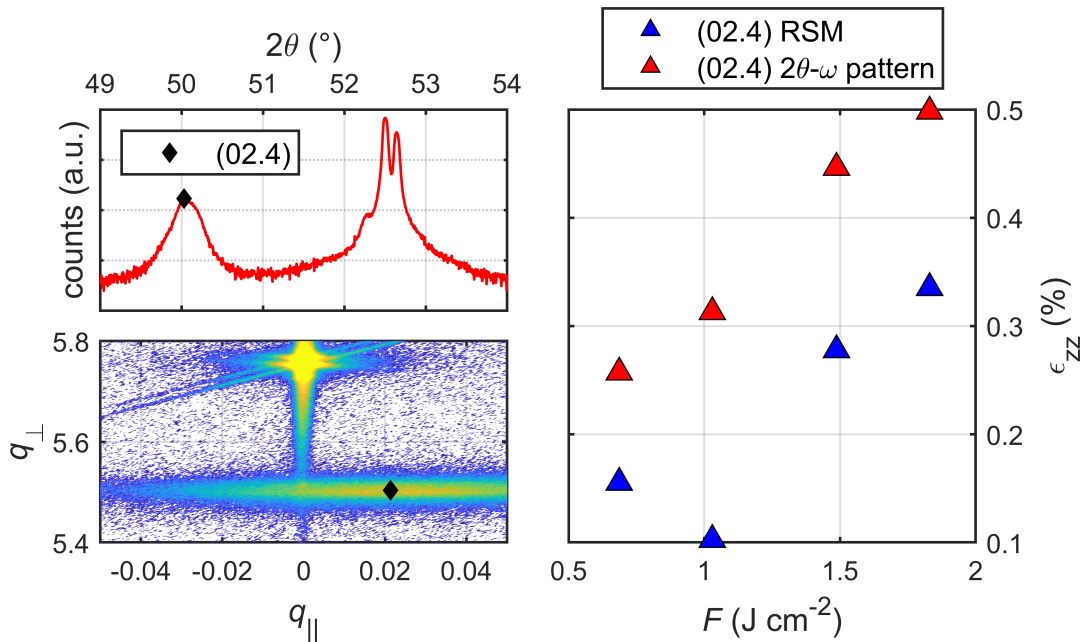


Figure 4.29: Out-of-plane strain for the r -plane samples fabricated with varying laser pulse energy (right). For the sample with $F = 1.1 \text{ J cm}^{-2}$, the $2\theta-\omega$ pattern (top left) and RSM (bottom left) are depicted. The black diamond (\blacklozenge) marks the position of the (02.4) reflection in the 1D $2\theta-\omega$ pattern and 2D RSM.

corresponds to a line with $q_{\parallel} = \text{const.} = 0$ in the reciprocal space. The peak on this line has the same q_{\perp} coordinate as the RSM peak not corrected to thin film tilt (both visualized as black diamonds, \blacklozenge). But if the (03.0) peak is rotated by the value of thin film tilt (counterclockwise), the q_{\perp} component slightly increases. Therefore it follows that

$$q_{\perp}^{\text{RSM,corrected}} > q_{\perp}^{\text{RSM,uncorrected}} = q_{\perp}^{2\theta-\omega},$$

which results in a smaller o.o.p. lattice constant obtained from RSMs. Therefore, the o.o.p. strain is smaller, when determined from symmetric RSMs. Note that a ω -optimization prior to a $2\theta-\omega$ -scan is done for correcting a tilt of the *substrate*, which is different from the correction of thin film tilt.

But even though this is a significant difference in evaluation between $2\theta-\omega$ -patterns and RSMs, the discrepancy between both methods does not change significantly when the thin film tilt decreases from $40'$ to $10'$. So further analysis has to be done for the applied evaluation methods. In general it has to be noted that the precision of the o.o.p. strain obtained from RSMs depends on (i) the peak position of the reflection, (ii) the peak position of the corresponding substrate peak (for substrate correction) and (iii) the peak position of the asymmetric peaks (for shear correction, not done for r -plane). These values are subject to a certain amount of uncertainty, which results in an ill-defined error.

Another observation is that the o.o.p. strain obtained from symmetric (yellow squares) and asymmetric reflections (green triangles) aligns for the two samples fabricated with higher fluences only (cf. Fig. 4.28). The discrepancy observed for the

lower fluences is unexpected. In Fig. 4.30, all symmetric and asymmetric RSMs are displayed. For the samples fabricated with 650 mJ and 800 mJ, accounting for the thin film tilt will result in a counterclockwise rotation of the reciprocal space. Therefore, the observed (03.0) reflection (■) has a smaller q_{\perp} component compared to the predicted (◆) peak position (after rotation). This results in tensile (positive) strain – which is in accordance with the values obtained from both symmetric RSM reflections and $2\theta\text{-}\omega$ patterns. For the samples with 300 mJ and 450 mJ, however, the thin film tilt is sufficiently small to result in compressive (negative) strain, i.e. the rotation of reciprocal space does not result in a smaller out-of-plane component q_{\perp} of the thin film (■) compared to the bulk value (◆).

and is probably due to an error in evaluation of the RSMs. This is supported by the fact that for those two data points, the strain obtained from asymmetric reflections is almost exactly mirroring the value obtained from the symmetric reflections.

As predicted by Grundmann and Lorenz [81], partially relaxed *r*-plane thin films should exhibit a tilt of the thin film with respect to the substrate. This tilt is indeed observed along the *x*-axis for all values of fluence, ranging from approx. $10'$ to $40'$ (purple triangles in Fig. 4.28). A corresponding tilt along the *y*-axis is not observed: there, the tilt angles are two orders of magnitude lower and below $0.4'$. This is in agreement with elasticity theory which predicts a tilt only along the *x*-axis, because the prismatic slip systems responsible for relaxation along the *y*-axis yield tilt components of the BURGER's vector that cancel out on average (cf. section 2.3.2). But note that the thin film tilt increases for higher fluences, which also results in a higher o.o.p. strain. This observation is unexpected, because the thin film tilt is a result of *relaxation*, whereas strain is a result of partial *pseudomorphic* growth. So according to strain, higher fluences result in less relaxed layers – according to tilt, higher fluences result in more relaxed layers. This result indicates that an interplay of both processes is present and that for growth modes that exhibit no partially relaxed behavior, more sophisticated models for the relaxation mechanism must be applied.

The ω -FWHM of the *r*-plane samples of the 2nd batch is approx. $50'$ and has no significant dependence on both fluence or thickness (Fig. 4.27). This confirms the previously obtained result for the samples fabricated with varying laser spot sizes.

***m*- and *a*-plane: Laser Spot Size Variation**

In Fig. 4.23, the o.o.p. strain for the *m*- and *a*-plane oriented samples of the 1st batch (laser spot size variation) is depicted. The maximum strain which is reached for high fluences is approx. 0.8 % and 1.5 % for *m*- and *a*-plane, respectively. Those values are far below the predicted values for pseudomorphic growth, which are 3.67 % (*m*-plane) and 3.63 % (*a*-plane). This indicates relaxed growth. In Fig. B.7 it can be seen that for higher thicknesses, the strain reduces only very slightly. The *m*-plane outlier at a thickness of 25 nm can be explained by the very low peak intensity of the (30.0)

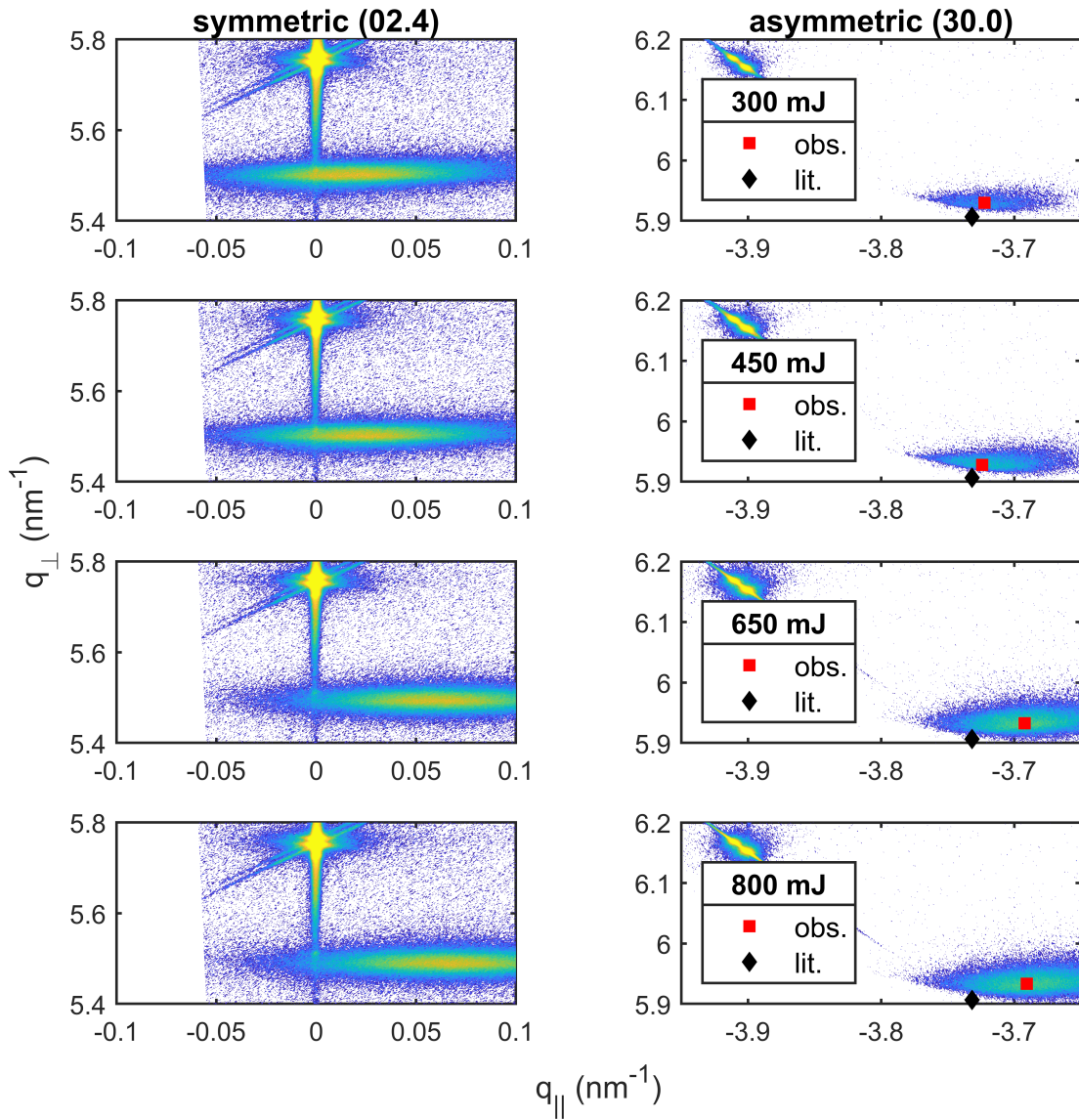


Figure 4.30: Reciprocal space maps of four *r*-plane oriented thin films fabricated with different laser pulse energy. The probed reflections are symmetric (02.4) (left) and asymmetric (30.0) (right). The peak with larger q_{\perp} component corresponds to the substrate. For the RSMs of the asymmetric reflections, the expected peak position (\blacklozenge) as well as the observed peak positions (\blacksquare) are indicated. Note that the RSMs are already corrected such that the substrate peak aligns with the expected position. A thin film tilt is indicated by the nonzero in-plane component of the symmetric (02.4) reflection. For determination of thin film lattice constants, the RSM is rotated by the observed thin film tilt, which is not visualized in these images.

reflection in the 2θ - ω pattern, which causes a larger uncertainty for this value. Overall, the fluence is the determining parameter for the strain, allowing strain values of down to 0 % for *a*-plane samples.

In Fig. 4.25, the ω -FWHM for both *m*- and *a*-plane samples is depicted. For *m*-plane, the ω -FWHM is approx. 50' for all fluences and thicknesses – only a small decrease for higher thicknesses is observed. As a result, in Fig. B.3, two regimes of high and low fluence can be distinguished, where each regime itself comes with a correlation indicating better crystallinity with less strain. However, altogether, a slight negative correlation can be observed, i.e. better crystallinity comes at the cost of higher strain. For *a*-plane samples, no significant dependence on fluence can be observed. On the contrary, there seems to be an increase in ω -FWHM for increasing thicknesses up to approx. 100 nm. This behavior differs from all other orientations observed and could be attributed to an unusual shape of the ω -patterns. In Fig. 4.31, such a pattern is depicted and has clearly no VOIGT-shape. Rather, the pattern consists of an exponential tail (linear in logarithmic intensity axis) for about 1.5° and a very sharp 2nd peak with a small FWHM on top of it. This shape is observed for almost every *a*-plane sample, as can be seen by the various diffractograms shown in Fig. B.5. The sharp peak is located at the maximum of the underlying broader peak and can therefore not be attributed to Al_2O_3 or another phase of Cr_2O_3 , because then it would not shift together with the (22.0) peak of the α -phase of Cr_2O_3 . This is also supported by the fact that no anomaly is observed in the 2θ - ω -patterns (not shown). This behavior has previously been observed for ZnO thin films grown on *c*-plane silicon [96, 97]. There, the broader peak contribution is attributed to a degradation at the interface region [96] and the sharp peak is present for a weakly disordered film, where the misfit to the substrate is damped through the underlying film. As shown by Durand *et al.* [97], the ω -FWHM of the narrow peak is limited by the instrumental resolution – they could resolve a broadening of 5 arcseconds for this peak. This behavior has also been observed for *c*-plane oriented Cr_2O_3 thin films fabricated by PLD [23]. In Fig. 4.31b, several ω -patterns are depicted for thin films of different thickness. For a layer thickness of 30 nm, a broad peak with an overlaying higher intensity peak is observable, which is not narrow but exhibits a plateau with a width of approx. 0.25°. For increasing film thicknesses, the FWHM of both the broader and narrow peak decrease, confirming the growth of a higher crystalline layer. Henceforth, the crystallinity of *a*-plane Cr_2O_3 thin films should be assessed by a two-layer model when determining the FWHM of the corresponding ω patterns.

***m*- and *a*-plane: Pulse Energy Variation**

In Fig. 4.26, the o.o.p. strain for the *m*- and *a*-plane oriented samples of the 1st batch is depicted. The strain ranges from 0.15 % (0.3 %) to 0.45 % (1.1 %) for *m*-plane (*a*-plane) samples. A clear dependence on fluence can be observed, whereas the thickness has

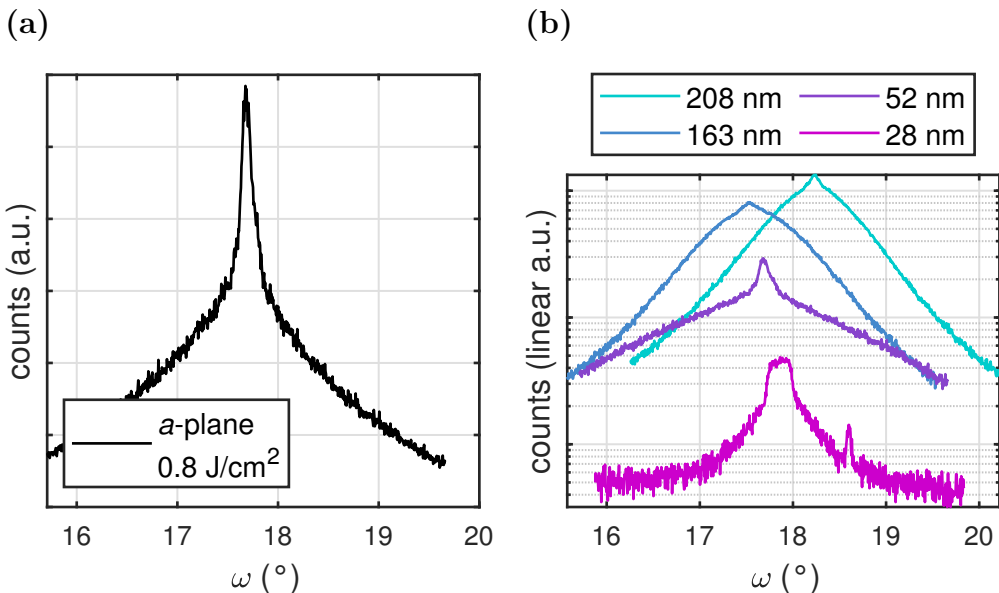


Figure 4.31: ω -pattern of a -plane samples from the 1st batch: (a) a sample with linear representation and (b) samples with varying thickness in logarithmic representation.

no influence on the o.o.p. strain at all. The complete in- and out-of-plane strains for m -plane samples are depicted in Fig. 4.32a. With increasing o.o.p. strain, the i.p. strain also increases, which indicates a pseudomorphic growth mode. Note that the i.p. strain is, in the range of uncertainty, the same along both x - and y -direction, even though both axes are not equivalent. As for r -plane samples (cf. Fig. 4.28), the o.o.p. strain is systematically smaller by 0.15 percentage points, compared to the values obtained from peak positions in 2θ - ω -patterns (Fig. 4.26). 2θ - ω -scans probe for symmetric reflections only, which is why shear stresses cannot be corrected by this method. However, those angles are rather small ($< 3'$, cf. Fig. 4.32a), which is why it is unplausible that this is the origin of the discrepancy. Moreover, as discussed for the r -plane samples, a thin film tilt can be observed, but the discrepancy does not change with varying tilt angles, which makes a correlation between both implausible.

As predicted by Grundmann [75] and demonstrated by Kneiß *et al.* [78], a significant tilt of the thin film is observed along the x -direction (purple triangles in Fig. 4.32a), which ranges from $20'$ to $40'$ and increases with higher fluences. Furthermore, a small shear Ψ_S of up to $2'$ is observed along this axis. On the contrary, a thin film tilt and a shear tilt below $1'$ are observed in y -direction (not shown). This is also in accordance with the predicted slip systems (cf. 2.3.2), which should result in no net tilt along the y -axis. However, as it is the case for the r -oriented samples, this thin film tilt – acting as an indicator for relaxation – increases with higher fluences. This is in contrast to the observation of decreasing relaxation with higher fluences due to increasing i.p. and o.o.p. strain. More investigations are needed to explain this effect.

In a qualitative sense, a similar behavior for a -plane samples is observed when investigating both in- and out-of-plane strain (Fig. 4.32b). However, the i.p. strain is 0.66 percentage points larger along the y -direction compared to x -direction for layers

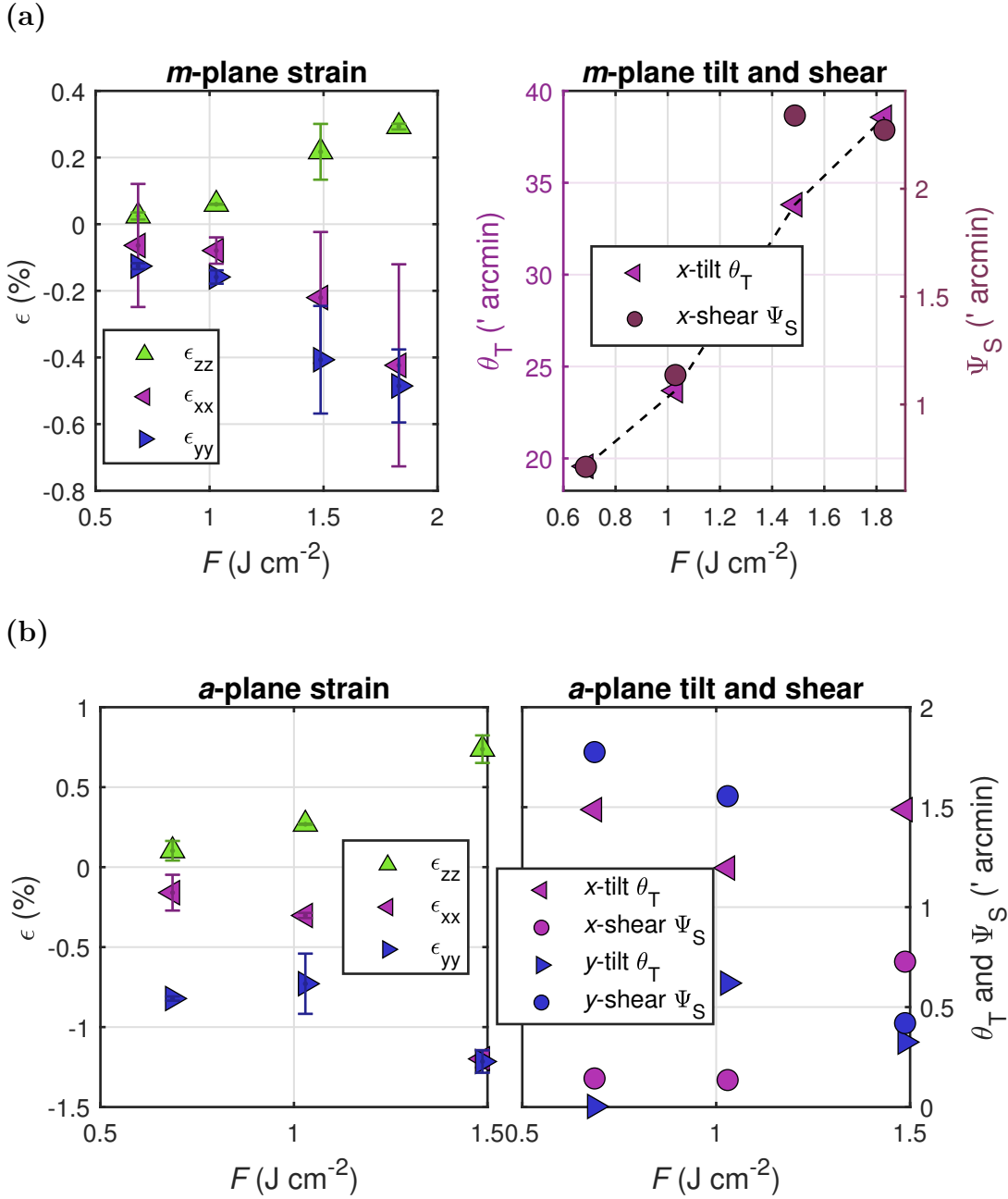


Figure 4.32: Left: In-plane (along x - and y -axis) and out-of-plane strain for the (a) m -oriented and (b) a -oriented samples from the 2nd batch, i.e. samples fabricated with varying laser pulse energy. The data was calculated from the peak positions of the RSMs described in section 4.3.1. Right: Shear (circles) and tilt (triangles) of thin films determined by asymmetric and symmetric reflections, respectively. The values were determined along x -axis and y -axis, but for m -plane samples, only the values along x -direction are shown.

Table 4.4: Strain, ω -FWHM and RMS roughness for two selected m -plane oriented Cr_2O_3 thin films that were investigated via AFM.

Id	thickness t	fluence F	strain ϵ_{zz}	ω -FWHM	RMS roughness
L.02	89 nm	1.05 J cm^{-2}	0.32 %	$38.1'$	2.5 nm
L.05	79 nm	2.06 J cm^{-2}	0.9 %	$44.4'$	1.9 nm

with less strain ($F = 0.7 \text{ J cm}^{-2}$). This discrepancy reduces for thin films that are more strained in total. Furthermore, as for the other orientations, the o.o.p. strain is systematically lower when compared to the values obtained from 2θ - ω -patterns, namely by 0.15 percentage points. The reasons for this effect are presumably the same as for the m -plane oriented samples. The shear and tilt angles for a -plane samples are depicted in Fig. 4.32b. As predicted by Grundmann [75], no tilt is observed along both the x -axis ($< 1.5'$) and y -axis ($< 0.7'$). A small shear angle of around $1.5'$ is observed along the y -axis.

Finally, the mosaicity for both m - and a -plane samples is depicted in Fig. 4.27. For m -plane oriented samples, the ω -FWHM is approx. $40'$ and decreases slightly with higher fluences, which is in contrast to the increasing strain. For a -plane samples, a large spread similar to the samples of the 1st batch (cf. Fig. 4.25) is observed. But, again, this observation is probably due to the specific shape of ω -patterns for the a -plane samples. In Fig. B.6, the diffractograms are depicted and a severe deviation from the VOIGT shape can be identified. Therefore, determination of the FWHM is hindered and the large spread of values explained.

For two selected samples, Atomic Force Microscopy (AFM) measurements were performed by M. Sc. C. Dethloff and the height profiles are displayed as false color images in Fig. 4.33. The sample L.02 (Fig. 4.33a,b) was fabricated with a larger laser spot size compared to the sample L.05 (Fig. 4.33c,d). The Root Mean Square (RMS) roughness for each sample was determined from the topography of a $2 \times 2 \mu\text{m}^2$ and $5 \times 5 \mu\text{m}^2$ probed area. These values as well as other details are listed in Tab. 4.4. In general, the surface morphology is comparable to the results obtained before for $\alpha\text{-Ga}_2\text{O}_3$ thin films fabricated by PLD, where RMS roughnesses of 0.6 to 3.5 nm were achieved for different growth temperatures [27]. No significant difference in surface morphology could be observed for both samples. However, the sample fabricated with higher fluence L.05 exhibits several stripes on the surface (cf. Fig. 4.33d). They are presumably not a measurement artifact, because they remained during repeated scans of the surface (not shown). Therefore, although having slightly larger RMS roughness, the fabrication with larger laser spot size (L.02) yields more homogeneous surfaces.

In Fig. 4.34, the transmission spectra of selected m -plane oriented samples from the 1st batch are depicted. The fluence does not have a significant influence on the absorption onset, however, the thickness is decisive for the shape of the absorption edge, which is due to thin film interferences. The onset of absorption E_{opt} is approx.

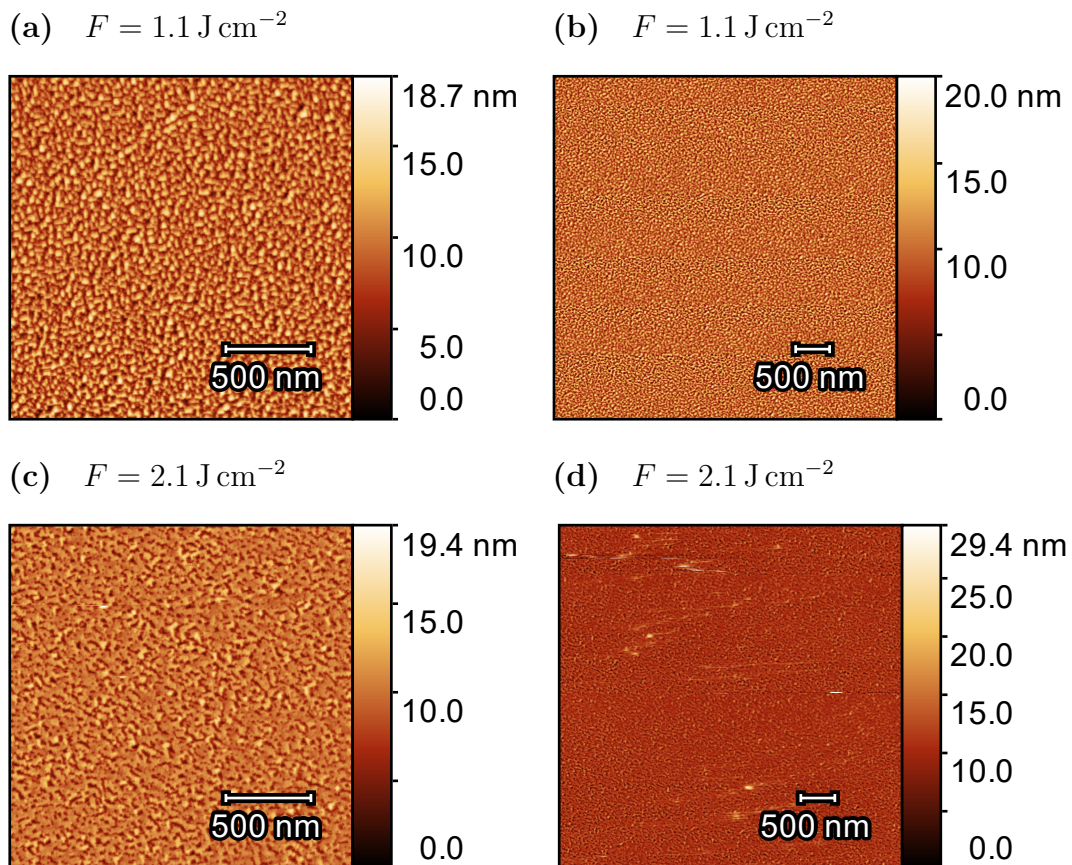


Figure 4.33: AFM false color images of two samples with (a, b) larger laser spot size and fluence of 1.1 J cm^{-2} (L.02) and (c, d) smaller laser spot size and laser fluence of 2.1 J cm^{-2} (L.05). The probed areas are $2 \times 2 \mu\text{m}^2$ and $5 \times 5 \mu\text{m}^2$ for the left and right panels, respectively.

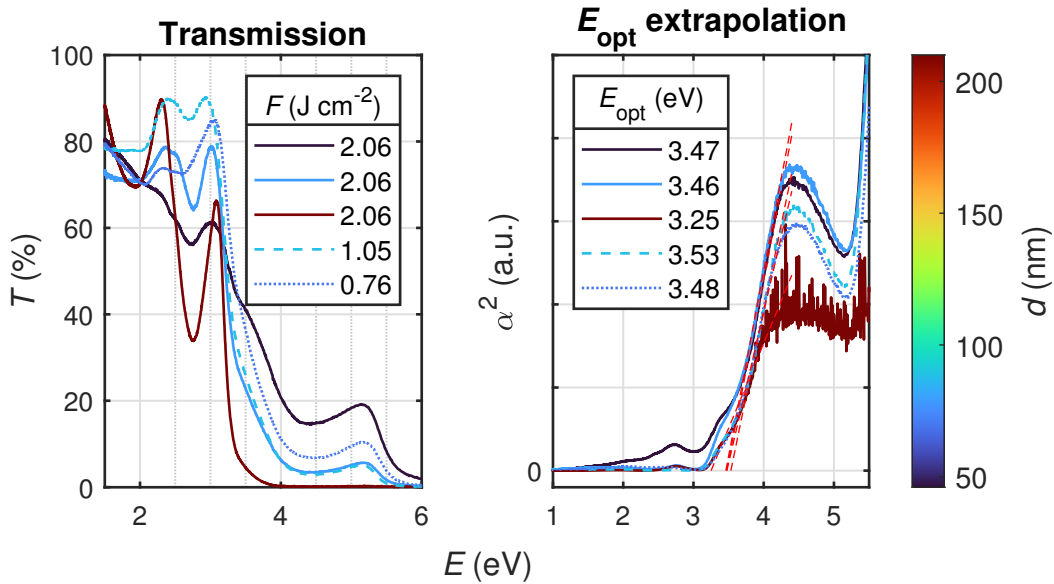


Figure 4.34: Transmission spectra (left) of selected *m*-plane oriented samples from the 1st batch. The samples differed in thickness and laser fluence on the target surface, achieved by varying lens positions. The α^2 vs. E plot (right) of the mentioned samples, determined by assuming a direct band gap of Cr_2O_3 (cf. 3.6 and 4.1).

3.5 eV for all samples of different thickness and fluence. This is in accordance with the value obtained for the samples of the initial Cr_2O_3 batch (cf. 4.1 and Fig. 4.5b).

4.3.4 Conclusion

The out-of-plane strain and in-plane strain of Cr_2O_3 thin films with different crystal orientations were investigated depending on the laser fluence on the target during deposition via PLD. The variation in laser fluence was achieved by either increasing the laser spot size or by decreasing the laser pulse energy. Samples with *c*-orientation grow fully pseudomorphic for low film thicknesses, whereas the samples with *r*-, *m*- and *a*-orientation are partially relaxed. The thickness is a crucial parameter for *c*- and *r*-plane samples, whereas the laser fluence on the target strongly influences the crystal structure of *m*- and *a*-plane samples. It can be concluded that the thickness of the thin films is more relevant for orientations that have more out-of-plane *c*-axis component. For *c*- and *r*-orientation, less laser fluence – no matter whether via larger laser spot sizes or reduced laser pulse energy – results in less FWHM in ω -patterns and thus better crystallinity. For *m*-plane samples, a reversed behavior is observed – however, the dependence on fluence is much less pronounced. A layered structure of *a*-plane thin films hardens the comparison of the ω -FWHM for this orientation. Furthermore, for *r*-, *m*- and *a*-plane oriented samples, thin film tilts have been observed in the directions that were previously observed for relaxed $\alpha\text{-Ga}_2\text{O}_3$ layers on Al_2O_3 [78, 81] (cf. Tab. 2.4b).

To understand the dependence between relaxation, crystallinity and thin film tilt for Cr_2O_3 *m*-plane thin films, a comparison to similarly structured $\alpha\text{-Ga}_2\text{O}_3$ can be

made: In Kneiß *et al.* [78], fully relaxed *m*-plane α -(Al_xGa_{1-x})₂O₃ thin films exhibited a tilt that was dependent on the aluminum content, and therefore on relaxed lattice constants. For pure α -Ga₂O₃ layers (zero aluminum content), a thin film tilt of 36' was observed, which is in accordance to the here observed angles of 20' to 40' (cf. Fig. 4.32a). In this work, however, due to variations in laser fluence, partially relaxed *m*-plane Cr₂O₃ thin films with out-of-plane strain ranging from 0.02 % to 0.3 %⁽⁴⁾ could be fabricated (Fig. 4.32a). It was observed that samples with less out-of-plane strain – i.e. smaller out-of-plane lattice constants – exhibit smaller thin film tilts. Note that due to the fact that Al₂O₃ has smaller lattice constants than relaxed Cr₂O₃, a decrease in lattice constants is directly related to a decreasing mismatch between substrate and thin film. Therefore, the here reported results are in accordance to Kneiß *et al.* [78] in the sense that a reduction in lattice mismatch reduces the thin film tilt. Furthermore, reducing the laser fluence also results in a slightly higher ω -FWHM (Fig. 4.27), which could correspond to an increased dislocation density. When applying a heteroepitaxial model as displayed in Fig. 2.4 [79], this reduced dislocation density results in less thin film tilt, which is indeed observed. Therefore, an increasing laser fluence on the PLD target results in both increasing strain and decreasing ω -FWHM which manifest in larger thin film tilts. These effects can be summarized as less partially relaxed layers.

However, note that the importance of reduced laser fluence for more relaxed thin films is not explained yet. By taking the reduced kinetic energy of the plasma species into account [98], one can infer that the growth dynamics are altered in such a way that the formation of dislocations is favored. In general, note that more sophisticated methods like TEM should be applied to get a more detailed view into the formation and density of dislocations, which are fundamental to relaxation and thin film tilt.

No investigations of the influence of laser fluence on the structural properties of Cr₂O₃ thin films fabricated by PLD have been done so far in the literature. The only report on varying laser fluence from 1.6 to 3.7 J cm⁻² has been concerning the atomic ratio of Cr cations to O anions for deposition on silicon [59]. Most of the Cr₂O₃ thin films fabricated via PLD were deposited on *c*-plane sapphire [23, 49, 58]. None of those studies could identify the laser fluence as a crucial parameter influencing the crystallinity of the thin films (Fig. 4.27): the best ω -FWHM of 22' that was reported by Singh *et al.* [58] is larger than the here reported value of 7'. For *r*-plane oriented thin films reported by Punugupati *et al.* [57], an out-of-plane strain of 0.57 % could be identified, but no studies have been performed on the origin of this observation.

To determine the optimal deposition parameters of Cr₂O₃, one has to take the different orientations into account: Because the thickness is mostly relevant for *c*-plane oriented thin films, the choice of at least $t = 150$ nm results in the lowest strain and ω -FWHM. Furthermore, a laser spot size of 10 mm² and pulse energy of 300 mJ would result in the lowest strain for *r*-, *m*- and *a*-orientation. Note that this, however, results

⁽⁴⁾ According the RSMs. Note that there was a discrepancy between the strain values obtained from 2 θ - ω scans and RSMs.

in less crystalline films for those orientations (Fig. 4.27), as well as a very low growth rate. Therefore, a pulse energy of 450 mJ is chosen for future depositions due to the best crystal quality while maintaining strain of about 0.1% and 0.3% for *m*- and *a*-plane respectively. Those deposition parameters also result in low thin film tilts of about 15' and 25' for *r*- and *m*-plane samples, respectively. The laser fluence on the target is therefore 1.1 J cm^{-2} , and will be applied when depositing high quality buffer layers for $\alpha\text{-Ga}_2\text{O}_3$ thin films: The reduced compressive in-plane strain is desired to achieve low mismatch between the Cr_2O_3 and $\alpha\text{-Ga}_2\text{O}_3$ layer, as demonstrated in the following chapter.

4.4 Cr₂O₃ Buffer Layers for α -Ga₂O₃

A major motivation for investigating Cr₂O₃ thin films is a possible usage as buffer layer for isostructural α -Ga₂O₃, which has similar lattice parameters: Cr₂O₃ has a slightly larger *c* and smaller *a* lattice constant than α -Ga₂O₃ (Fig. 4.35). This could improve the crystal quality of α -Ga₂O₃ thin films due to reduced lattice mismatch when compared to Al₂O₃ [16]. For *c*-plane, the mismatch of α -Ga₂O₃ to Al₂O₃ and Cr₂O₃ is 4.6 % and 0.4 %, respectively. However, as shown in chapter 4.3, the in-plane compressive strain for Cr₂O₃ thin films on *c*-plane Al₂O₃ increases the mismatch between Cr₂O₃ and α -Ga₂O₃ slightly for the pseudomorphic grown thin films. However, when supplying sufficiently thick samples of at least 150 nm, this strain is negligible. On the other side, for *m*-plane samples, the mismatch of α -Ga₂O₃ to Al₂O₃ and Cr₂O₃ regarding the *c*-axis is 3.3 % and -1.2 %, respectively. Furthermore, as shown in the previous chapter, the in-plane compressive strain for *m*-plane Cr₂O₃ thin films yields less discrepancy between the *c* lattice constant of both sesquioxides. A similar argument can be drawn for *a*-plane samples. In the following, a proof of concept will be given that α -Ga₂O₃ can be successfully deposited on Cr₂O₃ buffer layers.

4.4.1 Experiment

For the Cr₂O₃ thin films, deposition parameters were chosen that yield the lowest strain and smallest ω -FWHM. Therefore, a lens position of -1 cm and a laser pulse energy of 450 mJ were applied. Note that 350 mJ would result in even less strain, but only at the cost of very low growth rates and less crystallinity. The Ga₂O₃ layer was deposited with a lens position of -2 cm and a laser pulse energy of 650 mJ, being known as optimal for α -Ga₂O₃ deposition in this chamber. This is the configuration that was used for depositing Cr₂O₃ in 4.1 and 4.2. By assuming a growth rate of 10 pm pulse⁻¹ – which is achieved for deposition with similar parameters at a different PLD chamber –, 15 000 pulses were applied to achieve a layer thickness of approx. 150 nm. The oxygen partial pressure was 3×10^{-4} mbar and the temperature was chosen to be approx.

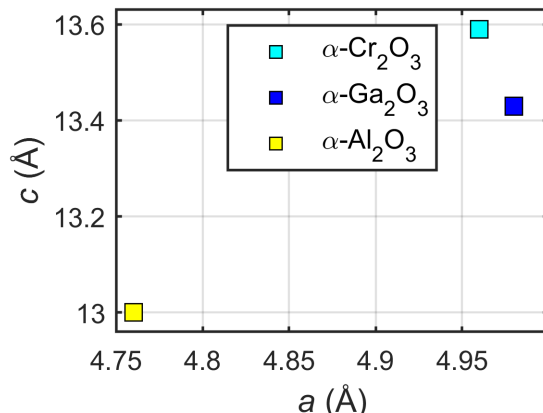


Figure 4.35: Lattice constants *a* and *c* for the three sesquioxides relevant in this work.

680 °C. Two approaches were chosen to deposit α -Ga₂O₃ of four different orientations *c*, *r*, *m* and *a*:

1. Deposition of Cr₂O₃ with subsequent *ex situ* analysis of the Cr₂O₃ layer under atmospheric conditions. Afterwards the Ga₂O₃ layer was deposited in an additional PLD process.
2. *In situ* deposition of Cr₂O₃ and Ga₂O₃ without returning to atmospheric conditions inbetween. Between both processes, the oxygen pressure was reduced and it was waited for 20 min to achieve thermodynamic equilibrium.

For the *ex situ* samples, RSMs around the exptected α -phase symmetric reflection were recorded before and after the deposition of the Ga₂O₃ layer to confirm the formation of the α -phase. Furthermore, 2θ-ω-scans were performed for all samples after deposition of the Ga₂O₃ layer to check whether other phases are present. To confirm the crystallinity of the Ga₂O₃ layer, RHEED patterns were recorded for the surfaces of all samples after deposition of the Ga₂O₃ layer.

The 2θ-ω patterns are compared to a reference Cr₂O₃ sample from chapter 4.3, fabricated with a pulse energy of 450 mJ. The theoretical predictions of the 2θ values for reflections of β -Ga₂O₃ were taken from the *Materials Project* [95, mp-886].

TEM and EDX measurements were performed by Dr. J. G. Fernandez from *Centre for Materials Science and Nanotechnology Physics*, Oslo, and kindly provided the images, shown in Figs. 4.38, 4.39 and 4.40.

4.4.2 Comparison of *in situ* and *ex situ* grown Ga₂O₃ on Cr₂O₃

The RHEED patterns of all samples from the *ex situ* and the *in situ* batch are depicted in Fig. 4.36a and Fig. 4.36b, respectively. From the periodic patterns it can be concluded that every surface is crystalline. Note that the mere observation of crystallinity does not indicate which phase of Ga₂O₃ is present on the samples.

c-plane α -Ga₂O₃ grown on Cr₂O₃

To determine the present crystal phases of the Ga₂O₃ thin film, in Fig. 4.37a, 2θ-ω patterns of the samples deposited on *c*-plane Al₂O₃ are depicted, namely the Cr₂O₃ reference sample (black), as well as the *ex situ* (blue) and *in situ* (red) samples. The peak at around 39.2° of the refefence sample is the (00.6) reflection of Cr₂O₃. This reflection is also attributed to the peaks at approx. 39.4° and 39.6° of the *ex situ* and *in situ* samples, respectively. The variation of peak position for the Cr₂O₃ layer may originate in the fact that for each process, the thickness may have varied. As discussed in chapter 4.3, this is a crucial factor for the out-of-plane strain and therefore the position of the reflection. In addition, two overlaying peaks occur at 40.14° for both

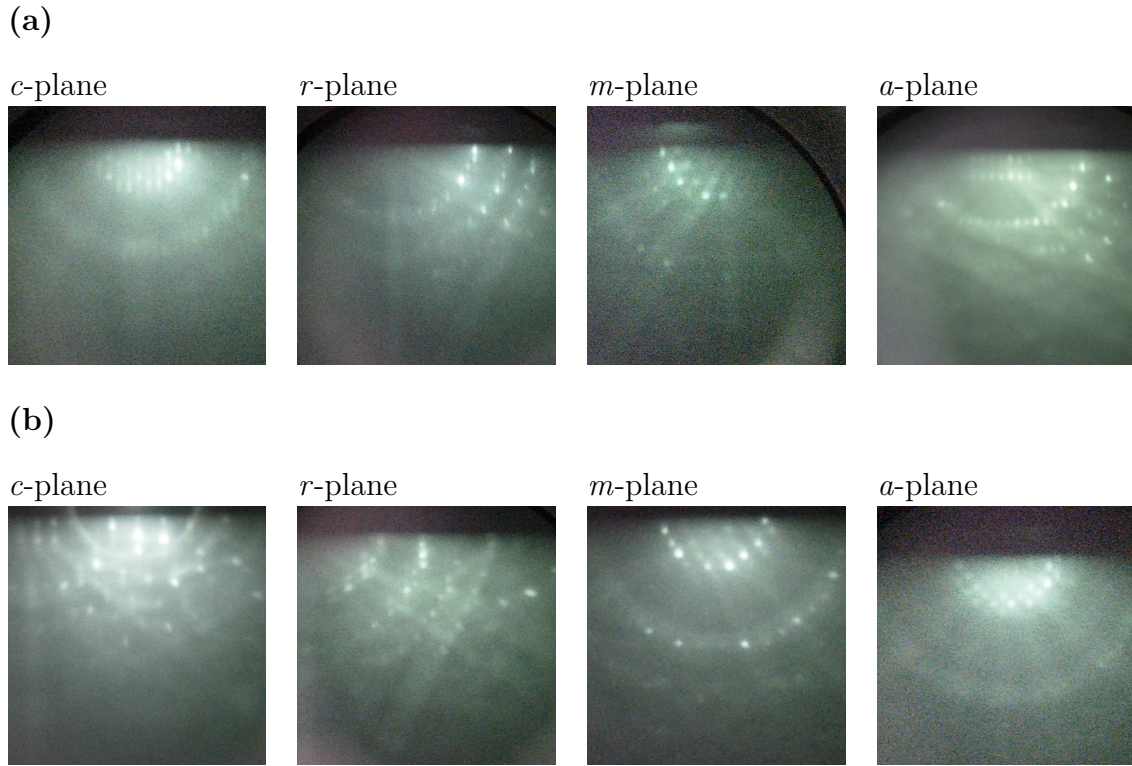


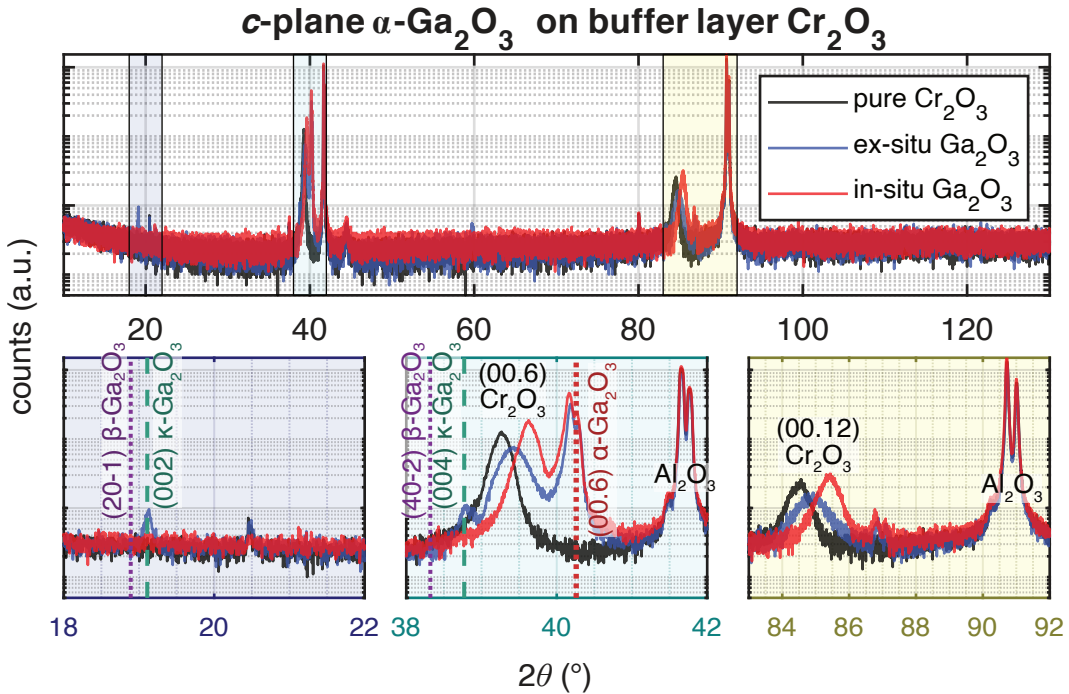
Figure 4.36: RHEED patterns of the α -Ga₂O₃ surface deposited (a) *ex situ* on Cr₂O₃ and (b) *in situ* on Cr₂O₃. Note that the patterns were recorded in arbitrary azimuth which is why they may differ between *ex situ* and *in situ* deposition. This is not necessarily a result of different crystal structure.

buffer layer processes. This is attributed to the (00.6) reflection of α -Ga₂O₃, because the predicted peak position is at 40.26° with a relative intensity of 3.37, and is therefore allowed. The presence of two peaks is attributed to the splitting between Cu-K α_1 and Cu-K α_2 radiation (*K α splitting*). Note that at approx. 86°, the higher order (00.12) reflection of Cr₂O₃ can be observed more dominantly than the (00.12) reflection of α -Ga₂O₃. This is due to the fact the the ratio of relative intensities of (00.12) to (00.6) is 29.6 % for Cr₂O₃ and only 1.4 % for α -Ga₂O₃.

For the *in situ* sample, no additional peaks are observed, indicating phase-pure deposition of *c*-plane Ga₂O₃ in the α -phase on *c*-plane Al₂O₃. For the *ex situ* sample, however, a peak occurs at 38.78° and both the β - and κ -phase of Ga₂O₃ have a predicted peak at this position, listed in Tab. 4.5. The observed peak is attributed to the (004) reflection of the κ -phase. A lower order of this reflection is also observed at 19.13°, which is attributed to the (002) reflection of κ -Ga₂O₃. Note that the peak observed at 20.4° is also observed for the Cr₂O₃ reference sample and can therefore not correspond to any Ga₂O₃ phase. It can be concluded that the *ex situ* growth of Ga₂O₃ on a *c*-plane Cr₂O₃ buffer layer results in both α -Ga₂O₃ and κ -Ga₂O₃, with the latter being much less pronounced.

In Fig. 4.37b, the RSMs of the *ex situ* *c*-plane sample are displayed before and after deposition of Ga₂O₃. Note that the image is cropped such that no substrate peak is visible. The previous result is confirmed that another phase has formed on top of

(a)



(b)

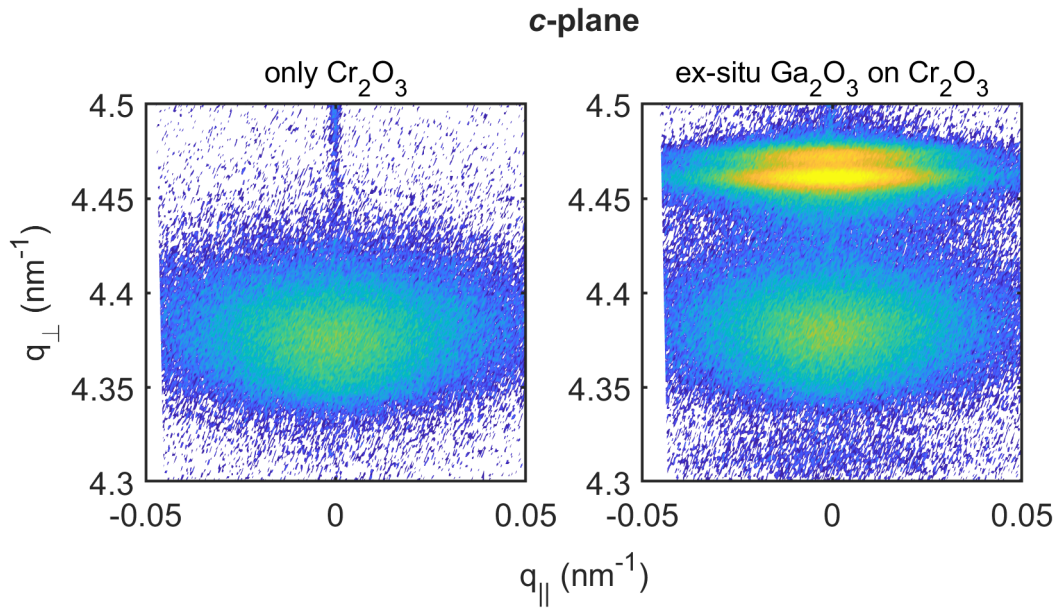


Figure 4.37: (a) $2\theta-\omega$ -patterns of the c -plane Cr_2O_3 reference sample (black), as well as the *ex situ* (blue) and *in situ* (red) buffer layer structures. The expected peak positions of $\beta\text{-Ga}_2\text{O}_3$ (purple dotted) and $\kappa\text{-Ga}_2\text{O}_3$ (green dashed) from Tab. 4.5 are indicated, as well as the (00.6) reflection of $\alpha\text{-Ga}_2\text{O}_3$ (red dotted). (b) RSM around the (00.6) reflection recorded before (left) and after (right) *ex situ* deposition of Ga_2O_3 .

Table 4.5: Selected reflections of $\beta\text{-Ga}_2\text{O}_3$ [95, mp-886] and $\alpha\text{-Ga}_2\text{O}_3$ [99] and their predicted positions in $2\theta\text{-}\omega$ patterns, as well as the observed peak position for Ga_2O_3 deposited *ex situ* on Cr_2O_3 (blue curve in Fig. 4.37a).

Phase	2θ	reflection	measured
$\beta\text{-Ga}_2\text{O}_3$	18.89°	(20 $\bar{1}$)	
$\alpha\text{-Ga}_2\text{O}_3$	19.11°	(002)	19.13°
$\beta\text{-Ga}_2\text{O}_3$	38.32°	(402)	
$\alpha\text{-Ga}_2\text{O}_3$	38.77°	(004)	38.78°

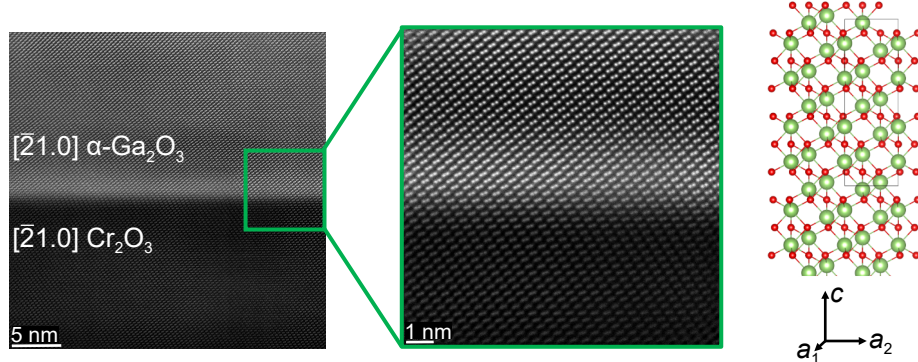


Figure 4.38: HAADF image of the interface between c -plane Cr_2O_3 and $\alpha\text{-Ga}_2\text{O}_3$. The $[21.0]$ direction is parallel to the electron beam, i.e. the a -plane is visible. Courtesy of Dr. J. G. Fernandez. The image of the $\alpha\text{-Ga}_2\text{O}_3$ crystal structure was made with VESTA Ver. 3 [47].

the Cr_2O_3 layer. No ω -scans were done, but the crystallinity can be estimated by the broadening in $q_{||}$ direction, which is less dominant in comparison to the Cr_2O_3 layer. Furthermore, the $\text{K}\alpha$ splitting indicates a highly crystalline thin film.

In Fig. 4.38, HAADF images are shown for the interface between $\alpha\text{-Ga}_2\text{O}_3$ and Cr_2O_3 . The c -axis points upwards, and the atom arrangement that is visible corresponds to the a -plane. The similar crystal structure can be clearly seen by comparing the lattice spacing of the upper and lower half plane. No dislocations form at the interface and the (00.1)-orientation of the Cr_2O_3 buffer continues for the Ga_2O_3 layer.

m-, a- and r-plane $\alpha\text{-Ga}_2\text{O}_3$ grown on Cr_2O_3

When comparing the peaks of m -plane buffer layer samples to the Cr_2O_3 reference sample, note that the (30.0) peak is shifted to lower angles (Fig. 4.41a), i.e. that the buffer layers are more strained when compared to the reference sample. Note that for the buffer layers, a new Cr_2O_3 target has been used. This could be the reason for the increased strain as shown in chapter 4.2, where target degradation reduced the peak shift in $2\theta\text{-}\omega$ patterns. Furthermore, two peaks can be observed for the buffer layer samples, which may originate in (i) either two peaks for Cr_2O_3 and $\alpha\text{-Ga}_2\text{O}_3$ each; or (ii) $\text{K}\alpha$ splitting of a (30.0) $\alpha\text{-Ga}_2\text{O}_3$ reflection on top of the Cr_2O_3 layer. Both explanations are favored by the fact that the expected peak position (red dotted

line) lays inbetween both peaks. The theoretical predictions of the 2θ positions also have similar distance as the two peaks observed (red and green dotted lines), favoring the first explanation. However, when considering Fig. 4.41b, it becomes clear that the origin is a $K\alpha$ splitting, because prior to the deposition of Ga_2O_3 , none of the peaks was present with the observed intensity. Therefore, the observed peaks must both stem from the α -phase of Ga_2O_3 . No other peaks are observed in the $2\theta\text{-}\omega$ pattern, therefore only the α -phase is present.

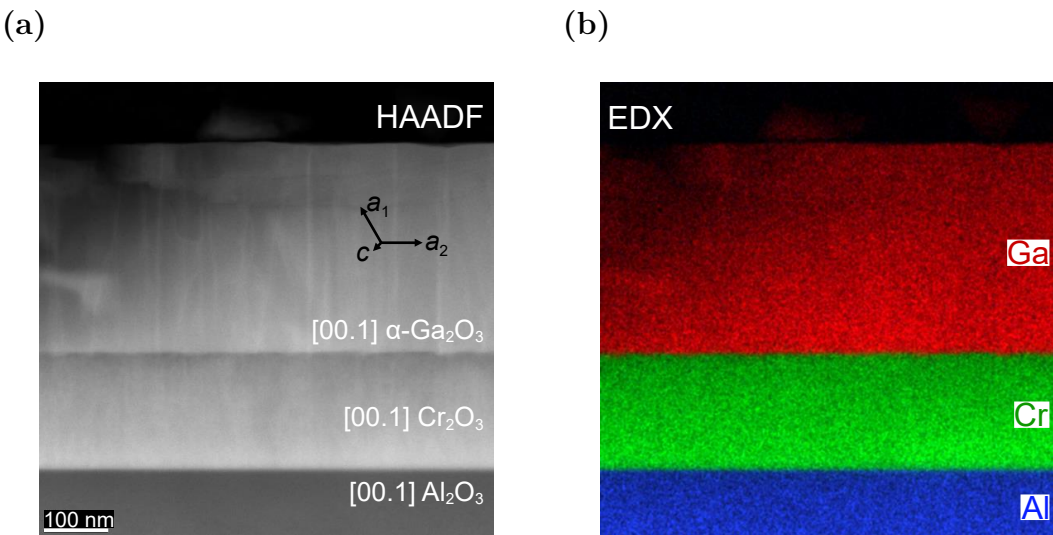


Figure 4.39: Images of the *m*-plane buffer layer structure: (a) HAADF image and (b) spatially resolved EDX data of the Al_2O_3 , Cr_2O_3 and $\alpha\text{-Ga}_2\text{O}_3$ layer. The c -axis is parallel to the electron beam. Courtesy of Dr. J. G. Fernandez.

In Fig. 4.39a, an HAADF image of the *m*-plane buffer layer structure is depicted. The [10.0] direction points upwards, and the atom arrangement that is visible corresponds to the c -plane. In the $\alpha\text{-Ga}_2\text{O}_3$ layer, threading dislocations can be seen. The expected composition of the layers is confirmed by spatially resolved EDX measurements (cf. Fig. 4.39b). A detailed view into the interface between Cr_2O_3 and $\alpha\text{-Ga}_2\text{O}_3$ is given in Fig. 4.40a. Similar to the c -plane structure, the (10.0) orientation of the buffer layer is continued in the $\alpha\text{-Ga}_2\text{O}_3$ layer, which exhibits very good crystal quality, as can be seen in Fig. 4.40b.

A similar behavior as for the *m*-plane samples can be observed in the $2\theta\text{-}\omega$ patterns of *a*-plane samples (Fig. 4.42a). The splitted peak is attributed to the (22.0) reflection of an $\alpha\text{-Ga}_2\text{O}_3$ layer and the peak on the left shoulder to the (22.0) reflection of Cr_2O_3 , which is shifted to lower angles in comparison to the reference sample. This behavior is also observed for the (11.0) reflections of both $\alpha\text{-Ga}_2\text{O}_3$ and Cr_2O_3 . This result is confirmed by the RSMs (Fig. 4.42b), where two peaks appear due to $K\alpha$ splitting after Ga_2O_3 deposition. The low broadening in $q_{||}$ direction as well as the $K\alpha$ splitting indicate good crystal quality.

The $2\theta\text{-}\omega$ patterns of the *r*-plane reference and buffer layer samples are depicted

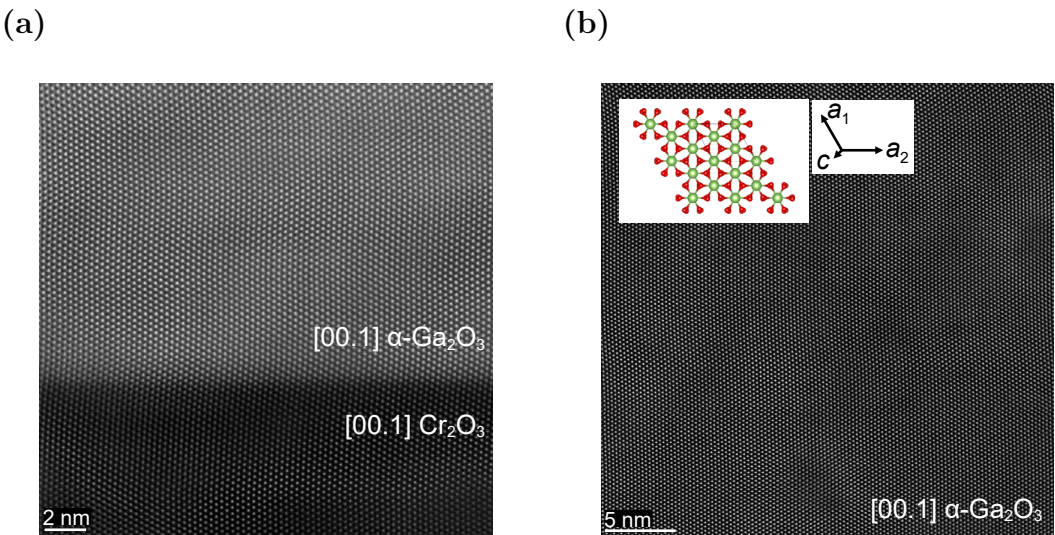


Figure 4.40: Images of the m -plane buffer layer structure: (a) HAADF image of the interface between Cr₂O₃ and α-Ga₂O₃. (b) HAADF representative image of the α-Ga₂O₃ layer. Courtesy of Dr. J. G. Fernandez. The image of the α-Ga₂O₃ crystal structure was made with VESTA Ver. 3 [47].

in Fig. 4.43a. Due to very close peak positions of the (02.4) reflection for both Cr₂O₃ and α-Ga₂O₃, a comparison with the reference sample (black) is not as straightforward as for the other orientations. No additional peak can be identified for the buffer layer samples. However, the RHEED patterns indicated a crystalline surface, which is why the only possible phase of the Ga₂O₃ layer is the α-phase. This is verified by RSMs of the *ex situ* sample in Fig. 4.43b: a significant increment in intensity can be observed at the expected peak position of (02.4) α-Ga₂O₃, which is due to the formation of α-phase Ga₂O₃ on *r*-plane Cr₂O₃.

4.4.3 Conclusion

Phase-pure deposition of α-Ga₂O₃ on Cr₂O₃ thin films was achieved for *c*-, *r*-, *m*- and *a*-plane oriented Al₂O₃ substrates. The orientation of both Cr₂O₃ and α-Ga₂O₃ thin film was the same as the respective substrate. For *ex situ* deposition of Ga₂O₃, XRD measurements indicate the presence of the α -phase of Ga₂O₃, which is less dominant than the α-phase. No optimization was performed for the deposition process, but the results serve as a proof of concept that the deposition of phase-pure α-Ga₂O₃ – especially in the *c*- and *r*-orientation – is possible on Cr₂O₃ buffer layers via PLD.

Especially the deposition of α-Ga₂O₃ in *c*-orientation has been a challenge in previous studies. Methods like mist-CVD or HVPE were able to deposit α-Ga₂O₃ on *c*-plane sapphire up to a critical thickness [20]. However, as pointed out by Schewski *et al.* [64], those thin films exhibited both rotational domains and a contribution of the β-Ga₂O₃ phase [100, 101]. Phase-pure deposition without rotational domains on Al₂O₃ can only be achieved pseudomorphically up to a thickness of only three monolayers [64]. The

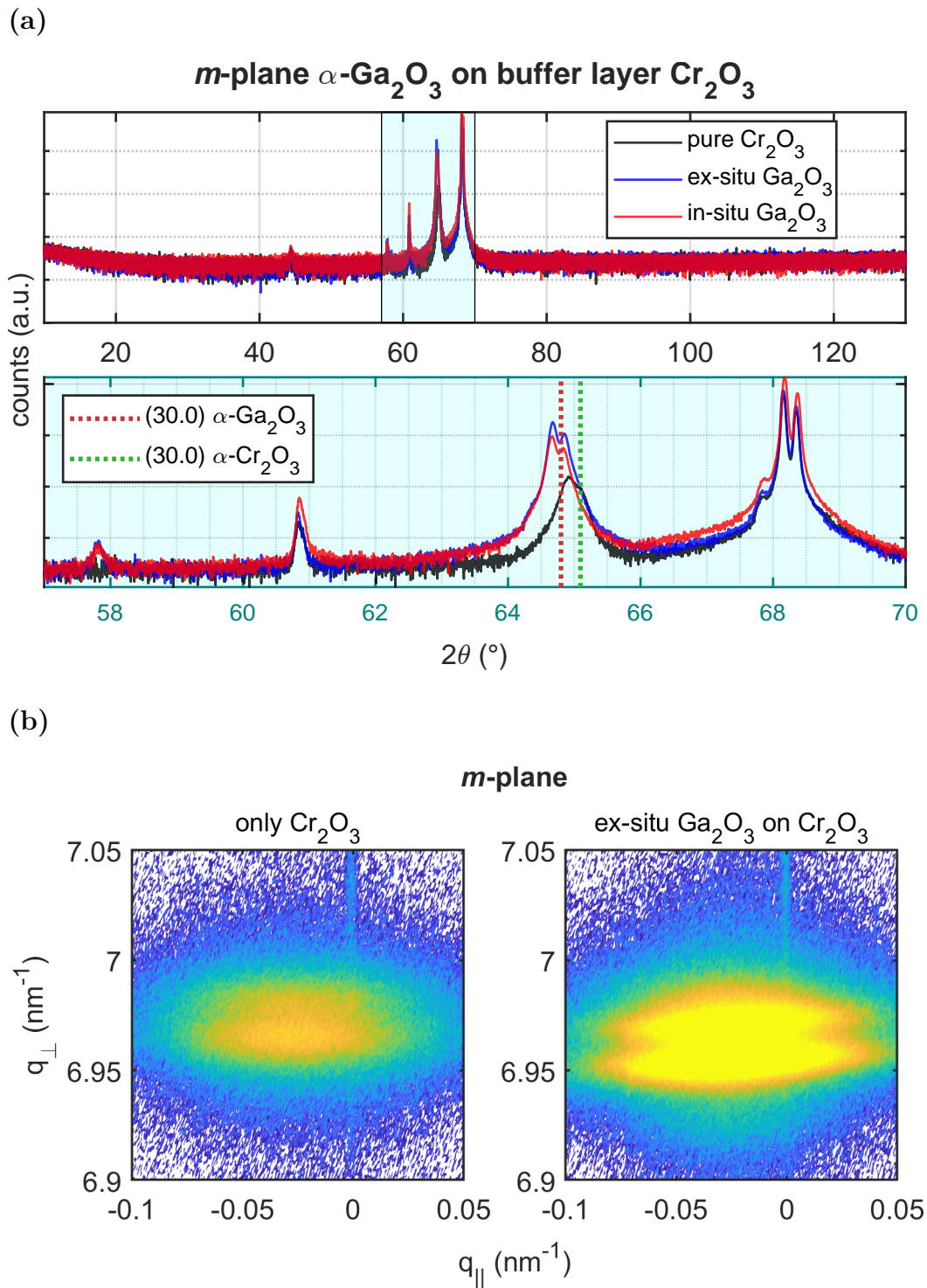


Figure 4.41: (a) $2\theta\text{-}\omega$ -patterns of the m -plane Cr_2O_3 reference sample (black), as well as the *ex situ* (blue) and *in situ* (red) buffer layer structures. The expected peak positions for the (30.0) reflection of Cr_2O_3 (green dotted) and $\alpha\text{-Ga}_2\text{O}_3$ (red dotted) are indicated. (b) RSM around the (30.0) reflection recorded before (left) and after (right) *ex situ* deposition of Ga_2O_3 on Cr_2O_3 .

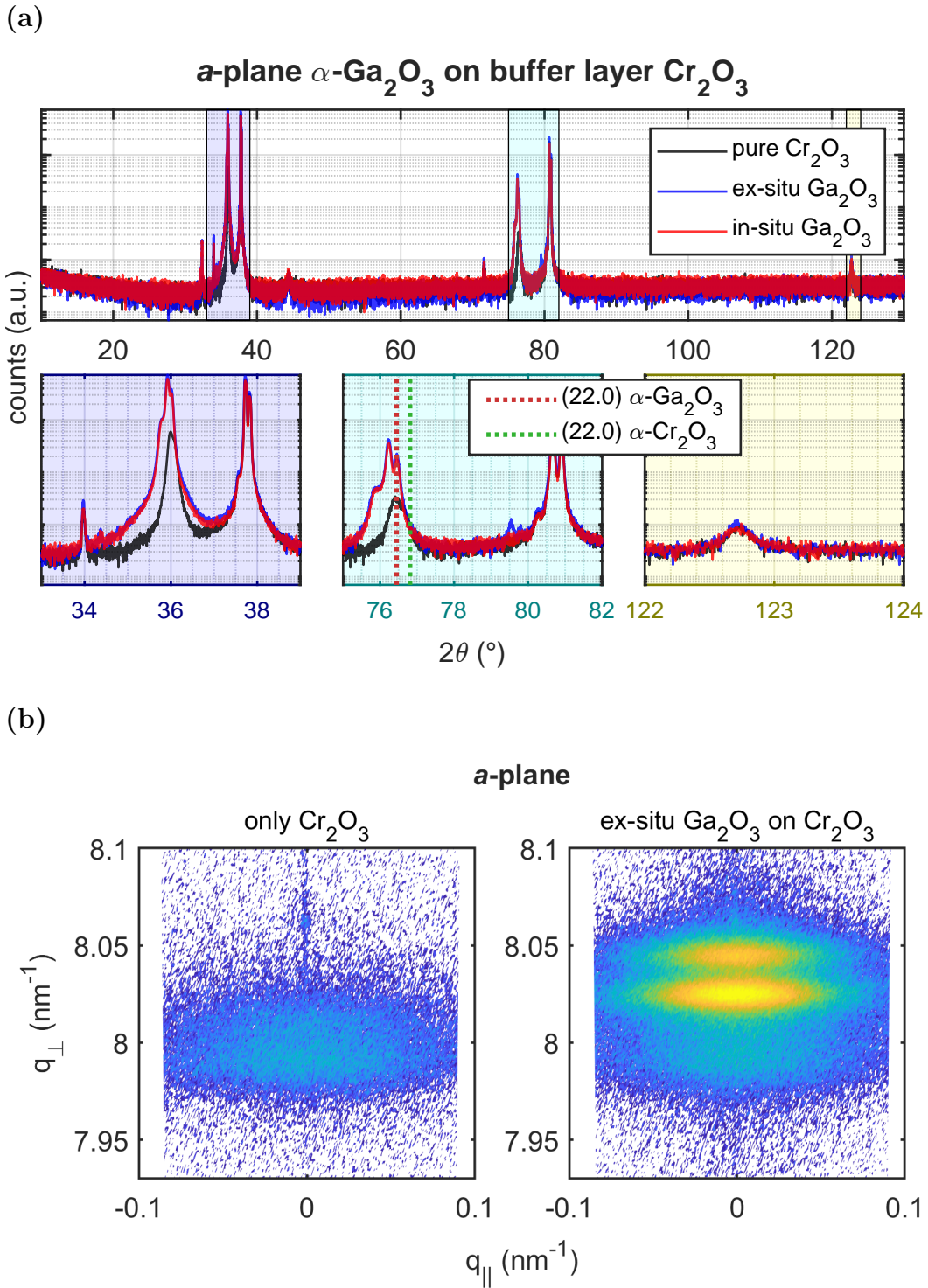
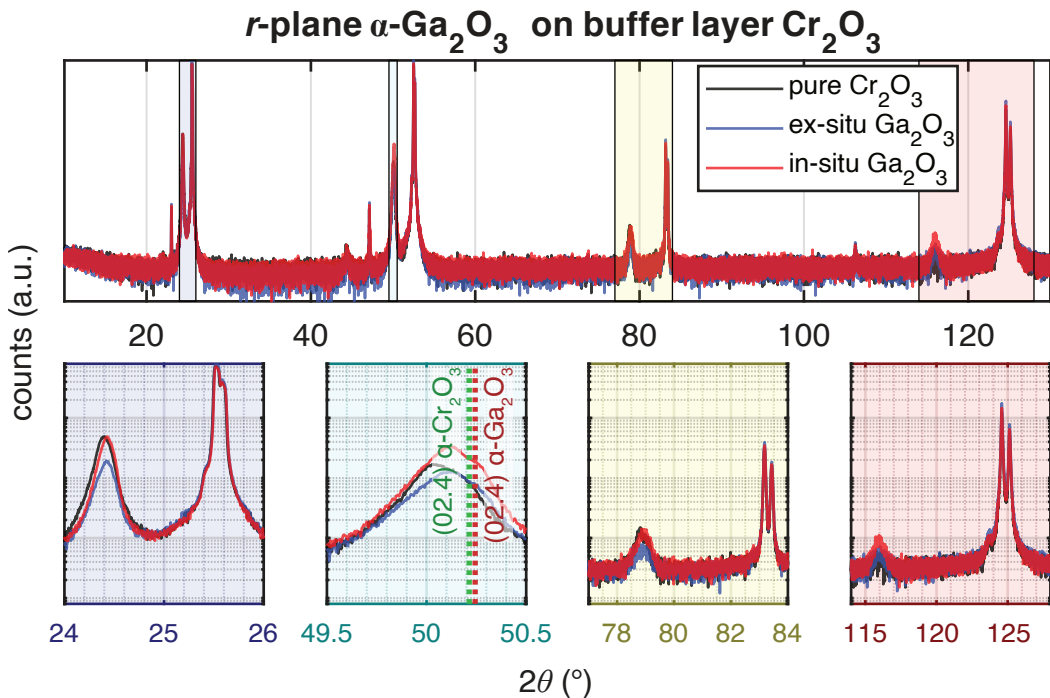


Figure 4.42: (a) $2\theta\text{-}\omega$ -patterns of the a -plane Cr_2O_3 reference sample (black), as well as the *ex situ* (blue) and *in situ* (red) buffer layer structures. The expected peak positions for the (22.0) reflection of Cr_2O_3 (green dotted) and $\alpha\text{-Ga}_2\text{O}_3$ (red dotted) are indicated. (b) RSM around the (22.0) reflection recorded before (left) and after (right) *ex situ* deposition of Ga_2O_3 on Cr_2O_3 .

(a)



(b)

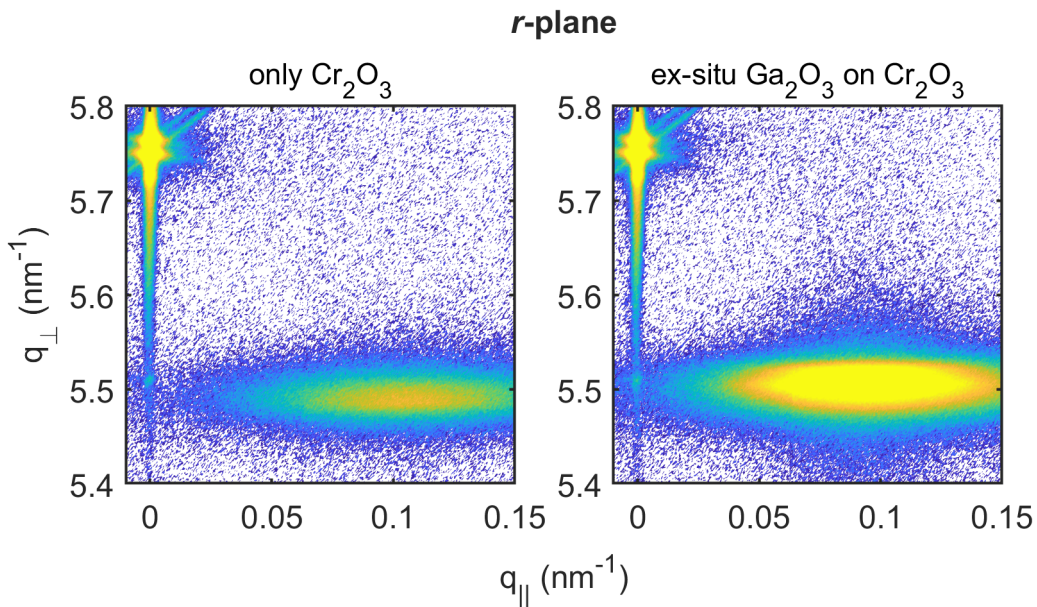


Figure 4.43: (a) $2\theta\text{-}\omega$ -patterns of the r -plane Cr_2O_3 reference sample (black), as well as the *ex situ* (blue) and *in situ* (red) buffer layer structures. The expected peak positions for the (02.4) reflection of Cr_2O_3 (green dotted) and $\alpha\text{-Ga}_2\text{O}_3$ (red dotted) are indicated. (b) RSM around the (02.4) reflection recorded before (left) and after (right) *ex situ* deposition of Ga_2O_3 on Cr_2O_3 .

usage of buffer layers can circumvent this limitation, e.g. via growth on $(\text{Al}, \text{Ga})_2\text{O}_3$ by mist-CVD [102] or on Cr_2O_3 via HVPE [17, 18]. However, no PVD method was able to deposit phase pure $\alpha\text{-Ga}_2\text{O}_3$ in *c*-orientation. By exploiting the isostructural properties of Cr_2O_3 , the phase pure deposition of $\alpha\text{-Ga}_2\text{O}_3$ in *c*-orientation could be achieved via Pulsed Laser Deposition in this work. Furthermore, the same approach works the growth of $\alpha\text{-Ga}_2\text{O}_3$ in *r*-, *m*- and *a*-orientation, which allows the deposition of $\alpha\text{-Ga}_2\text{O}_3$ on all four common sapphire orientations in one single PLD process.

Appendices

Appendix A

Calculations

In the following, Equ. 3.7 is applied:

$$d_{hkl} = \left(\frac{4}{3} \frac{h^2 + k^2 + hk}{a^2} + \frac{l^2}{c^2} \right)^{-1/2}.$$

A.1 m -plane lattice constants

The reflection $(30.\pm 6)$ is a superposition of out-of-plane (30.0) and in-plane $(00.\pm 6)$. The inverse lattice plane distances are

$$q_{\perp}^{(30.\pm 6)} = d_{(30.0)}^{-1} = \sqrt{\frac{4}{3} \frac{3^2}{a^2}} = \sqrt{12}/a, \quad (\text{A.1})$$

$$q_{\parallel}^{(30.\pm 6)} = d_{(00.\pm 6)}^{-1} = \sqrt{\frac{(\pm 6)^2}{c^2}} = 6/c. \quad (\text{A.2})$$

In the y -axis azimuth, $(4\bar{2}.0)$ is a superposition of out-of-plane (30.0) and in-plane $(1\bar{2}.0)$. Note that $(1\bar{2}.0)$ has a -plane character. The inverse lattice plane distances are

$$q_{\perp}^{(4\bar{2}.0)} = d_{(30.0)}^{-1} = \sqrt{12}/a, \quad (\text{A.3})$$

$$q_{\parallel}^{(4\bar{2}.0)} = d_{(1\bar{2}.0)}^{-1} = \sqrt{\frac{4}{3} \frac{1^2 + 2^2 - 2}{a^2}} = 2/a. \quad (\text{A.4})$$

Also in this azimuth, (22.0) is a superposition of out-of-plane (30.0) and in-plane $(\bar{1}2.0)$. The inverse lattice plane distances are

$$q_{\perp}^{(22.0)} = d_{(30.0)}^{-1} = \sqrt{12}/a, \quad (\text{A.5})$$

$$q_{\parallel}^{(22.0)} = d_{(\bar{1}2.0)}^{-1} = \sqrt{\frac{4}{3} \frac{1^2 + 2^2 - 2}{a^2}} = 2/a. \quad (\text{A.6})$$

A.2 *a*-plane lattice constants

The reflection $(22.\pm 6)$ is a superposition of out-of-plane (22.0) and in-plane $(00.\pm 6)$. The inverse lattice plane distances are

$$q_{\perp}^{(22.\pm 6)} = d_{(22.0)}^{-1} = \sqrt{\frac{4}{3} \frac{2^2 + 2^2 + 4}{a^2}} = 4/a, \quad (\text{A.7})$$

$$q_{\parallel}^{(22.\pm 6)} = d_{(00.\pm 6)}^{-1} = 6/c. \quad (\text{A.8})$$

In the y -axis azimuth, (30.0) cannot be represented as a superposition of in-plane and out-of-plane scattering vectors. This is due to the symmetry of the hexagonal lattice. But it is possible to represent it as a superposition of out-of-plane (11.0) and in-plane $(1\bar{1}.0)$, multiplied with a factor of 1.5 each. This leads to the calculation of inverse lattice planes via

$$q_{\perp}^{(30.0)} = \frac{3}{2} \cdot d_{1\bar{1}.0}^{-1} = \frac{3}{2} \sqrt{\frac{4}{3} \frac{1^2 + 1^2 - 1}{a^2}} = \frac{3}{2} \cdot \frac{2}{\sqrt{3}}/a = \sqrt{3}/a, \quad (\text{A.9})$$

$$q_{\parallel}^{(30.0)} = \frac{3}{2} \cdot d_{11.0}^{-1} = \frac{3}{2} \sqrt{\frac{4}{3} \frac{1^2 + 1^2 + 1}{a^2}} = \frac{3}{2} \cdot 2/a = 3/a. \quad (\text{A.10})$$

The same holds for the (03.0) reflection: it is a superposition of $(\bar{1}1.0)$ and (11.0) , multiplied by a factor of 1.5 and one obtains:

$$q_{\perp}^{(03.0)} = \frac{3}{2} \cdot d_{\bar{1}1.0}^{-1} = \sqrt{3}/a, \quad (\text{A.11})$$

$$q_{\parallel}^{(03.0)} = \frac{3}{2} \cdot d_{11.0}^{-1} = 3/a. \quad (\text{A.12})$$

Appendix B

Figures

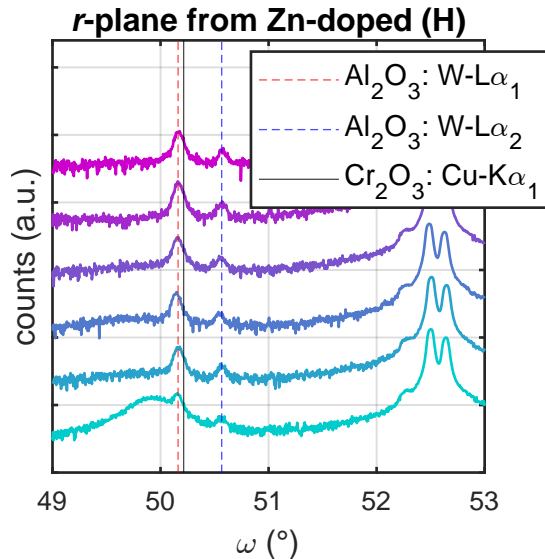


Figure B.1: 2θ - ω patterns of *r*-plane oriented samples fabricated from the Zn-doped (high) target. No Cr_2O_3 peaks at the predicted (02.4) position can be observed. Those peaks that are present belong to the (02.4) reflection of the substrate (tungsten L α_1 and L α_2 radiation).

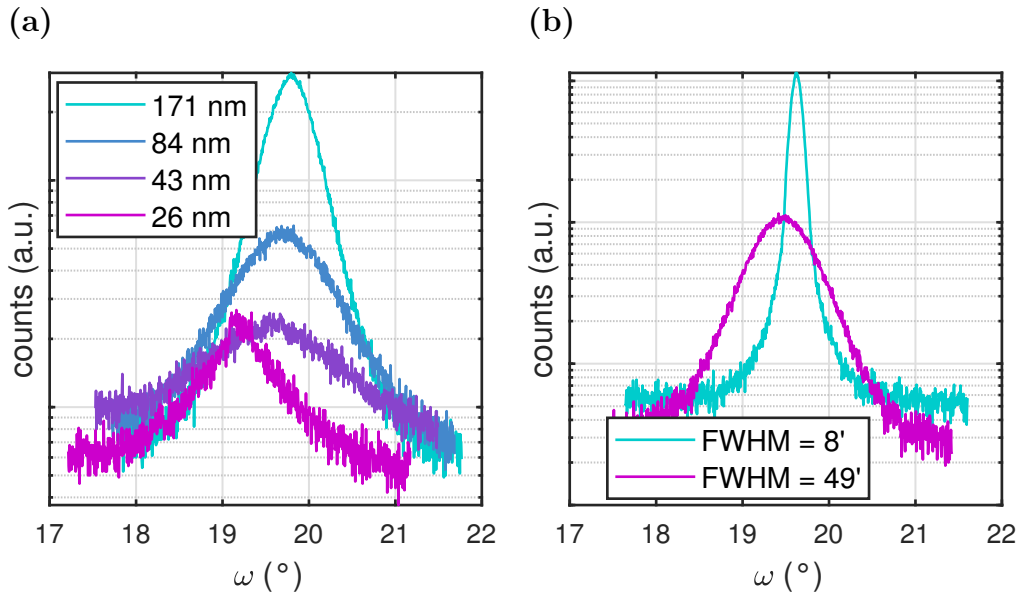


Figure B.2: (a) ω -patterns for c -plane oriented samples of the 1st batch in 4.3, fabricated with smallest laser spot size. (b) ω -patterns for two c -plane oriented samples from the 2nd batch in 4.3, that were fabricated with same fluence and had the same thickness of approx. 150 nm, but very different ω -FWHM.

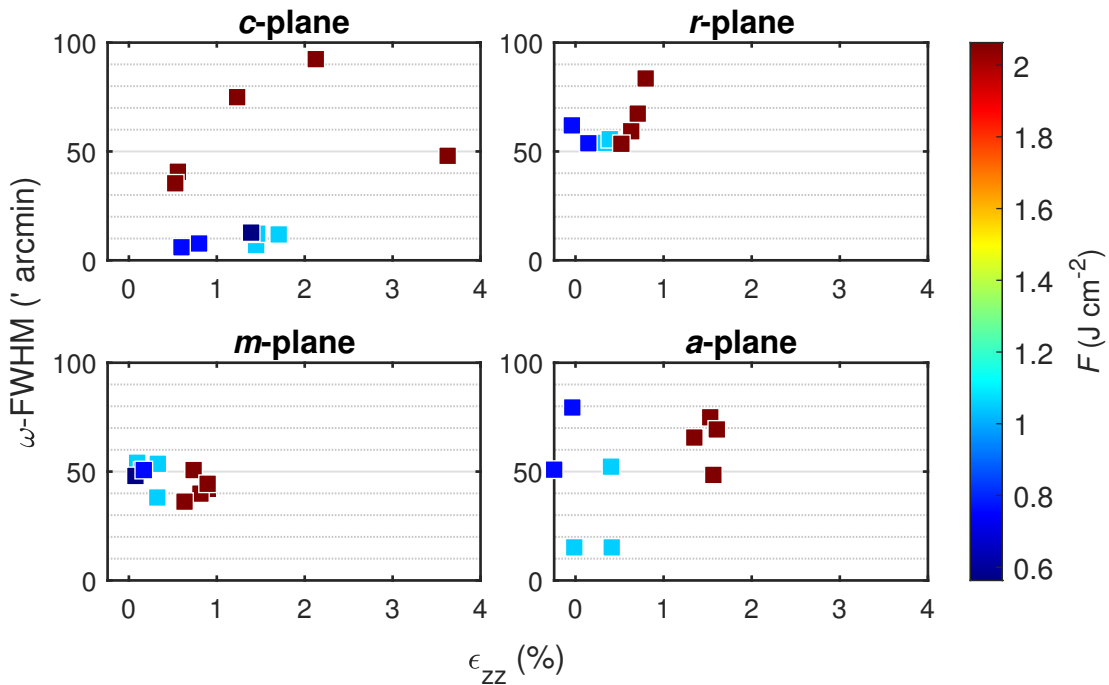


Figure B.3: Correlation between strain and ω -FWHM for all samples fabricated with a laser pulse energy of 650 mJ but varying laser spot size, depending on thickness and laser fluence (false color).

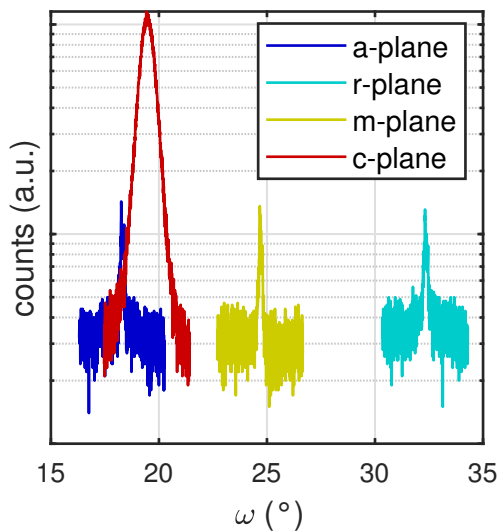


Figure B.4: ω -patterns for the samples of the process that yielded the c -plane sample with higher FWHM in Fig. B.2b. The patterns correspond to c - (red), r (cyan), m (yellow) and a -plane (blue).

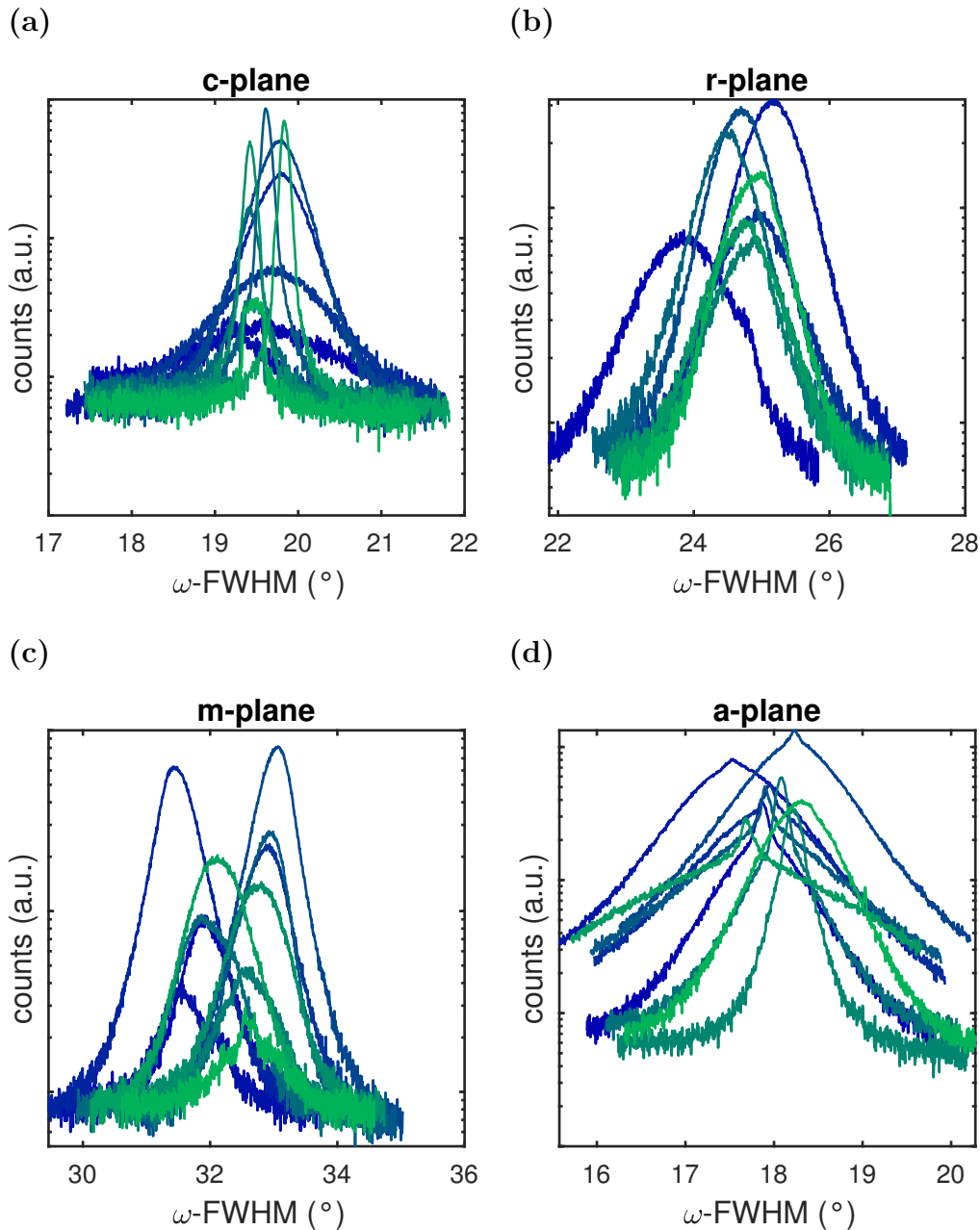


Figure B.5: Diffractogramms from ω -patterns for varying laser focus in 4.3.

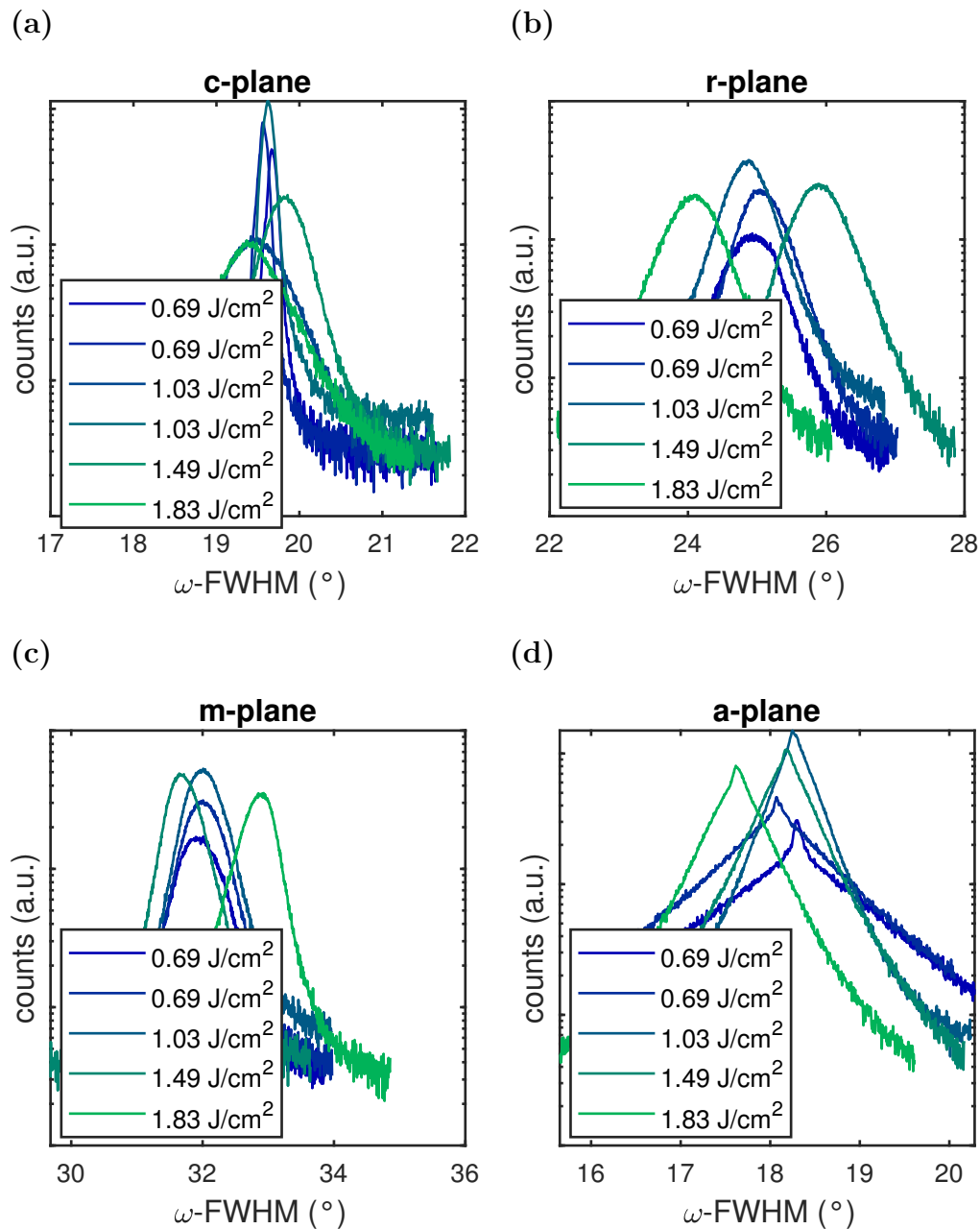


Figure B.6: Diffractogramms from ω -patterns for varying laser pulse energy in 4.3.

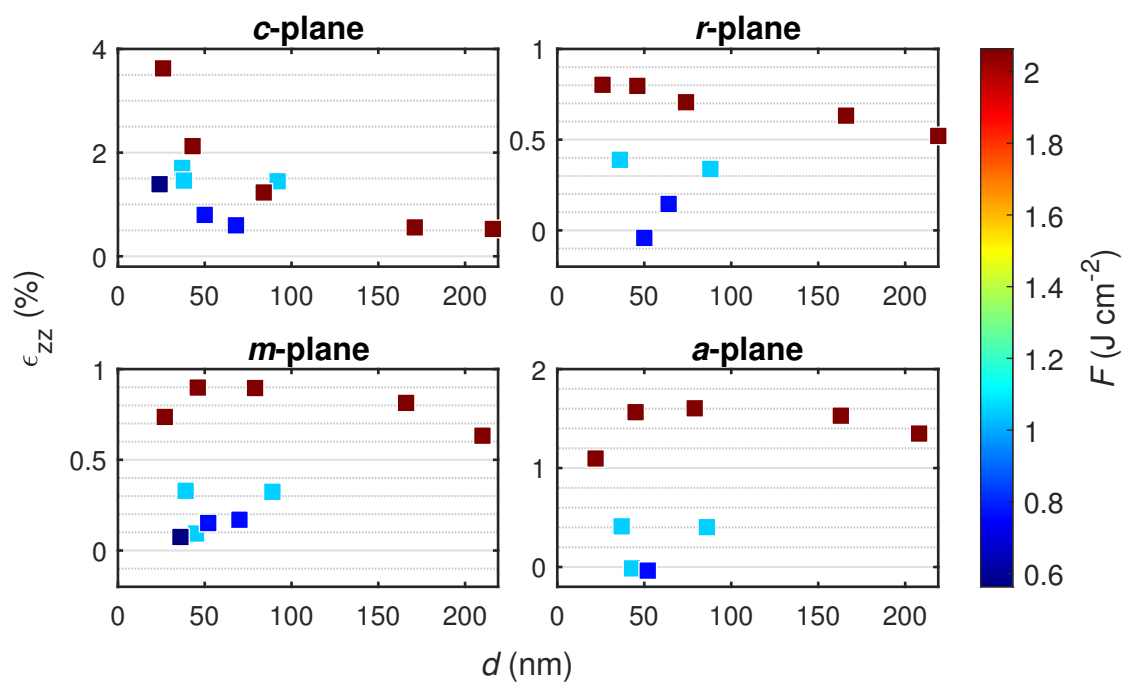


Figure B.7: Detailed view (cf. Fig. 4.23) of the o.o.p. strain for the samples of the 1st batch in 4.3.

Bibliography

- [1] Masataka Higashiwaki and Gregg H. Jessen. “Guest Editorial: The dawn of gallium oxide microelectronics”. In: *Applied Physics Letters* 112.6 (2018), p. 060401. ISSN: 0003-6951, 1077-3118. DOI: [10.1063/1.5017845](https://doi.org/10.1063/1.5017845).
- [2] Oleksiy Slobodyan *et al.* “Analysis of the dependence of critical electric field on semiconductor bandgap”. In: *Journal of Materials Research* 37.4 (2022), pp. 849–865. ISSN: 0884-2914, 2044-5326. DOI: [10.1557/s43578-021-00465-2](https://doi.org/10.1557/s43578-021-00465-2).
- [3] Geetak Gupta and Elaheh Ahmadi. “(Ultra)wide-bandgap semiconductors for electric vehicles”. In: *MRS Bulletin* 49.7 (2024), pp. 730–737. ISSN: 0883-7694, 1938-1425. DOI: [10.1557/s43577-024-00750-5](https://doi.org/10.1557/s43577-024-00750-5).
- [4] Anamika Singh Pratiyush *et al.* “High responsivity in molecular beam epitaxy grown β -Ga₂O₃ metal semiconductor metal solar blind deep-UV photodetector”. In: *Applied Physics Letters* 110.22 (2017), p. 221107. ISSN: 0003-6951, 1077-3118. DOI: [10.1063/1.4984904](https://doi.org/10.1063/1.4984904).
- [5] Jiancheng Yang *et al.* “High reverse breakdown voltage Schottky rectifiers without edge termination on Ga₂O₃”. In: *Applied Physics Letters* 110.19 (2017), p. 192101. ISSN: 0003-6951, 1077-3118. DOI: [10.1063/1.4983203](https://doi.org/10.1063/1.4983203).
- [6] Neil Moser *et al.* “Ge-Doped β -Ga₂O₃ MOSFETs”. In: *IEEE Electron Device Letters* 38.6 (2017), pp. 775–778. ISSN: 0741-3106, 1558-0563. DOI: [10.1109/LED.2017.2697359](https://doi.org/10.1109/LED.2017.2697359).
- [7] M Ogita *et al.* “Ga₂O₃ thin film for oxygen sensor at high temperature”. In: *Applied Surface Science* 175–176 (2001), pp. 721–725. ISSN: 01694332. DOI: [10.1016/S0169-4332\(01\)00080-0](https://doi.org/10.1016/S0169-4332(01)00080-0).
- [8] Anna Hassa, Marius Grundmann, and Holger Von Wenckstern. “Progression of group-III sesquioxides: epitaxy, solubility and desorption”. In: *Journal of Physics D: Applied Physics* 54.22 (2021), p. 223001. ISSN: 0022-3727, 1361-6463. DOI: [10.1088/1361-6463/abd4a4](https://doi.org/10.1088/1361-6463/abd4a4).
- [9] Kentaro Kaneko *et al.* “Evaluation of misfit relaxation in α -Ga₂O₃ epitaxial growth on α -Al₂O₃ substrate”. In: *Japanese Journal of Applied Physics* 51 (2R 2012), p. 020201. ISSN: 0021-4922, 1347-4065. DOI: [10.1143/JJAP.51.020201](https://doi.org/10.1143/JJAP.51.020201).

- [10] Hitoshi Takane *et al.* “Effect of dislocations and impurities on carrier transport in α -Ga₂O₃ on m-plane sapphire substrate”. In: *Journal of Materials Research* 38.10 (2023), pp. 2645–2654. ISSN: 0884-2914, 2044-5326. DOI: [10.1557/s43578-023-01015-8](https://doi.org/10.1557/s43578-023-01015-8).
- [11] M. Bosi *et al.* “Ga₂O₃ polymorphs: tailoring the epitaxial growth conditions”. In: *Journal of Materials Chemistry C* 8.32 (2020), pp. 10975–10992. ISSN: 2050-7526, 2050-7534. DOI: [10.1039/DOTC02743J](https://doi.org/10.1039/DOTC02743J).
- [12] Katsuaki Kawara *et al.* “Elimination of threading dislocations in α -Ga₂O₃ by double-layered epitaxial lateral overgrowth”. In: *Applied Physics Express* 13.7 (2020), p. 075507. ISSN: 1882-0778, 1882-0786. DOI: [10.35848/1882-0786/ab9fc5](https://doi.org/10.35848/1882-0786/ab9fc5).
- [13] V. I. Nikolaev *et al.* “Thick Epitaxial α -Ga₂O₃:Sn Layers on a Patterned Sapphire Substrate”. In: *Technical Physics Letters* 46.3 (2020), pp. 228–230. ISSN: 1063-7850, 1090-6533. DOI: [10.1134/S106378502003013X](https://doi.org/10.1134/S106378502003013X).
- [14] Riena Jinno *et al.* “Reduction in edge dislocation density in corundum-structured α -Ga₂O₃ layers on sapphire substrates with quasi-graded α -(Al,Ga)₂O₃ buffer layers”. In: *Applied Physics Express* 9.7 (2016), p. 071101. ISSN: 1882-0778, 1882-0786. DOI: [10.7567/APEX.9.071101](https://doi.org/10.7567/APEX.9.071101).
- [15] Riena Jinno *et al.* “Control of Crystal Structure of Ga₂O₃ on Sapphire Substrate by Introduction of α -(Al_xGa_{1-x})₂O₃ Buffer Layer”. In: *physica status solidi (b)* 255.4 (2018), p. 1700326. ISSN: 0370-1972, 1521-3951. DOI: [10.1002/pssb.201700326](https://doi.org/10.1002/pssb.201700326).
- [16] S.I. Stepanov *et al.* “HVPE growth of corundum-structured α -Ga₂O₃ on sapphire substrates with α -Cr₂O₃ buffer layer”. In: *Materials Physics and Mechanics* 47 (2021), pp. 577–581. DOI: [10.18149/MPM.4742021_4](https://doi.org/10.18149/MPM.4742021_4).
- [17] Alexander Polyakov *et al.* “Effects of sapphire substrate orientation on Sn-doped α -Ga₂O₃ grown by halide vapor phase epitaxy using α -Cr₂O₃ buffers”. In: *Journal of Physics D: Applied Physics* 55.49 (2022), p. 495102. ISSN: 0022-3727, 1361-6463. DOI: [10.1088/1361-6463/ac962f](https://doi.org/10.1088/1361-6463/ac962f).
- [18] Alexander Polyakov *et al.* “Electrical properties of α -Ga₂O₃ films grown by halide vapor phase epitaxy on sapphire with α -Cr₂O₃ buffers”. In: *Journal of Applied Physics* 131.21 (2022), p. 215701. ISSN: 0021-8979, 1089-7550. DOI: [10.1063/5.0090832](https://doi.org/10.1063/5.0090832).
- [19] Pavel N. Butenko *et al.* “Fabrication of α -Ga₂O₃:Sn/ α -Cr₂O₃/ α -Al₂O₃ heterostructure by mist CVD and HVPE”. In: *Condensed Matter and Interphases* 25.4 (2023), pp. 542–547. ISSN: 2687-0711. DOI: [10.17308/kcmf.2023.25/11476](https://doi.org/10.17308/kcmf.2023.25/11476).

- [20] Riena Jinno, Kentaro Kaneko, and Shizuo Fujita. “Thermal stability of α -Ga₂O₃ films grown on c-plane sapphire substrates via mist-CVD”. In: *AIP Advances* 10.11 (2020), p. 115013. ISSN: 2158-3226. DOI: [10.1063/5.0020464](https://doi.org/10.1063/5.0020464).
- [21] E. Arca, K. Fleischer, and I. V. Shvets. “Magnesium, nitrogen codoped Cr₂O₃: A p-type transparent conducting oxide”. In: *Applied Physics Letters* 99.11 (2011), p. 111910. ISSN: 0003-6951. DOI: [10.1063/1.3638461](https://doi.org/10.1063/1.3638461).
- [22] Elisabetta Arca *et al.* “Effect of Chemical Precursors On the Optical and Electrical Properties of p-Type Transparent Conducting Cr₂O₃:(Mg,N)”. In: *The Journal of Physical Chemistry C* 117.42 (2013), pp. 21901–21907. ISSN: 1932-7447. DOI: [10.1021/jp404230k](https://doi.org/10.1021/jp404230k).
- [23] Elisabetta Arca *et al.* “Valence band modification of Cr₂O₃ by Ni-doping: creating a high figure of merit p-type TCO”. In: *Journal of Materials Chemistry C* 5.47 (2017), pp. 12610–12618. ISSN: 2050-7534. DOI: [10.1039/C7TC03545D](https://doi.org/10.1039/C7TC03545D).
- [24] L. Farrell *et al.* “Conducting mechanism in the epitaxial p-type transparent conducting oxide Cr₂O₃:Mg”. In: *Physical Review B* 91.12 (2015), p. 125202. ISSN: 1098-0121, 1550-235X. DOI: [10.1103/PhysRevB.91.125202](https://doi.org/10.1103/PhysRevB.91.125202).
- [25] S. J. Pearton *et al.* “A review of Ga₂O₃ materials, processing, and devices”. In: *Applied Physics Reviews* 5.1 (2018), p. 011301. ISSN: 1931-9401. DOI: [10.1063/1.5006941](https://doi.org/10.1063/1.5006941).
- [26] Kentaro Kaneko *et al.* “Ultra-wide bandgap corundum-structured p-type α -(Ir,Ga)₂O₃ alloys for α -Ga₂O₃ electronics”. In: *Applied Physics Letters* 118.10 (2021), p. 102104. ISSN: 0003-6951, 1077-3118. DOI: [10.1063/5.0027297](https://doi.org/10.1063/5.0027297).
- [27] Clemens Petersen *et al.* “PLD of α -Ga₂O₃ on m-plane Al₂O₃: Growth regime, growth process, and structural properties”. In: *APL Materials* 11.6 (2023), p. 061122. ISSN: 2166-532X. DOI: [10.1063/5.0149797](https://doi.org/10.1063/5.0149797).
- [28] Sofie Vogt *et al.* “Realization of Conductive n-Type Doped α -Ga₂O₃ on m-Plane Sapphire Grown by a Two-Step Pulsed Laser Deposition Process”. In: *physica status solidi (a)* 220.3 (2023), p. 2200721. ISSN: 1862-6300, 1862-6319. DOI: [10.1002/pssa.202200721](https://doi.org/10.1002/pssa.202200721).
- [29] Sofie Vogt *et al.* “Zr doping in pulsed-laser-deposited α -Ga₂O₃ for device applications”. In: *Physical Review Applied* 21.6 (2024), p. 064016. ISSN: 2331-7019. DOI: [10.1103/PhysRevApplied.21.064016](https://doi.org/10.1103/PhysRevApplied.21.064016).
- [30] David S. Ginley, ed. *Handbook of Transparent Conductors*. Boston, MA: Springer US, 2011. ISBN: 978-1-4419-1637-2 978-1-4419-1638-9. DOI: [10.1007/978-1-4419-1638-9](https://doi.org/10.1007/978-1-4419-1638-9).
- [31] C. Guillén and J. Herrero. “TCO/metal/TCO structures for energy and flexible electronics”. In: *Thin Solid Films* 520.1 (2011), pp. 1–17. ISSN: 00406090. DOI: [10.1016/j.tsf.2011.06.091](https://doi.org/10.1016/j.tsf.2011.06.091).

- [32] Harpreet Singh and Bharpur Singh. “A brief study of novel transparent conducting oxide (TCO) material”. In: 14th international conference on materials processing and characterization 2023. Hyderabad, India, 2024, p. 030164. DOI: [10.1063/5.0197252](https://doi.org/10.1063/5.0197252).
- [33] Ganesh T. Chavan *et al.* “A Brief Review of Transparent Conducting Oxides (TCO): The Influence of Different Deposition Techniques on the Efficiency of Solar Cells”. In: *Nanomaterials* 13.7 (2023), p. 1226. ISSN: 2079-4991. DOI: [10.3390/nano13071226](https://doi.org/10.3390/nano13071226).
- [34] Chiara Cadelise, Jamie F. Speirs, and Robert J.K. Gross. “Materials availability for thin film (TF) PV technologies development: A real concern?” In: *Renewable and Sustainable Energy Reviews* 15.9 (2011), pp. 4972–4981. ISSN: 13640321. DOI: [10.1016/j.rser.2011.06.012](https://doi.org/10.1016/j.rser.2011.06.012).
- [35] Man Hoi Wong *et al.* “Ultrawide-bandgap semiconductors: An overview”. In: *Journal of Materials Research* 36.23 (2021), pp. 4601–4615. ISSN: 0884-2914, 2044-5326. DOI: [10.1557/s43578-021-00458-1](https://doi.org/10.1557/s43578-021-00458-1).
- [36] Kentaro Kaneko, Taichi Nomura, and Shizuo Fujita. “Corundum-structured α -phase $\text{Ga}_2\text{O}_3\text{-Cr}_2\text{O}_3\text{-Fe}_2\text{O}_3$ alloy system for novel functions”. In: *Phys. Status Solidi C* 7.10 (2010), pp. 2467–2470. ISSN: 1610-1642. DOI: [10.1002/pssc.200983896](https://doi.org/10.1002/pssc.200983896).
- [37] N. Uekawa and K. Kaneko. “Dopant Reduction in *p*-Type Oxide Films upon Oxygen Absorption”. In: *The Journal of Physical Chemistry* 100.10 (1996), pp. 4193–4198. ISSN: 0022-3654, 1541-5740. DOI: [10.1021/jp952784m](https://doi.org/10.1021/jp952784m).
- [38] P. S. Robbert *et al.* “Novel electronic and magnetic properties of ultrathin chromium oxide films grown on Pt(111)”. In: *Journal of Vacuum Science & Technology A: Vacuum, Surfaces, and Films* 16.3 (1998), pp. 990–995. ISSN: 0734-2101, 1520-8559. DOI: [10.1116/1.581283](https://doi.org/10.1116/1.581283).
- [39] M.F. Al-Kuhaili and S.M.A. Durrani. “Optical properties of chromium oxide thin films deposited by electron-beam evaporation”. In: *Optical Materials* 29.6 (2007), pp. 709–713. ISSN: 09253467. DOI: [10.1016/j.optmat.2005.11.020](https://doi.org/10.1016/j.optmat.2005.11.020).
- [40] François Lebreau *et al.* “Structural, Magnetic, Electronic, Defect, and Diffusion Properties of Cr_2O_3 : A DFT+*U* Study”. In: *The Journal of Physical Chemistry C* 118.31 (2014), pp. 18133–18145. ISSN: 1932-7447. DOI: [10.1021/jp5039943](https://doi.org/10.1021/jp5039943).
- [41] Zhishan Mi *et al.* “The effects of strain and vacancy defects on the electronic structure of Cr_2O_3 ”. In: *Computational Materials Science* 144 (2018), pp. 64–69. ISSN: 09270256. DOI: [10.1016/j.commatsci.2017.12.012](https://doi.org/10.1016/j.commatsci.2017.12.012).
- [42] James F. Shackelford and William Alexander, eds. *Crc materials science and engineering handbook*. 0th ed. CRC Press, 2000. URL: <https://doi.org/10.1201/9781420038408>.

- [43] F. D. Lai *et al.* “Ultrathin TiO₂ amorphous films for high transmittance APSM blanks at 157 and 193 nm wavelength simultaneously”. In: *Journal of Vacuum Science & Technology B: Microelectronics and Nanometer Structures Processing, Measurement, and Phenomena* 21.6 (2003), pp. 3062–3066. ISSN: 1071-1023, 1520-8567. DOI: [10.1116/1.1624252](https://doi.org/10.1116/1.1624252).
- [44] Jun C. Nable, Steven L. Suib, and Francis S. Galasso. “Metal organic chemical vapor deposition of Al₂O₃ and Cr₂O₃ on nickel as oxidation barriers”. In: *Surface and Coatings Technology* 186.3 (2004), pp. 423–430. ISSN: 02578972. DOI: [10.1016/j.surfcoat.2003.11.022](https://doi.org/10.1016/j.surfcoat.2003.11.022).
- [45] Chun-Shen Cheng, H. Gomi, and H. Sakata. “Electrical and Optical Properties of Cr₂O₃ Films Prepared by Chemical Vapour Deposition”. In: *Physica Status Solidi (a)* 155.2 (1996), pp. 417–425. ISSN: 00318965, 1521396X. DOI: [10.1002/pssa.2211550215](https://doi.org/10.1002/pssa.2211550215).
- [46] Cecilia Guillén and José Herrero. “Structural Changes Induced by Heating in Sputtered NiO and Cr₂O₃ Thin Films as *p*-Type Transparent Conductive Electrodes”. In: *Electronic Materials* 2.2 (2021), pp. 49–59. ISSN: 2673-3978. DOI: [10.3390/electronicmat2020005](https://doi.org/10.3390/electronicmat2020005).
- [47] Koichi Momma and Fujio Izumi. “VESTA 3 for three-dimensional visualization of crystal, volumetric and morphology data”. In: *Journal of Applied Crystallography* 44.6 (2011), pp. 1272–1276. ISSN: 0021-8898. DOI: [10.1107/S0021889811038970](https://doi.org/10.1107/S0021889811038970).
- [48] M. Catti *et al.* “Electronic, magnetic and crystal structure of Cr₂O₃ by theoretical methods”. In: *Journal of Physics and Chemistry of Solids* 57.11 (1996), pp. 1735–1741. ISSN: 00223697. DOI: [10.1016/0022-3697\(96\)00034-0](https://doi.org/10.1016/0022-3697(96)00034-0).
- [49] Aoife B Kehoe *et al.* “Assessing the potential of Mg-doped Cr₂O₃ as a novel *p*-type transparent conducting oxide”. In: *Journal of Physics: Condensed Matter* 28.12 (2016), p. 125501. ISSN: 0953-8984, 1361-648X. DOI: [10.1088/0953-8984/28/12/125501](https://doi.org/10.1088/0953-8984/28/12/125501).
- [50] Larry W. Finger and Robert M. Hazen. “Crystal structure and isothermal compression of Fe₂O₃, Cr₂O₃, and V₂O₃ to 50 kbars”. In: *Journal of Applied Physics* 51.10 (1980), pp. 5362–5367. ISSN: 0021-8979, 1089-7550. DOI: [10.1063/1.327451](https://doi.org/10.1063/1.327451).
- [51] Valerian Pishchik, Leonid A. Lytvynov, and Elena R. Dobrovinskaya. *Sapphire: Material, Manufacturing, Applications*. Boston, MA: Springer US, 2009. ISBN: 978-0-387-85694-0 978-0-387-85695-7. DOI: [10.1007/978-0-387-85695-7](https://doi.org/10.1007/978-0-387-85695-7).
- [52] M. Marezio and J. P. Remeika. “Bond lengths in the α -Ga₂O₃ structure and the high-pressure phase of Ga_{2-x}Fe_xO₃”. In: *The Journal of Chemical Physics* 46.5 (1967), pp. 1862–1865. ISSN: 0021-9606, 1089-7690. DOI: [10.1063/1.1840945](https://doi.org/10.1063/1.1840945).

- [53] R. W. G. Wyckoff. *Crystal structures*. New York, London, Sydney: Interscience Publishers, 1963. 467 pp.
- [54] Ruihua Cheng, C.N. Borca, and P.A. Dowben. “Selective Area Chemical Vapor Deposition of Chromium Oxides”. In: *MRS Proceedings* 614 (2000), F10.4.1. ISSN: 0272-9172, 1946-4274. DOI: [10.1557/PROC-614-F10.4.1](https://doi.org/10.1557/PROC-614-F10.4.1).
- [55] Ruihua Cheng *et al.* “Potential phase control of chromium oxide thin films prepared by laser-initiated organometallic chemical vapor deposition”. In: *Applied Physics Letters* 78.4 (2001), pp. 521–523. ISSN: 0003-6951, 1077-3118. DOI: [10.1063/1.1343846](https://doi.org/10.1063/1.1343846).
- [56] Anna Caricato *et al.* “Deposition of chromium oxide thin films with large thermoelectromotive force coefficient by reactive pulsed laser ablation”. In: *Journal of Optoelectronics and Advanced Materials* 12 (2010), p. 427.
- [57] Sandhyarani Punugupati, Jagdish Narayan, and Frank Hunte. “Room temperature ferromagnetism in epitaxial Cr₂O₃ thin films grown on r-sapphire”. In: *Journal of Applied Physics* 117.19 (2015), p. 193907. ISSN: 0021-8979, 1089-7550. DOI: [10.1063/1.4921435](https://doi.org/10.1063/1.4921435).
- [58] Jarnail Singh *et al.* “Structural, optical and electrical characterization of epitaxial Cr₂O₃ thin film deposited by PLD”. In: *Materials Research Express* 6.10 (2019), p. 106406. ISSN: 2053-1591. DOI: [10.1088/2053-1591/ab3543](https://doi.org/10.1088/2053-1591/ab3543).
- [59] M. Tabbal *et al.* “Pulsed laser deposition of nanostructured dichromium trioxide thin films”. In: *Thin Solid Films* 515.4 (2006), pp. 1976–1984. ISSN: 00406090. DOI: [10.1016/j.tsf.2006.08.010](https://doi.org/10.1016/j.tsf.2006.08.010).
- [60] P. Kofstad and K. P. Lillerud. “On High Temperature Oxidation of Chromium: II . Properties of and the Oxidation Mechanism of Chromium”. In: *Journal of The Electrochemical Society* 127.11 (1980), pp. 2410–2419. ISSN: 0013-4651, 1945-7111. DOI: [10.1149/1.2129481](https://doi.org/10.1149/1.2129481).
- [61] W. C. Hagel. “Electrical Conductivity of Li-Substituted Cr₂O₃”. In: *Journal of Applied Physics* 36.8 (1965), pp. 2586–2587. ISSN: 0021-8979, 1089-7550. DOI: [10.1063/1.1714536](https://doi.org/10.1063/1.1714536).
- [62] G. M. Crosbie *et al.* “Electronically Conducting Doped Chromium Oxides”. In: *Journal of the American Ceramic Society* 67.7 (1984), pp. 498–503. ISSN: 0002-7820, 1551-2916. DOI: [10.1111/j.1151-2916.1984.tb19642.x](https://doi.org/10.1111/j.1151-2916.1984.tb19642.x).
- [63] A Holt and P Kofstad. “Electrical conductivity and defect structure of Cr₂O₃. II. Reduced temperatures (<~1000 °C)”. In: *Solid State Ionics* 69.2 (1994), pp. 137–143. ISSN: 01672738. DOI: [10.1016/0167-2738\(94\)90402-2](https://doi.org/10.1016/0167-2738(94)90402-2).
- [64] Robert Schewski *et al.* “Epitaxial stabilization of pseudomorphic α-Ga₂O₃ on sapphire (0001)”. In: *Applied Physics Express* 8.1 (2015), p. 011101. ISSN: 1882-0778, 1882-0786. DOI: [10.7567/APEX.8.011101](https://doi.org/10.7567/APEX.8.011101).

- [65] Kentaro Kaneko *et al.* “Progress in α -Ga₂O₃ for practical device applications”. In: *Japanese Journal of Applied Physics* 62 (SF 2023), SF0803. ISSN: 0021-4922, 1347-4065. DOI: [10.35848/1347-4065/acd125](https://doi.org/10.35848/1347-4065/acd125).
- [66] Duyoung Yang *et al.* “Epitaxial growth of alpha gallium oxide thin films on sapphire substrates for electronic and optoelectronic devices: progress and perspective”. In: *Electronic Materials Letters* 18.2 (2022), pp. 113–128. ISSN: 1738-8090, 2093-6788. DOI: [10.1007/s13391-021-00333-5](https://doi.org/10.1007/s13391-021-00333-5).
- [67] Riena Jinno *et al.* “Crystal orientation dictated epitaxy of ultrawide-bandgap 5.4- to 8.6-eV α -(AlGa)₂O₃ on m-plane sapphire”. In: *Science Advances* 7.2 (2021), eabd5891. ISSN: 2375-2548. DOI: [10.1126/sciadv.abd5891](https://doi.org/10.1126/sciadv.abd5891).
- [68] Kazuaki Akaiwa *et al.* “Electrical properties of Sn-doped α -Ga₂O₃ films on m-plane sapphire substrates grown by mist chemical vapor deposition”. In: *physica status solidi (a)* 217.3 (2020), p. 1900632. ISSN: 1862-6300, 1862-6319. DOI: [10.1002/pssa.201900632](https://doi.org/10.1002/pssa.201900632).
- [69] Anna Hassa *et al.* “Control of phase formation of (Al_xGa_{1-x})₂O₃ thin films on c-plane Al₂O₃”. In: *Journal of Physics D: Applied Physics* 53.48 (2020), p. 485105. ISSN: 0022-3727, 1361-6463. DOI: [10.1088/1361-6463/abaf7d](https://doi.org/10.1088/1361-6463/abaf7d).
- [70] Neil W. Ashcroft and N. David Mermin. *Solid State Physics*. Saunders College Publishing, 1976. 826 pp.
- [71] Marius Grundmann and Michael Lorenz. “Azimuthal anisotropy of rhombohedral (corundum phase) heterostructures”. In: *physica status solidi (b)* 258.7 (2021), p. 2100104. ISSN: 1521-3951. DOI: [10.1002/pssb.202100104](https://doi.org/10.1002/pssb.202100104).
- [72] George F. Harrington and José Santiso. “Back-to-Basics tutorial: X-ray diffraction of thin films”. In: *Journal of Electroceramics* 47.4 (2021), pp. 141–163. ISSN: 1385-3449, 1573-8663. DOI: [10.1007/s10832-021-00263-6](https://doi.org/10.1007/s10832-021-00263-6).
- [73] Lothar Spieß, ed. *Moderne Röntgenbeugung: Röntgendiffraktometrie für Materialwissenschaftler, Physiker und Chemiker*. 2., überarb. und erw. Aufl. Studium. Wiesbaden: Vieweg + Teubner, 2009. 564 pp. ISBN: 978-3-8351-0166-1.
- [74] L. D. Landau and E. M. Lifshitz. *Theory of Elasticity*. Course of Theoretical Physics vol. 7. Pergamon Press Ltd., 1970. 165 pp. ISBN: 978-0-08-057069-3.
- [75] Marius Grundmann. “Elastic theory of pseudomorphic monoclinic and rhombohedral heterostructures”. In: *Journal of Applied Physics* 124.18 (2018), p. 185302. ISSN: 0021-8979, 1089-7550. DOI: [10.1063/1.5045845](https://doi.org/10.1063/1.5045845).
- [76] H.L. Alberts and J.C.A. Boeyens. “The elastic constants and distance dependence of the magnetic interactions of Cr₂O₃”. In: *Journal of Magnetism and Magnetic Materials* 2.4 (1976), pp. 327–333. ISSN: 03048853. DOI: [10.1016/0304-8853\(76\)90044-5](https://doi.org/10.1016/0304-8853(76)90044-5).

- [77] Marius Grundmann. “A most general and facile recipe for the calculation of heteroepitaxial strain”. In: *physica status solidi (b)* 257.12 (2020), p. 2000323. ISSN: 0370-1972, 1521-3951. DOI: [10.1002/pssb.202000323](https://doi.org/10.1002/pssb.202000323).
- [78] Max Kneiß *et al.* “Strain states and relaxation for α -(Al_xGa_{1-x})₂O₃ thin films on prismatic planes of α -Al₂O₃ in the full composition range: Fundamental difference of a- and m-epitaxial planes in the manifestation of shear strain and lattice tilt”. In: *Journal of Materials Research* 36.23 (2021), pp. 4816–4831. ISSN: 0884-2914, 2044-5326. DOI: [10.1557/s43578-021-00375-3](https://doi.org/10.1557/s43578-021-00375-3).
- [79] Marius Grundmann. *The Physics of Semiconductors: An Introduction Including Nanophysics and Applications*. Graduate Texts in Physics. Cham: Springer International Publishing, 2016. ISBN: 978-3-319-23879-1 978-3-319-23880-7. URL: <http://link.springer.com/10.1007/978-3-319-23880-7>.
- [80] Derek Hull and D. J. Bacon. *Introduction to Dislocations*. 5th ed. Elsevier Ltd., 2011. 268 pp. ISBN: 978-0-08-096673-1.
- [81] M. Grundmann and M. Lorenz. “Anisotropic strain relaxation through prismatic and basal slip in α -(Al, Ga)₂O₃ on R-plane Al₂O₃”. In: *APL Materials* 8.2 (2020), p. 021108. ISSN: 2166-532X. DOI: [10.1063/1.5144744](https://doi.org/10.1063/1.5144744).
- [82] M. Grundmann, T. Stralka, and M. Lorenz. “Epitaxial growth and strain relaxation of corundum-phase (Al,Ga)₂O₃ thin films from pulsed laser deposition at 1000 °C on r-plane Al₂O₃”. In: *Applied Physics Letters* 117.24 (2020), p. 242102. ISSN: 0003-6951, 1077-3118. DOI: [10.1063/5.0030675](https://doi.org/10.1063/5.0030675).
- [83] Michael Lorenz. “Pulsed laser deposition”. In: *Encyclopedia of Applied Physics*. Wiley, 2019. URL: <http://dx.doi.org/10.1002/3527600434.eap810>.
- [84] Holger von Wenckstern *et al.* “A review of the segmented-target approach to combinatorial material synthesis by pulsed-laser deposition”. In: *Phy. Status Solidi B* 257.7 (2020), p. 1900626. ISSN: 0370-1972, 1521-3951. DOI: [10.1002/pssb.201900626](https://doi.org/10.1002/pssb.201900626).
- [85] V. Srikant, J. S. Speck, and D. R. Clarke. “Mosaic structure in epitaxial thin films having large lattice mismatch”. In: *Journal of Applied Physics* 82.9 (1997), pp. 4286–4295. ISSN: 0021-8979, 1089-7550. DOI: [10.1063/1.366235](https://doi.org/10.1063/1.366235).
- [86] L. J. van der Pauw. “A method of measuring specific resistivity and Hall effect of discs of arbitrary shape”. In: *Philips Research Reports* 13.1 (1958), pp. 1–9.
- [87] Hiroyuki Fujiwara. *Spectroscopic Ellipsometry. Principles and Applications*. Tōkyō: John Wiley & Sons, Ltd, 2007. ISBN: 978-4-621-07253-0.
- [88] J.C. Manifacier *et al.* “Optical and electrical properties of SnO₂ thin films in relation to their stoichiometric deviation and their crystalline structure”. In: *Thin Solid Films* 41.2 (1977), pp. 127–135. ISSN: 00406090. DOI: [10.1016/0040-6090\(77\)90395-9](https://doi.org/10.1016/0040-6090(77)90395-9).

- [89] A. R. Zanatta. “Revisiting the optical bandgap of semiconductors and the proposal of a unified methodology to its determination”. In: *Scientific Reports* 9.1 (2019), p. 11225. ISSN: 2045-2322. DOI: [10.1038/s41598-019-47670-y](https://doi.org/10.1038/s41598-019-47670-y).
- [90] Jan Tauc. “Optical properties of amorphous semiconductors and solar cells”. In: *Fundamentals of Semiconductors*. 3rd ed. Berlin, Heidelberg: Springer, 2005. ISBN: 3-540-41323-5.
- [91] Alex Dolgonos, Thomas O. Mason, and Kenneth R. Poeppelmeier. “Direct optical band gap measurement in polycrystalline semiconductors: A critical look at the Tauc method”. In: *Journal of Solid State Chemistry* 240 (2016), pp. 43–48. ISSN: 00224596. DOI: [10.1016/j.jssc.2016.05.010](https://doi.org/10.1016/j.jssc.2016.05.010).
- [92] Mohamed A. Hafez, Mohamed K. Zayed, and Hani E. Elsayed-Ali. “Review: Geometric interpretation of reflection and transmission RHEED patterns”. In: *Micron* 159 (2022), p. 103286. ISSN: 09684328. DOI: [10.1016/j.micron.2022.103286](https://doi.org/10.1016/j.micron.2022.103286).
- [93] Dieter K. Schroder. *Semiconductor Material and Device Characterization*. 1st ed. Wiley, 2005. ISBN: 978-0-471-73906-7 978-0-471-74909-7. URL: <https://onlinelibrary.wiley.com/doi/book/10.1002/0471749095>.
- [94] Pavlo Makushko *et al.* “Flexomagnetism and vertically graded Néel temperature of antiferromagnetic Cr₂O₃ thin films”. In: *Nature Communications* 13.1 (2022), p. 6745. ISSN: 2041-1723. DOI: [10.1038/s41467-022-34233-5](https://doi.org/10.1038/s41467-022-34233-5).
- [95] Anubhav Jain *et al.* “Commentary: The Materials Project: A materials genome approach to accelerating materials innovation”. In: *APL Materials* 1.1 (2013), p. 011002. ISSN: 2166-532X. DOI: [10.1063/1.4812323](https://doi.org/10.1063/1.4812323).
- [96] M W Cho *et al.* “ZnO epitaxial layers grown on c-sapphire substrate with MgO buffer by plasma-assisted molecular beam epitaxy (P-MBE)”. In: *Semiconductor Science and Technology* 20.4 (2005), S13–S21. ISSN: 0268-1242, 1361-6641. DOI: [10.1088/0268-1242/20/4/002](https://doi.org/10.1088/0268-1242/20/4/002).
- [97] O. Durand *et al.* “Interpretation of the two-components observed in high resolution X-ray diffraction ω scan peaks for mosaic ZnO thin films grown on c-sapphire substrates using pulsed laser deposition”. In: *Thin Solid Films* 519.19 (2011), pp. 6369–6373. ISSN: 00406090. DOI: [10.1016/j.tsf.2011.04.036](https://doi.org/10.1016/j.tsf.2011.04.036).
- [98] S.I. Anisimov, B.S. Luk'yanchuk, and A. Luches. “An analytical model for three-dimensional laser plume expansion into vacuum in hydrodynamic regime”. In: *Applied Surface Science* 96–98 (1996), pp. 24–32. ISSN: 01694332. DOI: [10.1016/0169-4332\(95\)00373-8](https://doi.org/10.1016/0169-4332(95)00373-8).
- [99] Anna Hassa. “Epitaxy and Physical Properties of Group-III Sesquioxide Alloys”. PhD thesis. Leipzig University, 2021.

- [100] Daisuke Shinohara and Shizuo Fujita. "Heteroepitaxy of Corundum-Structured α -Ga₂O₃ Thin Films on α -Al₂O₃ Substrates by Ultrasonic Mist Chemical Vapor Deposition". In: *Japanese Journal of Applied Physics* 47 (9R 2008), p. 7311. ISSN: 0021-4922, 1347-4065. DOI: [10.1143/JJAP.47.7311](https://doi.org/10.1143/JJAP.47.7311).
- [101] Takayoshi Oshima, Takeya Okuno, and Shizuo Fujita. "Ga₂O₃ Thin Film Growth on c-Plane Sapphire Substrates by Molecular Beam Epitaxy for Deep-Ultraviolet Photodetectors". In: *Japanese Journal of Applied Physics* 46 (11R 2007), p. 7217. ISSN: 0021-4922, 1347-4065. DOI: [10.1143/JJAP.46.7217](https://doi.org/10.1143/JJAP.46.7217).
- [102] Kazuaki Akaiwa, Yoshito Ito, and Shizuo Fujita. *Growth and Characterization of α -Ga₂O₃ Films on Sapphire Substrates with α -(Al,Ga)₂O₃ Buffer Layer*. 2013. DOI: [10.11470/jsapmeeting.2013.2.0_466](https://doi.org/10.11470/jsapmeeting.2013.2.0_466). Pre-published.